MASTER THESIS IN PHYSICS/ACOUSTICS

Normally incident ultrasonic beam transmission through a water-embedded steel plate as a function of ka-number

Irene Dahl Isaksen

June 2023

Department of Physics and Technology
University of Bergen

Abstract

For non-destructive testing (NDT) used for immersed pipes and plane walls to e.g. characterize properties of or detect flaws in structures, the understanding of the underlying physics and characteristics is important for developing and further improving measurement solutions.

Complex characteristics have been revealed in the transmitted near-field of a water-embedded steel plate insonified by a bounded incidence beam. The guided ultrasonic waves appear as leaky Lamb waves, leading to some interesting effects, such as near-field beam enhancement, resonance shift, and beam narrowing and widening. This thesis aims to provide further insight into this by focusing on the Lamb modes S_2, A_2 and A_3. In-house built transducers and simulations utilizing the angular spectrum method are used for investigating normally incident ultrasonic beam transmission through a water-embedded steel plate of 6.05 mm as a function of ka-number.

Simulations were conducted for ka-numbers in the range of 1 to 120. Some spectral characteristics were present for all ka-numbers, which was attributed to the plate's response to the finite angular spectrum of the beam. Several additional characteristics were only present in certain ka-ranges, which were suggested to be caused by constructive or destructive interference in the water.

A big difference between measurements and the corresponding simulations was damped and widened behavior of a maximum-minimum doublet associated with A_2 exhibited by the measurements in contrast to narrow and highly dynamic doublet exhibited by the simulations. Considering that the model used in the simulations is not accounting for intrinsic losses in the plate and the water, this may be of significance for this deviation.

Compared to a prior study which studied for the transmission as a function of distance instead, several events were identified as possible events that could correspond to similar events found in this thesis. Other than this, this author was not able to find any prior literature on two events. A maximum occurring for ka-numbers 52 and 60 as part of a maximum-minimum-maximum-minimum quadruple in the frequency band associated with A_2, and a notch occurring for ka = 100 above the maximum associated with A_3.

It was investigated whether ka = 100 would tend toward plane-wave theory. This was inconclusive and suggested further investigations be conducted at an increased distance from the plate.

Acknowledgment

This thesis was conducted in the Acoustic group at the Department of Physics and Technology at the University of Bergen.

First and foremost, I would like to thank my supervisor Prof. Per Lunde and co-supervisors Dr. Mathias Myrtveit Sæther and Prof. Emer. Magne Vestrheim for their guidance. They have helped me understand and navigate the many theoretical and experimental challenges entailed by this thesis by providing fruitful discussions and invaluable insight throughout my master. I would also like to express my gratitude to the numerous people that has been a part of the Acoustic group throughout my thesis, and the helping hand they have offered whenever I needed help.

At last I would like to give a special thanks to friends and family for all the precious support and encouragement given.

Irene Dahl Isaksen

Bergen, 2023

Contents

Chapter 1

Introduction

1.1 Background, motivation and literature

Guided ultrasonic waves (GUW) have been a field of interest for the Acoustic group at the Department of Physics and Technology (IFT) at the University of Bergen (UiB) for the last decade. For a water-embedded steel plate insonified by a sound beam, GUW appears as leaky Lamb waves in the plate for the frequencies and plate dimensions considered in the current work. Some interesting beam effects have been observed in the transmitted pressure field through the plate, such as near-field beam enhancement, resonance shift, beam narrowing and beam widening [2, 3], attributed as diffraction effects caused by the transducers bounded beam. This is relevant in NDT applications where understanding such beam effects is crucial, e.g. when determining characteristics or detecting flaws in structures.

In the late 1800's, Rayleigh [4] and Lamb [5, 6] formulated the theory for symmetric and anti-symmetric Lamb modes in a vacuum-embedded solid plate. Reissner [7] then proposed a solution for plane waves transmitted through a fluid-immersed solid plate in 1938, according to [8]. Diffraction effects for the source has been observed in measurements [9], and the failure of plane-wave theory to present a narrow ultrasonic beam was pointed out by [10] according to [8]. Anderson et al. [11] developed in 1995 an angular spectrum (AS) method utilizing a 3D baffled piston model and exact plane-wave pressure transmission coefficient to calculate the transmission through a solid plate embedded in air. It demonstrated the need for 3D modeling, as 2D models do not capture the behavior of the beam well enough. To minimize the bounded beam effects, Cawley and Hosten [12] found that the effects were strongest at lower frequencies and used large transducers in order to utilize plane-wave assumptions.

Holland and Chimenti [13] focused on the unusually efficient transmission of airborne sound waves through plates at the first-order symmetric (S_1) Lamb mode, later referred to as the second-order negative symmetric (S_{-2}) Lamb mode [1], at a range of incident angles. Lohne et al. has from 2008 to 2013 [2, 3, 14–16] studied the transmission of a pulsed piston generated 3D beams through a water-immersed plate using the exact plane-wave pressure transmission coefficient while comparing with measurements. They explained the frequency shift of S_{-2} at normal incidence as beam diffraction effects. In 2013, Aanes [8] partially based his work on [2, 3] and studied piezoelectric transducer excited ultrasonic pulsed beams with a fluid-embedded viscoelastic plate using finite element modeling (FEM), angular spectrum modeling (ASM) and a combination of these, and compared to measurements. A piezoelectric source transducer of ka-number 26 was constructed and characterized for measurements and simulations to gain better control over the transducers as commercial ones provide limited information regarding the transducer's construction, dimensions, materials and material data. These have later been used in several studies [17–19]

Aanes et al. [18] extended earlier work in 2015 by studying a transmitted beam through a water-embedded steel plate at normal beam incidence covering the leaky Lamb modes S_2, A_2 and A_3 in the plate by varying the Poisson's ratio in the range 0.01-0.49 in simulations, also using FEM, ASM and a combination of these. The study found complex characteristics of the transmitted pressure field caused by diffraction due to the finite angular spectrum of the incident beam and identified near-field interference phenomena described in prior literature.The Acoustic Group at IFT, UiB, has since continued researching this [1, 17, 19–21], especially focusing on beam diffraction effects with measurements and simulations. A customization of the angular spectrum model developed by Anderson et al. [11], was suggested by Sæther [22] in 2022. The customization vastly reduced computational time without introducing possible severe aliasing effects [22].

[18] demonstrated a strong correlation between the acoustic phenomena relevant to this thesis and the apparently different guided-wave dispersion phenomena. Furthermore, the research suggests a relation between the size of the mode's NGV region being excited and the beam diffraction phenomena. This was investigated by [19] in the frequency band associated with the S_1 Lamb mode for ka-numbers 14, 20 and 41 by simulations, where the bigger the ka-number, the closer the results were to plane-wave theory. To further investigate this, transducers with ka numbers of 17 and 46, with a thickness mode thickness extension mode 1 (TE1) and center frequency at 500 kHz, lower and higher than those earlier constructed at the acoustic group at IFT UiB [8], was designed, constructed and characterized by Prøytz [23] for future use in the GUW study.

1.2 Objectives

This work is part of ongoing long-term activities at the Acoustic group at IFT UiB on GUW, specifically leaky Lamb waves. The aim is to use fluid-coupled beam excitation of selected leaky Lamb modes to examine some transmission phenomena. Such nearby effects include beam-enhancement, narrowing and widening, splitting, and notches.

For this purpose, three in-house built 500 kHz transducers, one of each ka-numbers 17, 25 and 46, will be utilized in measurements and compared to simulations using FEM and ASM.

The transducers characteristics, such as electrical admittance, sensitivity and beam pattern, will be measured and compared to simulations using FEM . Additionally, the acoustic measurement setup will be revised in an attempt to reduce noise and fluctuations before conducting transmission measurements. These will be compared to simulations using ASM.

The transmission measurements are conducted for normal beam incident at a constant distance from the source to the plate and to the receiving point on the other side of the plate. The frequency range investigate is 350-1000 kHz, relevant for the Lamb modes S_2, A_2 and A_3.

1.3 Outline of the thesis

The thesis consists of 6 chapters in addition to references and appendices. This chapter (Chap. 1) presents the background and motivation for the aim of this thesis while mentioning relevant literature. In addition, the objectives of the thesis are explained in more detail. Chap. 2 presents the theory of this thesis. This includes the theory of transducer characteristics and the FEM that is used to simulate this. Additionally, beam transmission theory will be derived, including leaky Lamb waves, before the angular spectrum method is derived, which is used to simulate beam transmission. The experimental setups and measurement methods are described in Chap. 3. First, the two experimental setups are described with their associated settings. Then the source transducers are presented and the different measurements before the challenges encountered and investigations of this chapter are presented. Further, Chap. 4 presents the simulation setup in the two programs utilized in this thesis, FEMP and ASM2. Then, Chap. 5 presents the results and discussion, starting with the measurements and simulations of the transducers available before a more extensive simulation study for more ka-numbers is presented. These results is further compared to results and simulations from [1] before the finding is discussed. Chap. 6 presents a conclusion and recommends further work. Lastly, the references are provided, along with the appendices comprising the programming scripts used in FEMP and ASM2, as well as supplementary figures.

Chapter 2

Theory

This chapter provides the theoretical basis for understanding the experiments and simulations carried out in this thesis. First, the coordinate system is stated in Chap. 2.1. Then Chap. 2.2 presents a simplified formula for sound velocity in water which later will be compared to sound velocity decided experimentally in the acoustic measurements setup. This is a parameter relevant on several occasions throughout the thesis. Then Chap. 2.3 presents parameters describing transducer properties, the demarcation between near-field and far-field, electrical admittance, source sensitivity and beam pattern. These parameters will be simulated by a transducer model using FEM utilized in the software FEMP which is presented in Chap. 2.4. Chap. 2.5 is presenting plane-wave theory for transmission through a steel plate, first for a vacuum-embedded plate and then for a fluid-embedded plate, where the behavior of Lamb waves is described for both cases. Lastly, the angular spectrum method is presented in Chap. 2.6 where the transducers are represented by a piston source, i.e. an idealized transducer. This method is utilized in the software ASM2 which is used to simulate beam transmission through a water-embedded steel plate.

2.1 Coordinate system

Fig. 2.1 shows the coordinate system of the sources expressed in several coordinates of a point relative to the source. The Cartesian coordinates expresses it like (x,y,z), which is displayed in black, where the x- and y-axis is in the plane of the front of the source and the z-axis is normal to the front of the source. The point expressed in cylindrical coordinates is (r,θ,z), where $r = \sqrt{x^2+y^2}$ and ϕ is the angle in the x,y-plane from the x-axis, and this is displayed in grey with dotted lines for r and z. Further expressed in spherical coordinates, the point is at (r',θ,ϕ), where θ is the angle relative to the z-axis and this is displayed in grey as well.

The term on-axis refers to a position on the z-axis, and the acoustic axis refers to the axis of the maximal sound pressure level of a source.

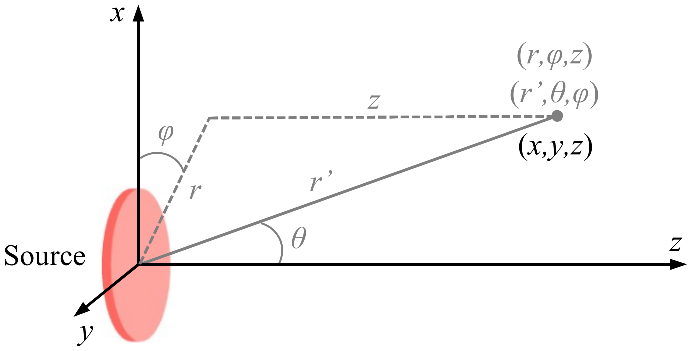

Figure 2.1: Coordinate system

2.2 Sound velocity in water

A simplified formula for sound of speed in distilled water is [24]

$$\begin{aligned} c(P,T) = 1402.7 + 488 \cdot \frac{T}{100} - 482 \cdot \left(\frac{T}{100}\right)^2 - 135 \cdot \left(\frac{T}{100}\right)^3 \\ + \left[15.9 + 2.8 \cdot \frac{T}{100} + 2.4 \cdot \left(\frac{T}{100}\right)^2\right] \cdot \frac{P}{100}, \end{aligned} \tag{2.1}$$

where P is the gauge pressure in bar and T is the water temperature in degrees Celsius.

2.3 Transducer properties

2.3.1 Near-field and far-field

The Rayleigh distance is a convenient demarcation along the z-axis between the complicated near-field found close to a source and the simpler far-field found at large distances from the source [24]. A plane circular piston mounted on a flat rigid baffle of infinite extent, from hereon noted piston source, is used to represent an idealized source. This has the Rayleigh distance [24]

$$\mathrm{Ra} = \frac{\pi a^2}{\lambda}, \tag{2.2}$$

where a is the radius of the piston source, $\lambda = c/f$ is the wavelength of the transmitted sound from the piston, whereas c is the speed of sound in the medium the piston radiates into at frequency f. For a piston source, the axial pressure amplitude is highly variable in the near-field and reaches a decreasing dependency of 1/Ra [24] when equal to or greater than the Rayleigh distance, i.e. in the far-field.

For more complex structures, such as transducers, the effective radius is utilized in order to find the respective Rayleigh distance. This is found by measuring the beam width of the sound field. While there are multiple definitions for the beam width, in this thesis, the beam width where the amplitude on the main lobe of the beam pattern has decreased by 3dB is chosen. This is equal to 2 times the half power angle, $\theta_{3\text{dB}}$ [24]. To determine this, an estimate of the Rayleigh distance is computed using properties of the structure, e.g. the radius of the transducer's front layer as a, to ensure far-field conditions before conducting the measurement of the beam pattern and finding the half power angle. The effective radius is then calculated by [25]

$$\theta_{3\text{dB}} = \sin^{-1}\left(\frac{1.6163}{\text{ka}_{\text{eff}}}\right) \quad \rightarrow \quad a_{\text{eff}} = \frac{1.6163}{k \cdot \sin(\theta_{3\text{dB}})}, \tag{2.3}$$

where $k = \omega/\lambda$ is the wavenumber and $\omega = 2\pi f$ is the angular frequency. The Rayleigh distance is then found by replacing a with a_{eff} in Eq. (2.2).

2.3.2 Electrical admittance

The electrical admittance is a measure of the electrical conductivity and is defined as [26]

$$Y(f) = G(f) + iB(f) = |Y(f)|e^{i\phi_Y(f)}, \tag{2.4}$$

where $G(f)$ is the conductance, $B(f)$ is the susceptance and $\phi_Y(f)$ is the phase.

2.3.3 Source sensitivity

The source sensitivity based on input voltage is defined as [26]

$$S_V(f) = \frac{P(r=0, \phi=0, z=d_0=1m, f)}{V(f)} \tag{2.5}$$

in cylindrical coordinates, where $P(r=0, \phi=0, z=d_0=1m, f)$ is the free-field on-axis sound pressure at a distance of 1 m, assuming far-field conditions at this distance. Measurements of the pressure executed at other distances, $z = d$, is extrapolated to the distance d_0 by the factor d/d_0. $V(f)$ is the transducer's input voltage.

2.3.4 Beam pattern

The directivity is defined as [25]

$$D(f) = \frac{P(r'=d, \theta, \phi=0, f)}{P(r'=d, \theta=0, \phi=0, f)} \tag{2.6}$$

in spherical coordinates, where $P(r'=d, \theta, \phi=0, f)$ is the axial sound pressure amplitude assuming far-field conditions, with an angle θ from on-axis at a given frequency and $P(r'=d, \theta=0, \phi=0, f)$ is the on-axis sound pressure amplitude at distance $r'=d$. The beam pattern is found by calculating the directivity for an angle range $(-\theta, \theta)$ which gives a representation of the pressure variation of the source as a function of the direction at a given distance.

2.4 Finite Element Method

FEM is a discretization of continuous problems.The software used in this thesis is Finite Element Modeling of Piezoelectric structures (FEMP) version 6.1 developed by the Acoustic Group at IFT UIB in cooperation with Christian Michelsen Research which is implemented in the programming language MATLAB. Full theory and description of the original FEMP can be found in Jan Kocbachs dissertation [27] and an overview only concerning relevant parts are reviewed here. FEMP is used to simulate the admittance, source sensitivity and beam pattern for the transducers immersed in water by implementing each transducer's construction as the source subsequently.

The fluid is assumed inviscid and irrotational, while the source is assumed axisymmetric and without torsion modes and can therefore be modeled in 2D with cylinder coordinates [27]. This also reduces the number of material constants needed in the computations reducing computational time. The source is modeled using finite elements and the fluid is divided into two regions, an inner region of finite elements and an outer region of infinite elements applying the Sommerfeld radiation condition, i.e. no reflection returning and interfering with the radiating sound field from the source. The boundary dividing the fluid regions is at the radius of R_{inf} from the center of the transducer, where a minimum distance of [27]

$$R_{\mathrm{inf}} = 0.25 \cdot \frac{(D_{\mathrm{f}}/2)^2}{\lambda_f} \tag{2.7}$$

is recommended for 12th order infinite elements, which is used in this thesis. D_{f} is the diameter of the front layer of the transducer and λ_f is the wavelength of the sound in the fluid. The elements are 8 nodes isoparametric elements where unknown quantities are calculated for the nodes. Points inside the elements are described as a function of the nodes and interpolation functions. The accuracy depends on the number of elements, number of nodes and type of interpolation function where a trade-off between accuracy and computational time needs to be considered for bigger problems/simulations. Elements per wavelength is defined by the shortest wavelength, i.e. shear wavelength for solids, and longitudinal wavelength for fluids [27].

The finite elements (FE) equations using a time-harmonic solution, $e^{i\omega t}$, for a piezoelectric disc in an infinite fluid governing FEMP are [27]

$$-\omega^2 \begin{bmatrix} M_{uu} & 0 & 0 \\ 0 & 0 & 0 \\ 0 & 0 & -M_{\psi\psi} \end{bmatrix} \begin{Bmatrix} \hat{u} \\ \hat{\phi} \\ \hat{\psi} \end{Bmatrix} + i\omega \begin{bmatrix} 0 & 0 & C_{u\psi} \\ 0 & 0 & 0 \\ C_{\psi u} & 0 & 0 \end{bmatrix} \begin{Bmatrix} \hat{u} \\ \hat{\phi} \\ \hat{\psi} \end{Bmatrix} + \begin{bmatrix} K_{uu} & K_{u\phi} & 0 \\ K_{\phi u} & K_{\phi\phi} & 0 \\ 0 & 0 & -K_{\psi\psi} \end{bmatrix} \begin{Bmatrix} \hat{u} \\ \hat{\phi} \\ \hat{\psi} \end{Bmatrix} = \begin{Bmatrix} 0 \\ -Q \\ 0 \end{Bmatrix}, \tag{2.8}$$

where $\{\hat{u}\}$ is the global displacement vector, $\{\hat{\phi}\}$ is the global electrical potential vector, $\{\hat{\psi}\}$ is the global fluid velocity potential vector and $\{Q\}$ is the global charge vector. ω is the angular frequency, $[M_{uu}]$ is the global mass matrix $[M_{\psi\psi}]$ is the global fluid mass matrix, $[C_{u\psi}]$ is the global fluid/structure coupling matrix and $[C_{\psi u}]$ is the transposed matrix of $[C_{u\psi}]$. $[K_{uu}]$ is the global stiffness matrix, $[K_{u\phi}]$ is the global piezoelectric stiffness matrix, $[K_{\phi u}]$ is the transposed matrix of $[K_{u\phi}]$, $[K_{\phi\phi}]$ is the global dielectric stiffness matrix and $[K_{\psi\psi}]$ is the global fluid stiffness matrix.

A simpler calculation of the response functions can be found by deriving the FE equations from K- to H-form. Introducing the potential difference between the two electrodes of the piezoelectric disc, V, where one is set as as ground and reference, and the current going to the other electrode, $I = i\omega t$ [27], gives [27]

$$-\omega^2 \begin{bmatrix} M_{uu} & 0 & 0 \\ 0 & 0 & 0 \\ 0 & 0 & -M_{\psi\psi} \end{bmatrix} \begin{Bmatrix} \hat{u} \\ V \\ \hat{\psi} \end{Bmatrix} + i\omega \begin{bmatrix} 0 & 0 & C_{u\psi} \\ 0 & 0 & 0 \\ C_{\psi u} & 0 & 0 \end{bmatrix} \begin{Bmatrix} \hat{u} \\ V \\ \hat{\psi} \end{Bmatrix} + \begin{bmatrix} H_{uu} & H_{u\phi} & 0 \\ H_{\phi u} & H_{\phi\phi} & 0 \\ 0 & 0 & -K_{\psi\psi} \end{bmatrix} \begin{Bmatrix} \hat{u} \\ V \\ \hat{\psi} \end{Bmatrix} = \begin{Bmatrix} 0 \\ -I/(i\omega) \\ 0 \end{Bmatrix}, \tag{2.9}$$

where the $[H]$ matrices are defined by different $[K]$ matrices, given in Eqs. (3.190)-(3.192) in [27].

For fluid, only direct harmonic analysis is applicable which is calculated directly from manipulation of the matrix equations.. First, the third equations in Eq. (2.9) is solved for the global fluid velocity potential giving [27]

$$\{\hat{\psi}\} = i\omega \left(\omega^2[M_{\psi\psi}] - [K_{\psi\psi}]\right)^{-1} [C_{\psi u}]\{\hat{u}\}, \tag{2.10}$$

and then this is combined with the third equation in Eq. (2.9) and solved for the global displacement vector giving [27]

$$\{\hat{u}\} = -[D]^{-1}\{H_{u\phi}\}V, \tag{2.11}$$

where the response function is [27]

$$[D] = [H_{uu}] - \omega^2[M_{uu}] + \omega^2[C_{u\psi}]\left(-[K_{\psi\psi}] + \omega^2[M_{\psi\psi}]\right)^{-1}[C_{\psi u}]. \tag{2.12}$$

By inserting the global velocity potential, Eq. (2.10), in to the relation between the velocity potential and the acoustic pressure in the fluid for the time harmonic case [27]

$$p = -i\omega\rho_f\psi, \tag{2.13}$$

the global acoustic pressure is found [27]

$$\{\hat{p}\} = -\omega^2\rho_f\left(-[K_{\psi\psi}] + \omega^2[M_{\{}\psi\psi])\right)^{-1}[C_{\psi u}]\{\hat{u}\}. \tag{2.14}$$

The admittance is found by further combining Eq. (2.12) and the second equation in Eq. (2.9) giving [27]

$$Y = i\omega\left(\{H_{u\phi}\}^T[D]^{-1}\{H_{u\phi}\} - H_{\phi\phi}\right). \tag{2.15}$$

2.5 Beam transmission

A propagating wave field can be decomposed into a summation of plane waves in different directions. Therefore, plane wave theory for Lamb waves in a vacuum-embedded plate is derived before an overview regarding leaky Lamb waves is presented. A thorough derivation of the latter can be found in [8].

2.5.1 Lamb waves

The plate is assumed elastic, homogeneous, isotropic. It has thickness $2L$ in z-direction, vertically, and has infinite extent in x- and y-direction, horizontally. Studying plane waves interaction with this plate embedded in vacuum, the linearized displacement equation of motion is [28]

$$(\lambda_{\mathrm{La},s} + 2\mu_{\mathrm{La},s})\nabla(\nabla\cdot\underline{u}) - \mu_{\mathrm{La},s}[\nabla\times(\nabla\times\underline{u})] = \rho_s\frac{\partial^2\underline{u}}{\partial t^2}, \tag{2.16}$$

where $\lambda_{\mathrm{La},s}$ and $\mu_{\mathrm{La},s}$ are the Lamé parameters for the plate assumed constant, $\underline{u}$ is the displacement, ρ_s is the density of the plate and t is time. Utilizing Helmholtz decomposition, this can be expressed by scalar potential, Φ, and vector potential, $\underline{\Psi}$, one for longitudinal and one for shear waves, in two separate equations [28]. Without loss of generality, the motion is defined as propagating in x- and z-direction, so that the components are independent of y, i.e. there is no change in y-direction. The description of the y-components becomes superfluous and can be removed alongside horizontally polarized shear (SH) waves, which leaves the longitudinal (P) and vertically polarized shear (SV) waves [28]. The equations for horizontal and vertical displacements and normal and shear stresses are then [28]

$$u_x = \frac{\partial \Phi}{\partial x} - \frac{\partial \Psi_y}{\partial z}, \qquad u_z = \frac{\partial \Phi}{\partial z} + \frac{\partial \Psi_y}{\partial x}, \tag{2.17}$$

$$T_{zz} = (\lambda_{\mathrm{La},s} + 2\mu_{\mathrm{La},s})\frac{\partial u_z}{\partial z} + \lambda_{\mathrm{La},s}\frac{\partial u_x}{\partial x}, \qquad T_{xz} = \mu_{\mathrm{La},s}\left(\frac{\partial u_x}{\partial z} + \frac{\partial u_z}{\partial x}\right), \tag{2.18}$$

respectively. The solution for the scalar and vector potential is then found by separation of variables [28]

$$\Phi = \left(A_s^- e^{ih_z z} + A_s^+ e^{-ih_z z}\right) e^{i(\omega t - \eta x)}, \qquad \Psi_y = \left(B_s^- e^{ih_z z} + B_s^+ e^{-ih_z z}\right) e^{i(\omega t - \eta x)}, \tag{2.19}$$

where A_s^- and A_s^+ are the amplitudes of the P waves inside the plate propagating in $-z$- and $+z$-direction, respectively, and B_s^- and B_s^+ are the amplitudes of the SV waves inside the plate propagating also propagating in $-z$- and $+z$-direction, respectively. $h = \omega/c_l$ and $k = \omega/c_t$ is the longitudinal and shear wavenumbers where c_l and c_t is the longitudinal and shear wave velocity, respectively. Both waves have the same phase velocity on the surfaces, derived from the boundary conditions, and together with the aforementioned defined wave propagating in x-direction, the horizontal wavenumber is $\eta = h_x = k_x$, where h_x is the horizontal longitudinal wavenumber and h_x is the horizontal shear wavenumber [28]. The vertical wavenumbers are then defined as [28]

$$h_z = \begin{cases} \sqrt{h^2 - \eta^2} & \text{for } \eta \leq h \\ i\sqrt{\eta^2 - h^2} & \text{for } \eta > h \end{cases}, \qquad k_z = \begin{cases} \sqrt{k^2 - \eta^2} & \text{for } \eta \leq k \\ i\sqrt{\eta^2 - k^2} & \text{for } \eta > k \end{cases}, \tag{2.20}$$

where evanescent waves are included.

For every wave interaction with a boundary, two new waves are excited in the plate, one compression wave and one shear wave, which results in an infinite number of waves propagating in the plate called a Lamb wave. For a vacuum-embedded plate there is no stress at the boundaries, i.e. the boundaries move freely, keeping the energy inside the plate. Fig. 2.2 shows an illustration of this of one plane wave where *(a)* shows the boundary interactions of the (P) and shear (SV) waves causing new waves, which ultimately results in a Lamb wave. *(b)* illustrates the P and SV waves represented by their respective coefficients.

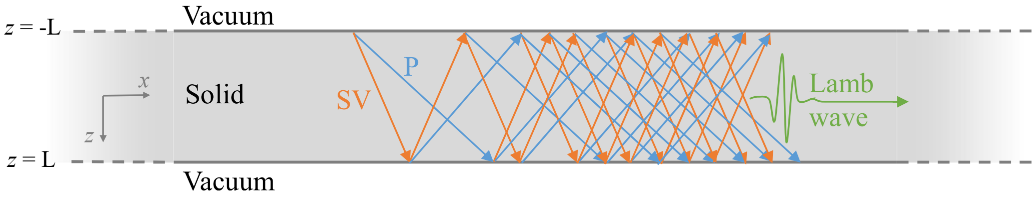

(a)

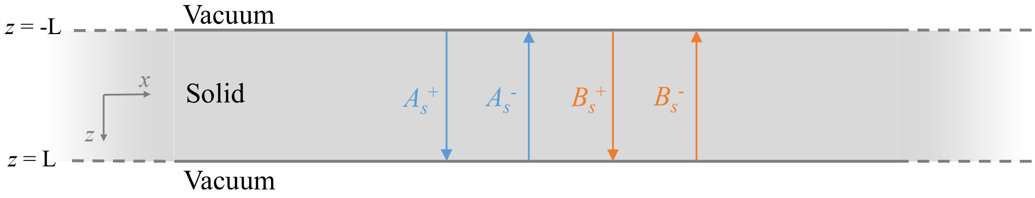

(b)

Figure 2.2: Longitudinal and shear waves propagating in a vacuum-embedded steel plate for one plane wave. (a) Longitudinal (P), and vertically polarized shear (SV) waves propagating resulting in a Lamb wave. (b) Longitudinal (A) and vertically polarized shear (B) waves represented by collective coefficients propagating in + and - z-direction.

Further on, using trigonometric functions and utilizing the boundary conditions, zero stress at the boundaries, in Eq. (2.18), while suppressing the term $e^{i(\omega t-\eta x)}$ [8], the symmetric and anti-symmetric Lamb modes are derived [28]

$$\begin{aligned}\text{Symmetric:}\quad & \frac{-4\eta^2 h_z k_z}{(2\eta^2-k^2)^2}=\frac{\tan(k_zL)}{\tan(h_zL)},\\ \text{Anti-symmetric:}\quad & \frac{-4\eta^2 h_z k_z}{(2\eta^2-k^2)^2}=\frac{\tan(h_zL)}{\tan(k_zL)}.\end{aligned}\tag{2.21}$$

Both the symmetric and anti-symmetric modes are a function of P and SV waves. In the symmetric mode, the plate compresses and expands, while for the anti-symmetric mode, the top and bottom of the plate move like a flexural wave. Illustrations of these movements are shown in Fig. 2.3 where *(a)* shows the symmetrical mode and *(b)* shows the anti-symmetrical mode.


(a) *(b)*

Figure 2.3: Modes in a vaccum-embedded steel plate. (a) Symmetric mode. (b) Anti-symmetric mode.

Asymptotic solutions of Eq. (2.21) provides cutoff frequencies for the Lamb modes which are useful reference frequencies for later use. At these frequencies, standing compressional and shear waves are present across the thickness of the plate. These are found by first letting the phase velocity of the generated Lamb wave in x-direction, $c_{\text{ph}}=\omega/\eta$, approach infinity for η approaching zero, giving [28]

$$\begin{aligned}\text{Symmetric:}\quad & \frac{\tan(k_zL)}{\tan(h_zL)}=0,\\ \text{Anti-symmetric:}\quad & \frac{\tan(h_zL)}{\tan(k_zL)}=0.\end{aligned}\tag{2.22}$$

The solutions are found for when the numerator becomes zero or the denominator becomes to infinity [28]:

$$\lim_{x \to n\pi} \tan(x) = 0 \quad \text{or} \quad \lim_{x \to \frac{n\pi}{2}} \tan(x) = 0, \tag{2.23}$$

where $x = hL$ or $x = kL$, and $n = 1, 2, 3...$ Cutoff frequencies are then [28]

$$\begin{aligned} &\text{Symmetric:} \qquad f_{ln}^{S} = \frac{(2n-1)c_l}{4L},\ n = 1,2,3... \ \text{and,}\ f_{tn}^{S} = \frac{2nc_t}{4L},\ n = 1,2,3...,\\ &\text{Anti-symmetric:}\ f_{ln}^{A} = \frac{2nc_l}{4L},\ n = 1,2,3... \ \text{and,}\ f_{tn}^{A} = \frac{(2n-1)c_t}{4L},\ n = 1,2,3... \end{aligned} \tag{2.24}$$

where f_{ln}^{S} and f_{tn}^{S} are the corresponding frequencies for the symmetrical thickness-shear (TS) and thickness-extensional (TE) modes, and f_{ln}^{A} and f_{tn}^{A} are the corresponding frequencies for the anti-symmetric TS and TE modes.

As mentioned, this thesis is focused on normal beam incidence through a steel plate of thickness $2L = 6.05$ mm with a compressional velocity of 5780 m/s and shear velocity of 3130 m/s [2], corresponding to a Poisson's ratio of 0.2925 [1]. The cutoff frequencies within the frequency range of interest, 350 kHz to 1 MHz, are $f_{l1}^{S} = 477.686$ kHz, $f_{t2}^{S} = 517.355$ kHz ,$f_{t3}^{A} = 776.033$ kHz ,$f_{l2}^{A} = 955.372$ kHz which corresponds to the Lamb modes S_{-2}, S_2, A_2, A_3. Following the terminology of [8] and [1], f_{l1}^{S} and f_{t2}^{S} are the lower and upper cutoff frequencies of the S_2 mode, excluding the S_{-2} mode for simplicity, and f_{t3}^{A} and f_{l2}^{A} are the cutoff frequencies for the A_2 and A_3 modes, respectively. Related to the TE and TS resonances of the plate, f_{l1}^{S} and f_{l2}^{A} are the resonance frequencies of TE1 and TE2, and f_{t2}^{S} and f_{t3}^{A} are the resonance frequencies of TS2 and TS3.

2.5.2 Leaky Lamb waves

When the plate is immersed in an infinite fluid, the guided waves inside the plate generate P waves in the fluid while propagating, leaking energy into the fluid, hence the name leaky Lamb wave. The motion is still also defined as propagating in x- and z-direction here. A P wave propagating from the upper fluid layer, $f1$, in the direction of the plate, generates a reflected wave back into the fluid and a transmitted wave into the plate. The transmitted wave is then further transmitting a wave into the second fluid layer on the lower side of the plate, $f2$. For a plane wave of normal incident to the plate, only P waves are generated inside the plate, which is not causing any guided waves in the plate and no energy is leaked into the fluid. For a plane wave of oblique angle to the plate, a guided wave consisting of P and SV waves is generated, causing energy to leak into both fluid layers giving leaky wave fields of P waves. Fig. 2.4 shows an illustration of this where *(a)* illustrates the boundary interaction from a plane wave at an oblique angle to the plane generating a leaky Lamb wave of P and SV waves in the plate and leaky wave field in both fluids. *(b)* illustrates P and SV represented by their respective coefficients where A_{f1}^{+} and A_{f1}^{+} is the coefficient of the incident, reflection and leaky waves propagating in $+z$- and $-z$-direction in the upper fluid $f1$, and A_{f2}^{+} is the coefficient of the transmitted waves propagating in $+z$- in the lower fluid $f2$.

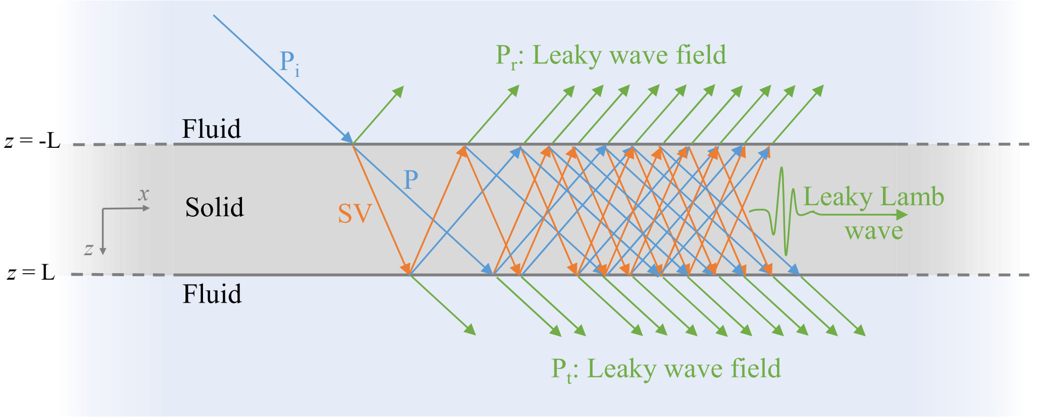

(a)

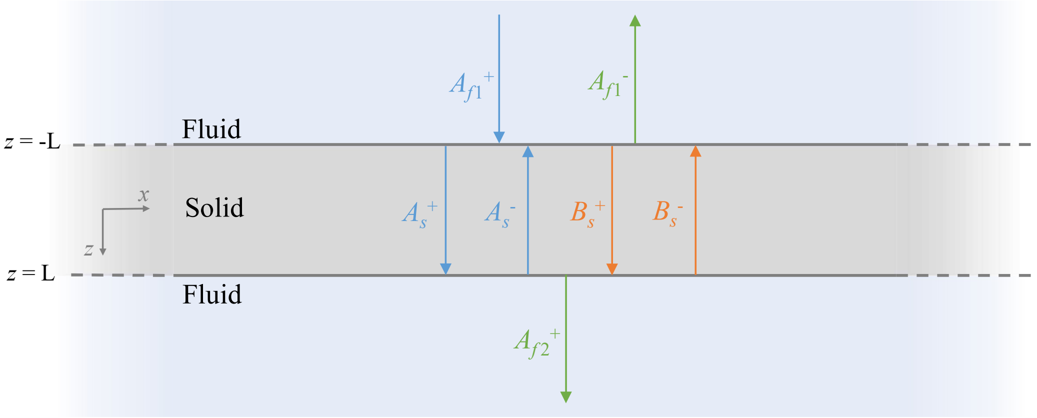

(b)

Figure 2.4: Longitudinal and shear waves propagating in a vacuum-embedded steel plate. (a) Longitudinal (P), and vertically polarized shear (SV) waves propagating resulting in a leaky Lamb wave. (b) Longitudinal (A) and vertically polarized shear (B) waves represented by collective coefficients propagating in + and - z-direction.

The sound pressure in the fluid layers can be written as [8]

$$\begin{aligned} \Phi_{f1} &= A_{f1}^{+} e^{-ih_{f,z}z} + A_{f1}^{-} e^{ih_{f,z}z}, \\ \Phi_{f2} &= A_{f2}^{+} e^{-ih_{f,z}z}, \end{aligned} \tag{2.25}$$

where the vertical wavenumber for the fluid is [8]

$$h_{f,z} = \begin{cases} \sqrt{h_f^2 - \eta^2} \text{ for } \eta \leq h_f \\ i\sqrt{\eta^2 - h_f^2} \text{ for } \eta > h_f, \end{cases} \tag{2.26}$$

where $h_f = \omega / c_f$, $c_f = \sqrt{\lambda_{\mathrm{La},f} / \rho_f}$, $\lambda_{\mathrm{La},f}$ are the Lamé parameter for the fluid and ρ_f is the fluid density.

The boundary conditions here are a continuation of normal displacement and normal stress across the boundaries, while the shear stress is zero. The horizontal and normal displacement and normal stress at the boundaries between the plate and the fluid layers are given as [8]

$$u_x = \frac{\partial \Phi}{\partial x}, \quad u_z = \frac{\partial \Phi}{\partial z}, \tag{2.27}$$

$$T_{zz} = -p = \lambda_{\mathrm{La},f} \left(\frac{\partial u_x}{\partial x} + \frac{\partial u_z}{\partial z} \right) \tag{2.28}$$

respectively, where p is the sound pressure. This gives [8]

$$\begin{aligned} u_{f1,z} &= -ih_{f,z} \left[A_{f1}^{+} e^{-ih_{f,z}z} - A_{f1}^{-} e^{ih_{f,z}z} \right], \\ u_{f2,z} &= -ih_{f,z} A_{f2}^{+} e^{-ih_{f,z}z}, \end{aligned} \tag{2.29}$$

$$\begin{aligned} T_{f1,zz} &= -\rho_f \omega^2 \left[A_{f1}^{+} e^{-ih_{f,z}z} - A_{f1}^{-} e^{ih_{f,z}z} \right], \\ T_{f2,zz} &= -\rho_f \omega^2 A_{f2}^{+} e^{-ih_{f,z}z}, \end{aligned} \tag{2.30}$$

where $u_{f1,z}$ and $u_{f2,z}$ is the displacement at the upper and lower boundaries between the plate and the fluid layers, respectively, and $T_{f1,zz}$ and $T_{f1,zz}$ is the normal stress at the boundaries the plate and the fluid layers respectively. Further derivation of the dispersion relations for symmetric and anti-symmetric leaky Lamb waves can be found in [8].

As this theory is presented in relation to the transmission, only the transmission coefficient will be utilized, which is derived by this author in Chap. 2.6. Fig. 2.5 [1] shows the magnitude of the plane-wave transmission coefficient for a water-embedded steel plate, $|T(\theta,d,f)|$, as a function of the plane-wave incidence angle θ, distance to the plate, d, and the frequency, calculated by Eq.(2.36). $\theta = \sin^{-1}(\eta/h_f)$ for $\eta \leq h_f$. The overlayed black dashed curves are the dispersion curves for the associated Lamb modes in the plate (i.e. vibrating in vacuum), calculated for real η. The symmetric and anti-symmetric Lamb modes present in the $f-\theta$ range here is marked $S_0, S_1, S_2, S_{\text{-}2}$ and A_0, A_1, A_2, A_3, respectively [1]. The plane-wave cutoff frequencies of Lamb modes $S_{\text{-}2}$, S_2, A_2, A_3 of a solid plate with Poisson's ratio in the range $1/5-1/3$ are labeled f_{l1}^{S}, f_{t2}^{S}, f_{t3}^{A} and f_{l2}^{A}. f_{l1}^{S} and f_{t2}^{S} are the lower and upper cutoff frequencies of the S_2 mode, and f_{t3}^{A} and f_{l2}^{A} are the cutoff frequencies of the A_2 and A_3 modes.

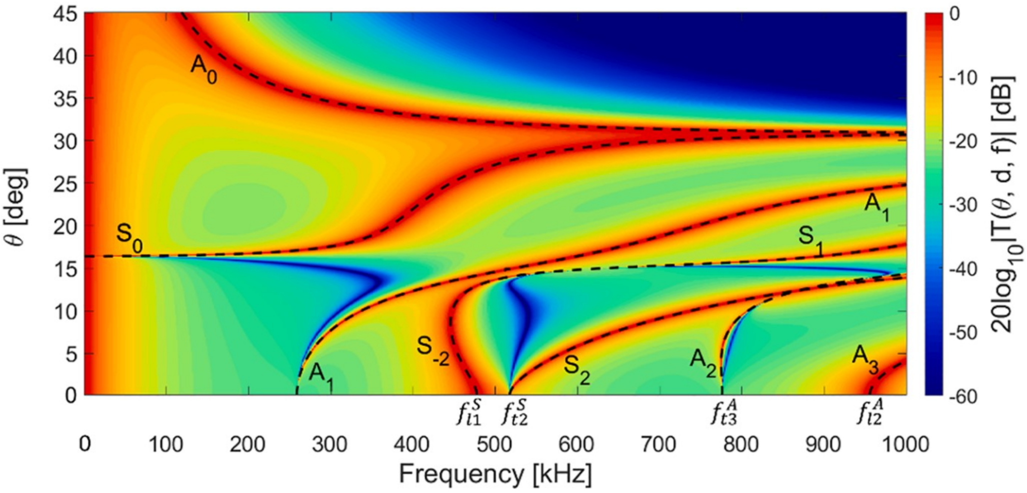

Figure 2.5: Magnitude of the plane-wave pressure transmission coefficient for a 6.05 mm thick water-embedded steel plate. Plotted together with dispersion curves (dotted dashed lines) for the associated Lamb modes of the plate vibrating in vacuum [1]. Figure from [1] with permission from authors.

2.6 Angular spectrum method

The angular spectrum method models a propagating wave field by decomposing it into a summation of an infinite number of plane waves in different directions. Sæther [22] proposed a customization of the angular spectrum model developed by Anderon et al. [11]. The purpose was to examine on-axis beam transmission through a solid plate for a plane circular piston while reducing computational time and preventing possible severe aliasing effects that ASM1 can give [22]. This customized software is the one used in this thesis, referred to as ASM2, for the simulation of beam transmission through a water-embedded steel plate at normal incidence and this is implemented in the programming language MATLAB. An overview regarding relevant theory of the physics and mathematics is shown here, whereas the while the execution of the calculations in the software is described in [22].

The source is represented by a plane, circular and baffled piston. This is immersed in water, which is assumed inviscid and irrotational, at a distance from a steel plate parallel to the piston's front surface. The plate is assumed to be elastic, isotropic, homogeneous, lossless and of infinite lateral extent and thickness d. The source is radiating an acoustic beam field into the water, which is transmitted through the plate. Fig.2.6 shows the setup and includes two points on-axis from the source, one at the upper surface of the steel plate, $z_0 = 270$ mm from the piston source and one on the other side of the plate in the water, $z_1 = 376.05$ mm from the piston source and 100 mm from the steel plate. The thickness of the steel plate is $d = 6.05$ mm. Distances are stated for each important segment.

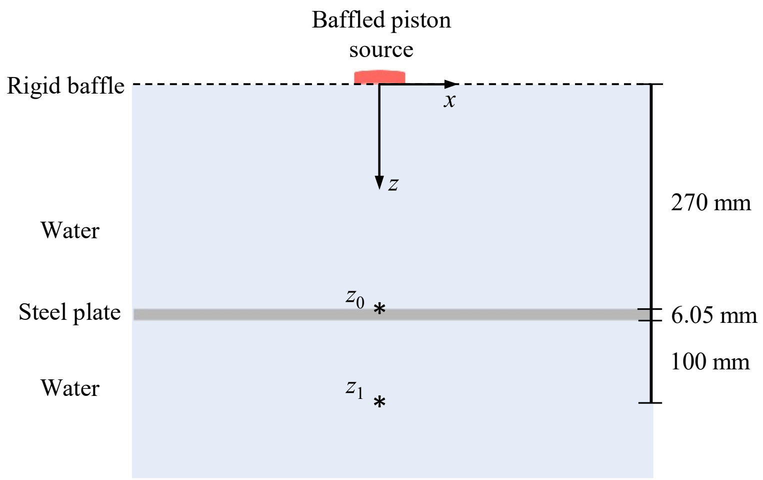

Figure 2.6: Illustration of the setup for simulation of beam transmission with .

The ASM model is expressed in cylindrical coordinates (r,ϕ,z) and since the source is assumed axisymmetric, ϕ is superfluous and omitted [1]. A time convention $e^{i\omega t}$ is used and suppressed [1].

Starting with the z-component of the piston's particle velocity, $v_z(r,z=0,f)$ is assumed constant on the surface of the transducer and zero elsewhere. Using spatial Hankel transformation, the particle velocity wavenumber spectrum is given as [1]

$$V_z(\eta,0,f) = 2\pi\int_0^\infty v_z(r,z=0,f)J_0(\eta r)rdr = \pi a^2 v_0 \frac{2J_1(a\eta)}{a\eta}, \tag{2.31}$$

where J_0 and J_1 are the zeroth and first order Bessel functions of first kind and η is the wave vector component in direction parallel to the plate, r-direction. Since the plate is assumed homogeneous and without internal sources, there are no evanescent and propagating waves rapidly decaying in r-direction. Thus only real-valued η are left to be considered [1].

The z-component of the linearized Euler's equation is the frequency domain is given as [1]

$$i\omega\rho_f v_z(r,z,f) = -\frac{\partial p(r,z,f)}{\partial z}, \tag{2.32}$$

and using spatial Hankel transformation then gives [1]

$$i\omega\rho_f V_z(\eta,z,f) = -\frac{\partial P(\eta,z,f)}{\partial z} = uh_{f,z}P(\eta,z,f), \tag{2.33}$$

for a plane wave propagating in the positive z-direction at a given η and ϕ. Combining Eqs. (2.31) and (2.33) gives the sound pressure wavenumber spectrum at $z=0$ [1]

$$P(\eta,0,f) = \frac{\omega a\rho_f}{\eta h_{f,z}} 2\pi v_0 J_1(a\eta). \tag{2.34}$$

$P(\eta,0,f)$ is then propagating to the distance z_0 in the fluid, which is the distance of the plate from the source, using the plane-wave propagation term $e^{-ih_{f,z}z_0}$, giving [1]

$$P_i(\eta, z_0, f) = P(\eta, 0, f)e^{-ih_{f,z}z_0}, \tag{2.35}$$

where $P_i(\eta, z_0, f)$ is the sound pressure wavenumber spectrum of the incident free-field sound pressure frequency spectrum p_i in the fluid, at the upper surface of the plate, in absence of the plate.

To handle the transmission through the plate, a plane-wave transmission coefficient is introduced [1]

$$T(\eta, d, f) = \frac{P(\eta, z_0 + d, f)}{P_i(\eta, z_0, f)}, \tag{2.36}$$

where $P(\eta, z_0 + d, f)$ is the sound pressure wavenumber spectrum in the fluid at the plate's lower surface.This is calculated by [1]

$$T(\eta, d, f) = \frac{-iY(A+S)}{(S+iY)(A-iY)} \tag{2.37}$$

where

$$\begin{aligned} Y &= \frac{\rho_f h_z}{\rho h_{f,z}} k^4, \\ S &= \left(2\eta^2 - k^2\right)\cot\left(h_z \frac{d}{2}\right) + 4\eta^2 h_z k_z \cot\left(k_z \frac{d}{2}\right), \\ A &= \left(2\eta^2 - k^2\right)\tan\left(h_z \frac{d}{2}\right) + 4\eta^2 h_z k_z \tan\left(k_z \frac{d}{2}\right). \end{aligned} \tag{2.38}$$

The sound pressure wavenumber spectra at distances $z > z_0 + d$ can then be described as [1]

$$P(\eta, z, f) = P_i(\eta, z_0, f)T(\eta, d, f)e^{-ih_{f,z}(z-d-z_0)} = P(\eta, 0, f)T(\eta, d, f)e^{-ih_{f,z}(z-d)}. \tag{2.39}$$

Further on, the inverse Hankel transform is used on P and P_i, obtaining the sound pressure frequency spectra [1]

$$p(r, z, f) = \frac{1}{2\pi}\int_0^\infty P(\eta, z, f)J_0(\eta r)\eta d\eta \tag{2.40}$$

and

$$p_i(r, z_0, f) = \frac{1}{2\pi}\int_0^\infty P_i(\eta, z_0, f)J_0(\eta r)\eta d\eta, \tag{2.41}$$

so that Eq. (2.42) can be used.

The plate's acoustic response at the acoustic axis ($r = 0$) can then be studied using the axial pressure transfer function [1] which for this thesis at $z = z_1$ on the other side of the plate is

$$H_{pp}(0, z_1, f) = \frac{p(0, z_1, f)}{p_i(0, z_0, f)}, \tag{2.42}$$

where $p_i(0, z_0, f)$ is the axial free-field sound pressure frequency spectrum radiated by the piston at the upper surface of the plate, as if the plate was absent. With this the plate's acoustic response at the acoustic axis $(r = 0)$ can be studied. $p(0, z_1, f)$ is the axial sound pressure frequency spectrum transmitted through the steel plate at a distance z_1. These are measured experimentally, where $p_i(0, z_0, f)$ is measured without the plate present, and $p(0, z_1, f)$ with the plate present, and compared with the simulations.

In the customization, there was made a conversion from 2D to 1D model using cylindrical coordinates. Further on, a combination of the use of Gauss quadrature and a generalized Filon method for more accurate pressure calculations compared to the use of fast Fourier transformation was introduced, and lastly, adaptive numerical integration algorithms in MATLAB and error control parameters were introduced, which is highly user-friendly [22].

This software is used in the calculations of beam transmission through the plate, $p(r = 0, z, f)$. As for $p_i(r = 0, z_0, f)$, a minor limitation was discovered in the software for this specific task, where calculations at a few frequencies demanded a high computational time. Therefore, [24]

$$\mathbf{p}(r', \theta = 0, \phi = 0, t) = \rho_0 c U_0 \left[1 - e^{-ik(\sqrt{r^2+a^2}-r)}\right] e^{i(\omega t - kr)}, \tag{2.43}$$

expressed in spherical coordinates, is used for this purpose where the absolute value is extracted for the magnitude.

Chapter 3

Experimental setup and measurement method

This chapter presents the experimental setup and measuring method for this work. First, the experimental setup and the associated instrument settings are presented along with alignment and distance measurements and data processing. Then, the experimental setup for electrical admittance measurements is described. Further on, the source transducers utilized in this thesis are presented and then the measurement methods used in this thesis are described. Lastly, challenges encountered and investigations regarding the acoustic experimental setup and measurement method are presented.

All curves shown and compared to in this thesis originating from others' studies are obtained using the tool CurveSnap [29], which is a software that captures curve data from screenshots taken of the respective thesis'. Deviations from the actual data occur, e.g. apparent fluctuations and higher or lower levels, as its accuracy varies, especially when extracting data from small figures.

3.1 Acoustic measurements

3.1.1 Experimental setup

The acoustic measurements, the sound velocity, transducer sensitivity, transducer directivity and transmission measurements were conducted in a water tank of inner dimensions (width, height, length) = (71, 57.5, 157.5) cm at the acoustic laboratory at IFT UIB, hereon referred to as Tank A. Fig 3.1 shows the setup where *(a)* shows the setup at the laboratory and *(b)* shows an illustration of the setup.

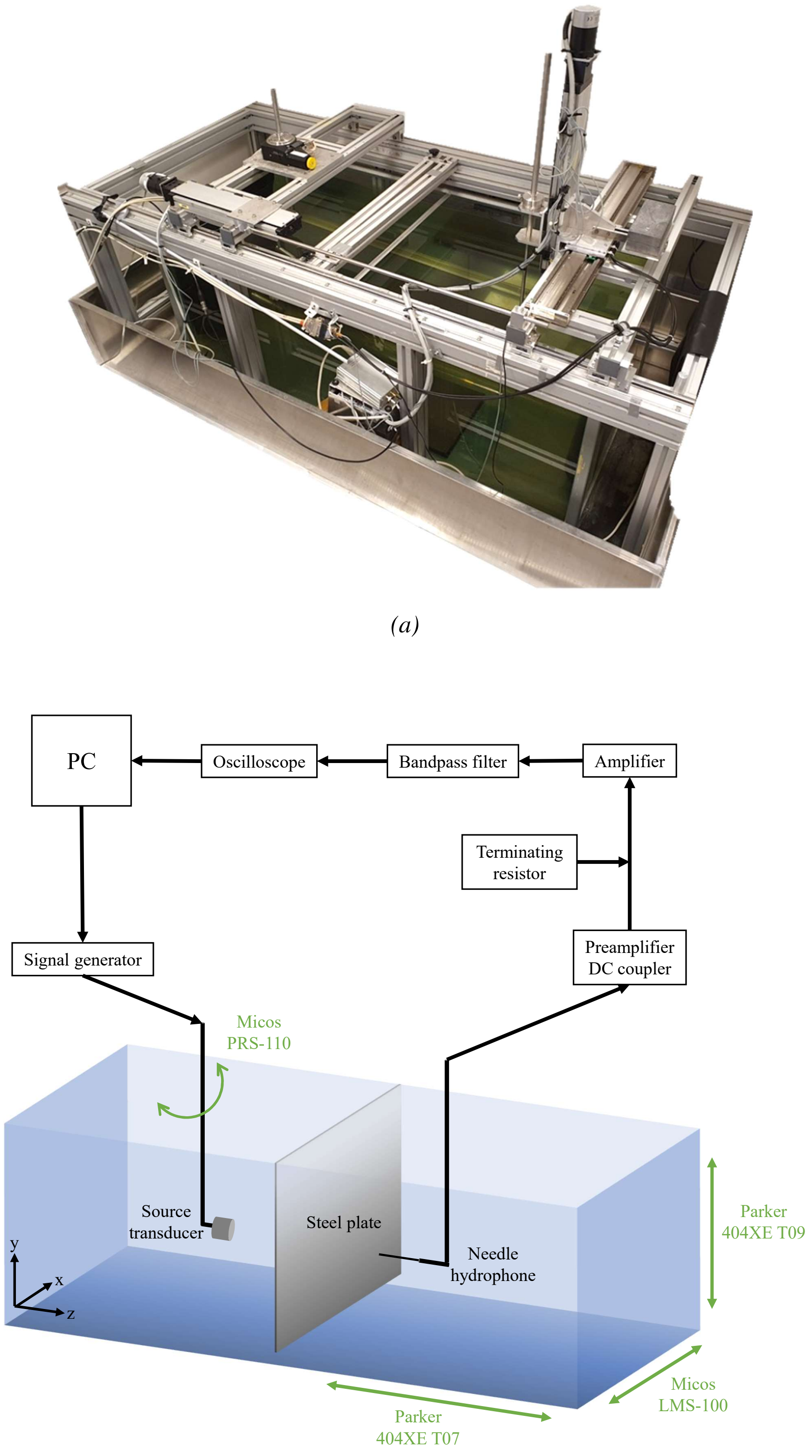

(a)

(b)

Figure 3.1: Acoustic measurement setup in Tank A. (a) Setup at IFT UiB. (b) Illustration of the setup including signal path and motor stages.

Table 3.1 lists the instruments in the signal path with their corresponding serial number (SN), excluding the source transducers, which are described in Chap. 3.3.

Table 3.1: Instruments signal path

Role	Instrument	Serial number
Signal generator	Hewlett Packard 33120A [30]	
Needle hydrophone	1 mm PVDF PA	1820 [31]
Needle hydrophone	1 mm PVDF PA	1848 [32]
Preamplifier	-	PA110078 [31]
DC coupler	-	DCPS223 [31]
Terminating resistor	Resistance load of 50 Ω	-
Amplifier	FEMTO HVA-10M-60-F [33]	05-04-235
Bandpass filter	Krohn-Hite model 3940 [34]	LR2722R (508) 580-1660
Oscilloscope	Tektronix DPO3012 [35]	

A signal generator excites a water-immersed piezoelectric source transducer through a coaxial cable of length 180 cm, which converts the signal to pressure and transmits it into the water. For transmission measurements, a hot rolled AISI 316L stainless steel plate [2] of dimensions (width, height, length) = (500, 760, 6.05) mm is immersed in the x, y-plane between the transducer and the needle hydrophone. Two different 1 mm PVDF Precision Acoustics Ltd. (PA) needle hydrophones featuring a probe length of 100 mm and a measurement uncertainty of 9% in the frequency range $0.1 - 1$ MHz are used to detect the pressure and convert it back into a voltage signal. The signal is further sent through a preamplifier [31] and a DC coupler [31]. It is then transmitted through a RG-58 coaxial cable and terminated by a 50 Ω load in parallel with the amplifier [33] operating in 40 dB mode. A bandpass filter [34] filters the signal at Butterworth mode before it is digitalized by an oscilloscope [35] and sent to the PC for further data processing.

The hydrophone SN 1820 was calibrated together with preamplifier PA110078 and DC coupler DCPS223, which are the ones used in this thesis. This was executed by PA and the National Physical Laboratory (NPL) UK, as well as in-house by Aanes using a 3-transducer reciprocity calibration scheme [8], and covers the frequencies from 100 kHz to 1 MHz. This hydrophone measured the sound velocity in water and the transducer's beam patterns. The hydrophone SN 1848 was calibrated together with another preamplifier SN PA10028 and DC coupler SN 606 in 2011 by PA and NPL UK. The frequency calibration data available covers the frequencies of 1 MHz to 20 MHz, which unfortunately only covers the highest frequency measured in this thesis, 1 MHz. Nevertheless, this limitation will only have an impact on absolute measurements, such as sensitivity, as opposed to the relative measurements this measured; the transducers' sensitivities and transmission measurements. When necessary, the calibration data for hydrophone SN 1820, preamplifier PA110078 and DC coupler DCPS223 from NPL UK is used when hydrophone 1848 SN is deployed.

The system is comprised of two carriages, both able to move in z-direction where Carriage 1 is connected to the source transducer, and Carriage 2 is connected to the needle hydrophone. A Parker 404XE T07 linear stage [36] with a positional accuracy of 90 μm is mounted on

Carriage 1, and a rod of approximately 89 cm can be attached to couple the two carriages together. By tightening one carriage to the frame, keeping it stationary, it allows the Parker stage to move the other carriage in z-direction. Additionally, Carriage 1 is equipped with a Micos precision rotary stage PRS-110 [37] with a maximum resolution of 0.002° which enables the transducer to rotate in the xz-plane while keeping the center of the front at rest. Carriage 2 has a Micos lineary motor stage LMS-100 [38] with a positional accuracy of 0.015 μm for movement in x-direction, and a Parker 404XE T09 linear stage [36] with a precision accuracy of 106 μ for movement in y-direction.

3.1.2 Instrument settings

For all measurements using the main measurement setup, the signal generator is set at a 10 V_{pp} sine burst at a burst rate of 10 Hz and signal duration of 130 μs. While the signal generator's voltage is specified for an output resistance 50 Ω, the transducers impose a much higher load than this, resulting in an increased amplitude in the voltage over the transducer. For the oscilloscope, which has an input resistance of 1 MHz, the V_{pp} was just below 20 at frequency 575 kHz. The oscilloscope is set to an 8-bit vertical resolution and temporal settings are set to 100 000 samples in the 400 μs window with a sample rate of 250 MHz. For each measurement, 512 samples are averaged per point. The bandpass filter is working at Butterworth mode as a moving filter from frequencies $400/575 \cdot f$ to $800/575 \cdot f$, relative to the frequency measured. There are three rubber mats placed strategically in the water tank to minimize and dampen the diffuse sound field arising during measurements; one behind the transducer, one behind the hydrophone and one at the bottom in the middle of the tank. The transducers are attached to a holder, a cylinder, when submerged in the tank, where they are aligned by their respective markings to the holder with a set screw located at the top of the holder pointing in positive y-direction.

3.1.3 Alignment and distance measurements

The transducer and hydrophone are roughly aligned at the acoustic axis, approximately along the z-axis, by eye and then adjusted acoustically by moving the hydrophone while finding the maximum sound pressure at the respective measurement's peak amplitude.

A steel measuring tape with an estimated user uncertainty of 0.5 mm is used for distance measurements. The front of the transducer is aligned with the center of a pole of diameter 11.0 mm, measured by a Vernier caliper [39], which has an uncertainty of 0.05 mm. The needle hydrophone is also attached to a pole, and its distance from the closest point on the pole was measured to be 250 millimeters using a steel measuring tape with a measuring uncertainty of 1 millimeter. The distance between the transducer and the hydrophone is then found by measuring the distance between the two poles, adding $11/2$ mm and subtracting 250 mm. This has an accumulated uncertainty of $u = 0.5 + 0.05 = 0.5$ mm.

For transmission measurements, a reference rod of length 270 mm is used between the transducer and steel plate. Similarly, a reference rod of length 100 mm is used between the steel plate and the hydrophone. The reference rods user uncertainty is assumed to be 0.5 mm. With the Micos rotary stage, the transducer is rotated towards one of the walls in the y, z-plane of the tank. A diode circuit is inserted before the transducer to use the transmitter/receiver mode of the transducer. The transducer is then rotated until the maximum sound pressure level is found. Once the highest level is identified, the transducer is rotated 90° toward the hydrophone, which is then adjusted acoustically in the usual manner when the steel plate is absent. When the steel plate is present, the hydrophone is adjusted after the plate has been submerged and the system is at rest.

3.1.4 Data processing

A Fourier spectrum technique is used to process the data in the measurement window (MW) of the measured waveform. For each measurement, a MW in the steady-state region (SSR) is defined for all data points in the measurement. This is found by examining raw data waveforms extracted at different frequencies or angles depending on the type of measurements, such as resonance frequency, local maximum magnitude, local dips etc. Any zero offset is removed and the first and last zero-crossing points within the MW are obtained, defining an integer of periods. The signal is then zero-padded to increase frequency resolution after Fourier transforms it. The magnitude of the peak in the Fourier spectrum corresponds to the peak-to-peak of the MW in the waveform.

In Tank A, the boundaries of the water tank give reflections that can affect the measurements by interfering before the direct signals duration is completed. The maximal water height is 52 cm, smaller than the width of the tank, making the water surface and the bottom the crucial surfaces. As the water continuously evaporates, adding a safety margin is necessary to prevent frequent refilling and thus limit air bubbles in the tank. The signal duration is 130 μs. For a chosen water height of 50 cm and a distance of 376.05 mm as for the transmission measurements, considering the largest transducer CP2, the first reflections arrive earliest 410.9 μs after the direct signal, therefore, not affecting measurements. For sensitivity measurements, where the distance is 0.87 m, the reflections occur 85.6 μs after the direct signal, while for directivity measurements, where the distance is 0.63 m, the reflections occur 109.5 μs after. Therefore, for both sensitivity and directivity measurements, reflections interfere with the signal before it reaches completion, which limits the possible area for choosing the MW. Hence, data must be taken before this occurs, as failure to do so will falsely impact the results.

3.2 Experimental setup for electrical admittance measurements

The electrical admittance measurements are conducted in air and water using another water tank of inner dimensions (width, height, length) = (102, 104.5, 401) cm, also located at the acoustic laboratory at IFT UiB, which will be referred to as Tank B.

Fig. 3.2 shows the electrical admittance measurement setup where *(a)* shows the air measurement setup, including the Impedance analyzer where the transducers are placed on top of styrofoam to radiate freely. *(b)* shows half of the water measurement setup, excluding the Impedance analyzer shown in *(a)*. Here, the transducer is submerged in water while attached to a pole with duct tape and aimed at an oblique angle to minimize direct reflections. During testing, the transducers were attached to the carriage mounted on the steel railing, similar to the setup shown in Fig 3.1. However, these measurements were highly influenced by shorting issues due to the casing being electrically connected to the steel railing, and therefore, duct tape was chosen to eliminate this electrical connection. Unfortunately, this can affect the vibrations of the transducers.

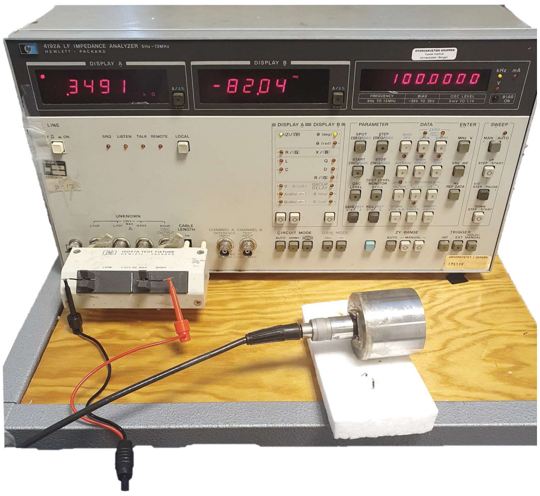

(a)

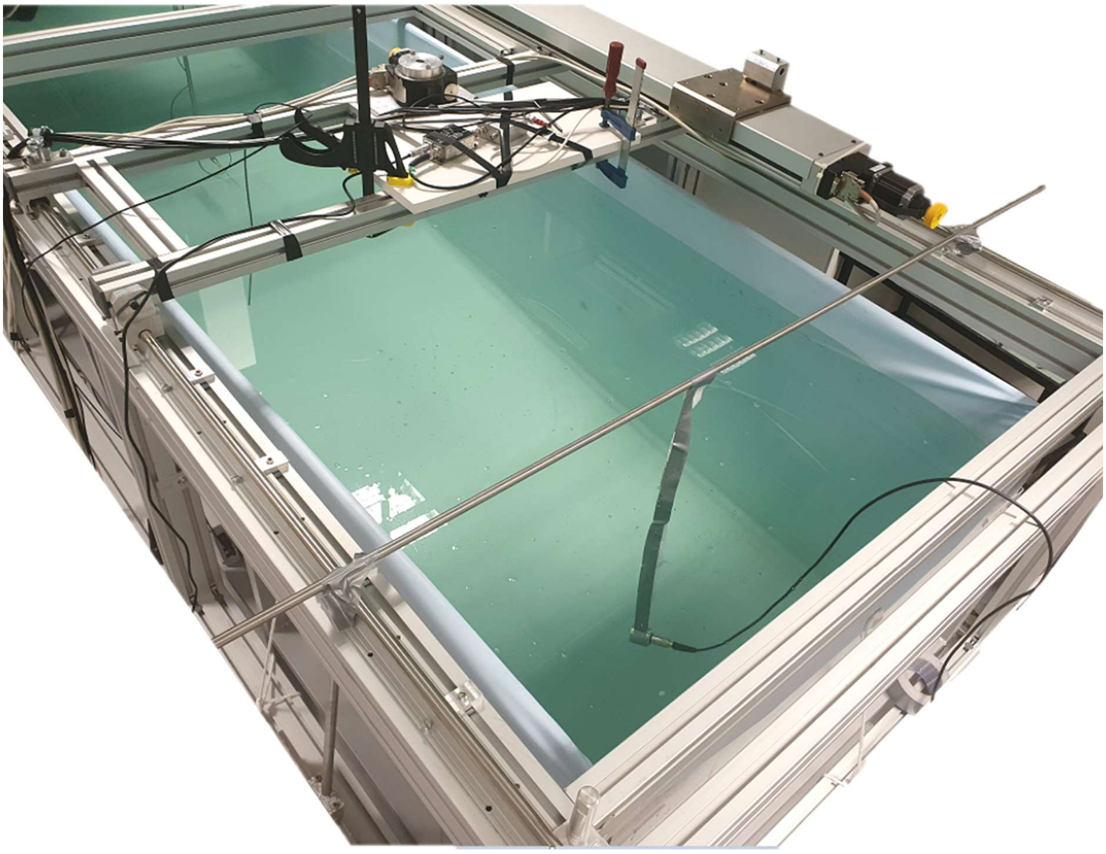

(b)

Figure 3.2: Admittance measurement setup. (a) Air measurement setup. (b) Water measurement setup showing half of Tank B and excluding the Impedance analyzer shown in (a).

For both measurements, the transducer is connected to a RG-58 coaxial cable of length 180 cm connected to another coaxial cable of length 110 cm, which splits into two hook clips. These are clipped onto short wires connected to a HP4192A LF Impedance analyzer [40], shown in Fig. 3.2a.

3.3 Source transducers

The source transducers used in this thesis are piezoelectric ultrasonic transducers of ka-numbers 17, 26 and 46, where k denotes the wavenumber at which the center frequency of $f_{TE1} = 500$ kHz is used, and a denotes the radius of the piezoelectric discs. These transducers are optimized for maximal source sensitivity at 575 kHz, designed for use in water-immersed measurements, with the aim to use in GUW studies at a frequency range of 350 kHz to 1000 kHz. The transducer with ka= 26 is prototype 3 made by Aanes [8], hereon noted as MA. The transducers with ka=17 and 46 are transducers 4 and 3, respectively, made by Prøytz [23], and will hereon be noted as CP1 and CP2, respectively, according to ascending size.

Fig. 3.3 presents the transducers at three angles, one of the side, one of the side including the front and one of the side including the back. To ensure reproducibility during measurements, the transducers are fastened to a holder using a set screw and rotated to a specific angle indicated by a marking. On the left-most picture showing the side of the transducers, clear markings are shown. For MA in Fig. 3.3a, the number three is engraved (upside down in picture), for CP1 in Fig. 3.3b, there is a stamp on the casing, and for CP2 in Fig. 3.3c, there is a straight line engraved following the length of the transducer. (In case of the stamp disappears on CP1, there is engraved ”SD-23S” on the side of the casing square, almost coinciding with the marking.) A thin, long strip of duct tape is centered on these markings and is used to align the transducers straight up in $+y$-direction.

(a)

(b)

(c)

Figure 3.3: Pictures of the transducers showing their respective marking, front and back of the transducers. (a) MA. (b) CP1. (c) CP2.

The transducers’ consists of a piezoelectric disc, a front layer, a conductive adhesive layer coupling them, a backing layer, an air pocket and a casing enclosing it. Illustrations of half the cross-section along the z-axis of the transducers is shown in Fig. 3.4. Fig. 3.4a illustrates MA and 3.4b illustrates CP1 and CP2.

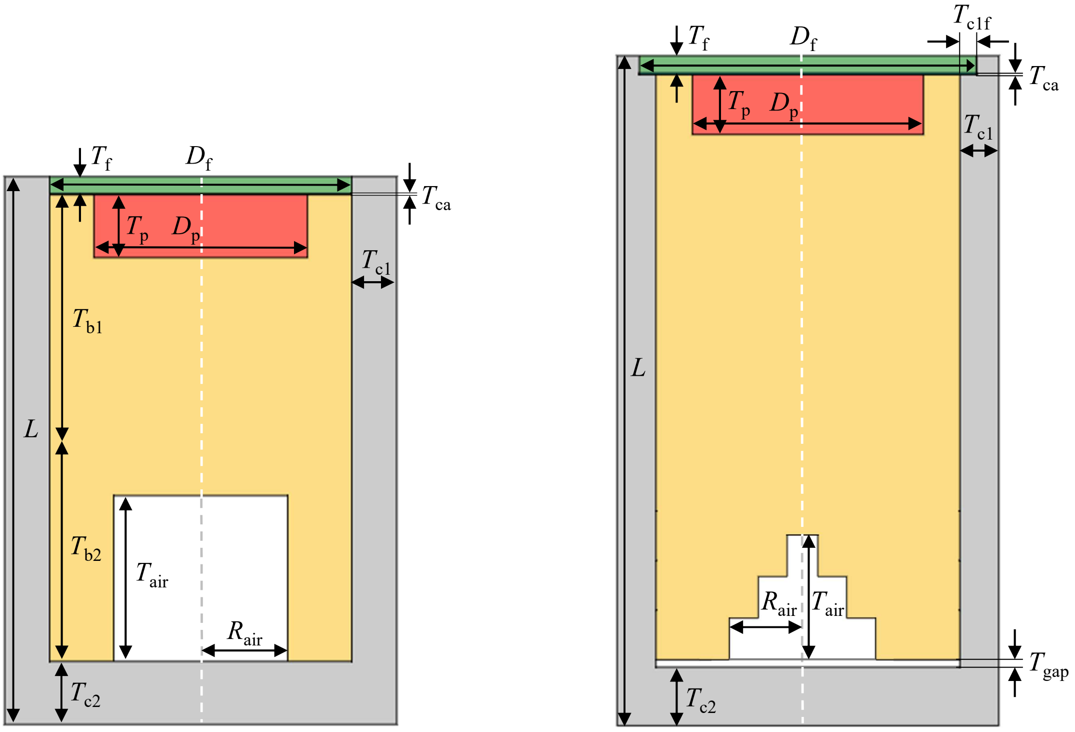

(a) *(b)*

Figure 3.4: Illustrations of the cross-section from back to front of the transducers. (a) MA. (b) CP1 and CP2.

Transducer dimensions are listed in Table 3.2 where *(a)* lists the dimensions for MA and *(b)* lists the dimensions for CP1 and CP2. The values are primarily sourced from [8] and [23], with a few exceptions. For MA, R_{air} has been modified, and for CP1 and CP2, T_{c1}, T_{c2} and R_{air} has been modified while T_{gap} is added. Further elaboration on the reasons behind this selection and the specific alterations made are provided in Sec. 4.1.2.

Table 3.2: Transducer dimensions. (a) MA. (b) CP1 and CP2.

(a)

	MA
D_p [mm]	24.877
T_p [mm]	3.956
D_f [mm]	30.440
T_f [mm]	1.065
T_ca [mm]	0.07125
T_b1 [mm]	15.12
T_b2 [mm]	13.64
T_c1 [mm]	2.83
T_c2 [mm]	3.96
L [mm]	34.42
R_air [mm]	11.2
T_air [mm]	10.42

(b)

	CP1	CP2
D_p [mm]	16.171	44.03
T_p [mm]	3.973	4.017
D_f [mm]	23.031	51.16
T_f [mm]	1.123	1.172
T_ca [mm]	0.036	0.106
T_c1 [mm]	2.046	2.608
T_c1f [mm]	0.974	1.109
T_c2 [mm]	2.997	3.930
L [mm]	45.01	45.06
R_air [mm]	7.50	5.00
T_air [mm]	10.00	10.00
T_gap [mm]	0.5	0.5

For all transducers, D_p and T_p are the diameter and thickness of the piezoelectric discs, respectively, and D_f and T_f are the diameter and thickness of the front layer, respectively. The conductive adhesive has a thickness of T_ca and covers the lower surface of the front layer. L is the length of the total transducer. The backing layer, casing and air pocket differ among the transducers. For MA, the backing layer consists of two solid pieces of the same material and has the thicknesses T_b1 and T_b2. These are both fitted, the upper one to fit the piezoelectric disc in, and the lower one with an air cone [8]. The air pocket is in reality a cone but is described and simulated as a rectangle of radius R_air and thickness T_air. The casing consists of a cylinder surrounding the transducer of thickness T_c1, and a disc of thickness T_c2 enclosing the transducer at the bottom. For CP1 and CP2, the casing consists of a cylinder surrounding the transducer of thickness T_c1 which has a hatch of thickness T_c1f at the top, covered by the front layer. CP1 is enclosed at the bottom by a casing square which is described as a disc, and CP2 is enclosed by a casing disc. These are of thickness T_c2. The backing layer was a liquid mixture that solidified inside the transducer during construction while shaping an air cone in the bottom of the transducer [23]. The air pocket is in reality a cone in these as well but is here described and simulated by steps by diving the radius R_air and thickness T_air into three equal parts. In the bottom of the transducer between the backing layer and air cone, and the back piece of casing, there is an air gap of thickness T_gap.

The materials used in the transducers are specified in Table 3.3. MA uses the lead zirconate titanate material, pz27 [41], as the piezoelectric disc material. Eccosorb MF114 [42] is used as the front layer material, and a silver conductive epoxy 2-component electrically conductive adhesive [43] is used as the conductive adhesive. The backing layer is made of divinycell HCP70 [44], and the casing is made of AISI 316L stainless steel [2], the same as the steel plate. CP1 and CP2 have the same type of piezoelectric disc but with data from [45] and Eccosorb MF114 [46] for the front layer. The conductive adhesive used is 8330D [47], and the backing layer is a tungsten epoxy mixture of SDS-Epofix-Hardener [48] and tungsten powder and grains. The casing is also made of steel [23]. The specific material data can be found in [8] and [23], and is also given in App. A.4.

Table 3.3: Transducer materials

	MA	CP
Piezoelectric disc	Lead zirconate titanate piezoceramic material, Pz27 [41]	Lead zirconate titanate piezoceramic material, Pz27 [45]
Front layer	Eccosorb MF114 [42]	Eccosorb MF114 [42]
Conductive adhesive	Silver Conductive Epoxy [43]	8330D [47]
Backing layer	Divinycell HCP70 [44]	Tungsten epoxy mixture of SDS-Epofix-Hardener [48] and tungsten powder and grains
Casing	AISI 316L Stainless steel [2]	Steel [23]

3.4 Measurements

The distances chosen for the sensitivity and beam pattern measurements are chosen for possible comparison to measurements and simulations by [8] and [23] and for transmission measurements, the distance is chosen for possible comparison to [17], [1] and [19] in addition to [2] and [3].

3.4.1 Sound velocity - water

The equation for sound velocity in water provided by [24] applies to distilled water. However, in the case of water tank A used in the acoustic measurements, the water was taken from a tap and there was a constant growth of algae in the tank. These conditions are less than ideal and could impact the validity of the equation under these circumstances. Therefore, a preliminary measurement was conducted to determine if the equation still holds true.

The experimental estimation of the sound velocity was carried out using the acoustic measurement setup as described in Chap. 3.1.1, without the presence of the steel plate. Four consecutive measurements using the transducer MA with the stated settings specified in Chap. 3.1.2 at frequency 575 kHz were executed at relative distances of $[0, 0.05, 0.1, 0.15]$ m along the acoustic axis, approximately along the z-axis. The step distance was controlled by the Parker 404XE T07 motor stage, which has an accuracy of $u = \pm(0.025 + 0.01 \cdot \text{distance})$ mm [36] and the temperature was measured to be 21.5°C.

As signals lack a clear starting point in reality, it is necessary to define a stable reference point for them that is transferable across distances. This can be achieved by selecting the third positive peak of the signal, which exhibits a considerable amplitude and a noticeable increase compared to the preceding peak. By defining the reference amplitude between these peaks, the trigger point can be stabilized, thereby minimizing the impact of variations in amplitude. The raw data obtained from the measurements were extracted and any zero offset was corrected before the MW was selected. The reference amplitude was then defined as 54% of the MW's mean positive peak value, V_p, corresponding to an amplitude between the third and second peaks. By drawing a line, $V_{\text{trigger}} = 54\% \cdot V_p$, the reference point can be determined at the first intersection of the raw data with this line, and the time can be extracted from this point. An example of this is shown in Fig. 3.5.

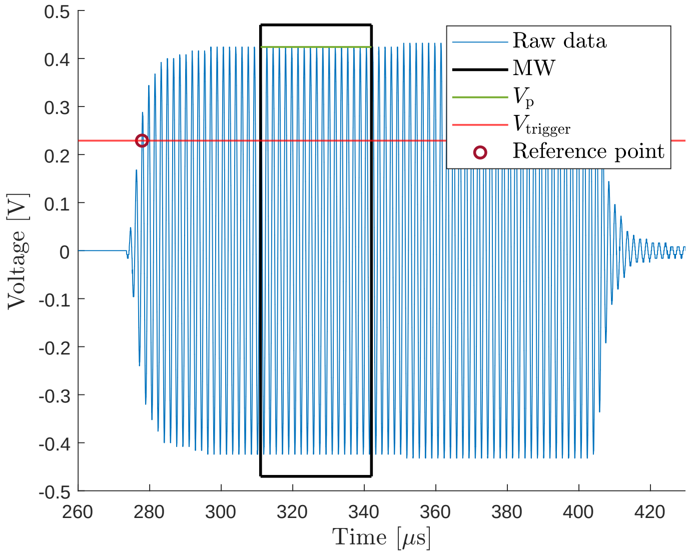

Figure 3.5: Example of a raw data waveform indicating the measurement window (MW), voltage peak value, voltage trigger value and reference point.

Then the time value of the reference point was obtained for each measurement at a respective distance and averaged, and the respective uncertainty is calculated by type A experimental standard deviation, [49], σ. MATLAB's ”fitlim” function was used to perform a linear regression of distance versus time, resulting in the sound velocity. The uncertainty was determined using the min-max method based on the two-pair points, including their respective standard deviations for time and uncertainty for distance, which yielded the steepest and the most gentle slope. The resulting sound velocity was then 1485 ± 2 m/s. This is shown in Fig. 3.6.

In comparison to Eq. (2.1) giving $c(0.02, 21.5) = 1484$ m/s, the experimental estimation covers it. The sound velocity of 1485 m/s obtained from the experimental measurement, is used throughout this thesis.

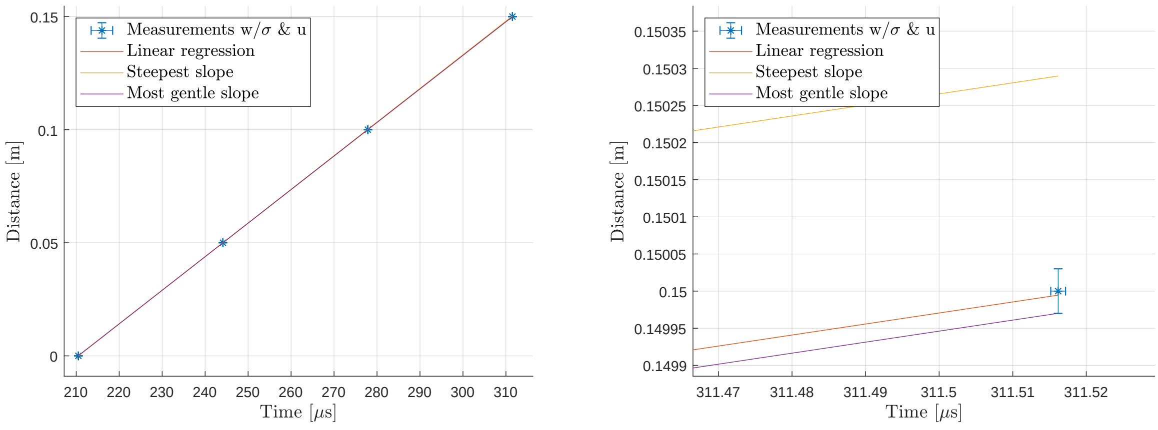

(a) *(b)*

Figure 3.6: Measurements of time versus distance including uncertainties where the slope obtained by linear regression is the sound velocity, including uncertainty. (a) All four measurements (b) Zoom-in version of (a) showing the fourth point as an example.

3.4.2 Electrical admittance

The measurement setup used for the electrical admittance measurements is described in Chap. 3.2. Before each measurement, the instrument and cables used for admittance measurements are calibrated by using the zero adjustment function of the Impedance analyzer. First, it is zero open adjusted by leaving the circuit open, and then it is zero short adjusted by shorting the shield and copper wire together with a short wire closing the circuit [40]. This is shown in Fig. 3.7 where *(a)* is the zero open adjusting and *(b)* is the zero short adjusting.

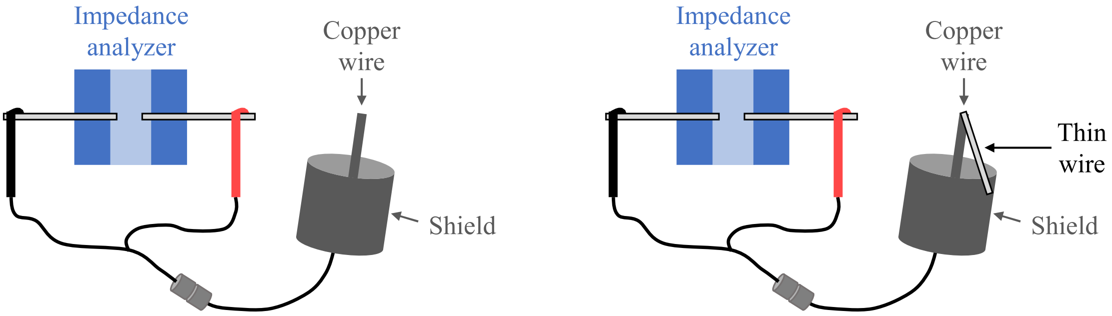

(a) *(b)*

Figure 3.7: Illustrations of zero adjusting cables for an Impedance analyzer. (a) Zero open adjusting. (b) Zero short adjusting.

A frequency sweep from 100 k to 1 MHz at a frequency step of 1 kHz is executed for each transducer in air and water, obtaining $Y(f)$.

3.4.3 Source sensitivity

The measurement setup used for the sensitivity measurements is the acoustic measurement setup described in Chap. 3.1.1 excluding the presence of the steel plate. The transducer and hydrophone were aligned on the acoustic axis, approximately along the z-axis, at a distance of 0.87 m from each other, which is the maximum possible distance in the tank setup. Then, a frequency sweep from 200-1000 kHz was executed with a step frequency of 1 kHz for two measurements. One was conducted by measuring the input voltage over the water-immersed transducer, $V(f)$, and the other one was conducted by measuring the pressure at the respective distance with the hydrophone. Subsequently, the latter measurement was corrected for the effects of the instruments and cables not present in the first measurement imposed. Additionally, the water's absorption was accounted for before it was extrapolated to 1 m resulting in $P(z = d_0 = 1m, \theta = 0, f)$. The sensitivity is then calculated by Eq. (2.5).

As stated in Chap. 3.1.1, this measurement was conducted using hydrophone SN 1848, and therefore calibration data for hydrophone SN 1820, preamplifier PA110078 and DC coupler DCPS223 from NPL UK was used when correcting for this hydrophone and the other two instruments. Aanes measured the response of the instruments used in his dissertation [8]. The amplifier working in 40 dB mode exhibited a relatively flat response in the frequency range 200-1500 kHz, and thus a constant amplification factor of 45.74 dB was applied to all frequencies [8]. A larger variation between -1.3 to 0.5 dB in the frequency range 100-1500 kHz was found in the gain imposed by the Krohn-Hite filter model 3202, shown in Fig. 3.3 in [8]. This is utilized and taken into account for each frequency for the Krohn-Hite filter model 3940 used in this thesis.

3.4.4 Beam pattern

The measurement setup used for beam pattern measurements is the acoustic measurement setup described in Chap. 3.1.1 without the presence of the steel plate. In directivity measurements, the instruments are also aligned on the acoustic axis, approximately along the z-axis, where the 0° degree angle is defined. The directivity is measured one frequency at a time while using the Micos rotary stage to rotate the transducer. The frequencies 370, 420, 520, 575, 630, 760, 850 and 1000 kHz where measured for angle area -45° to 45° with steps of 0.2° obtaining $P(z = d, , f)$. The beam pattern is then calculated by Eq. (2.6). The hydrophone SN 1820 was used in these measurements and even though the hydrophone SN 1820 was compromised related to absolute response, directivity measurements are normalized and is therefore relative measurements. Hence, the results were deemed acceptable.

Additional challenges were encountered here. In order to become familiar with the measurement setup and reproduce Aane's results, directivity measurements were focused on first. When instrumental settings where set, full directivity measurements where executed before sensitivity measurements. For directivity measurements to be done correctly without having to correct results afterwards, the holder for the transducer is supposed to be adjusted to the transducer so that when the transducer is rotated in the x,z-plane, the front surface's center is at rest. It was discovered that this was not correct when attaching Prøytz' transducers, since these are longer. Therefore, a new holder with a set screw was produced by the institutes work shop to fit those.

The measurements per frequencies where executed consecutively in ascending frequency order at a constant immersion time of the hydrophone per transducer. Regarding the stabilization of the hydrophone, as it is recommended to be immersed one hour prior to measurements, only the angle area from -45° to -35° for the lowest frequency, 370 kHz, could be affected by this. This is calculated from the time it takes to measure one beam pattern, which was 7 hours.

3.4.5 Transmission measurements

The transmission measurements are carried out by conducting two separate measurements: one without the steel plate and another one with the steel plate positioned between the transducer and the hydrophone. For the measurement without the steel plate the distance between the transducer and the hydrophone is 270 mm where $p_i(0,z_0,f)$ is measured. For the measurement with the steel plate, the distance between the transducer and the steel plate is 270 mm, and the distance between the steel plate and the hydrophone is 100 mm. The total distance between the transducer and hydrophone is then 376.05 mm, which includes the 6.05 mm thickness of the steel plate and this is where $p_i(0,z_0,f)$ is measured. As mentioned in Chap. 3.1.3, the distances is found by using reference rods of 270 mm and 100 mm and the hydrophone is positioned at the acoustic axis of the transducer.

A frequency sweep from 350-1000 kHz is performed for both measurements, after which the transfer function is calculated by Eq. (2.42).

3.5 Challenges and investigations

There have been multiple challenges and investigations regarding the acoustic measurement setup.

3.5.1 Instrument settings

To commence, one of the objectives in this thesis was to replicate Aanes' measurement results with transducer MA by using identical settings [8], and subsequently expand measurements to include CP1 and CP2. Starting with directivity measurements at resonance frequency 575 kHz, the results had considerable noise and fluctuations. Consequently, a comprehensive evaluation of all the settings was required. Investigations revealed that the current setup is slightly different than in 2013 [8] due to it being moved from one position to another inside the laboratory in 2017, resulting in a smaller z-range. This affects the sensitivity measurements, as the distance Aanes used, $d = 0.9065$ [8], is not possible in this thesis. In addition, Aanes may have used additional rubber mattresses in the tank and placed them differently in the tank. This can all be causes leading to difficulties reproducing his results. Therefore, the priority shifted to refining the measurement setup and its settings. Regular checks were performed to ensure proximity to Aanes' results.

While observing the signal live on the oscilloscope, the burst rate and band pass filter settings were analyzed. It was determined that a burst rate of 10 was necessary instead of 50 [8], to avoid interference from a diffuse noise field of high magnitude. Additionally, the band-pass filter was adjusted from a constant filter of 20 kHz to 2 MHz [8], covering all frequencies measured, to a moving filter from $(400/575)\cdot f$ to $(800/575)\cdot f$, which was determined at the frequency 575 kHz. The number of samples averaged over per point was set to 512 instead of 256 [8] to obtain even more stable results.

During these directivity measurements, it was discovered that the transducer rotated considerably in the holder around its own axis while being rotated by the Micos rotary stage in the xz-plane, due to stress from the cable and lack of friction in the holder. As a solution, the institute's workshop installed a set screw to stabilize the system. The transducer was found to be non-axisymmetric, meaning that the rotation of the transducer in the holder plays an important role in the experimental setup. Later, a second set screw was found to be oriented towards the wall. However, there is no record of Aanes or Prøytz observing this detail. In addition, no information was uncovered pertaining to the rotation of the transducers, leaving it unknown as to whether or not they employed the set screw in question. At the frequency of 575 kHz, four measurements of MA were taken at rotation angles in the holder at 0°, 45°, 90° and 135° relative to an arbitrary set 0° angle. Settings were as in Sec. 3.1.2 except the number of samples averaged over was reduced to 64 to save time and the distance between the transducer and the hydrophone was 0.5 m. These measurements are presented in Fig. 3.8a displaying clear asymmetry. The rotation of 90° shows the best agreement with Aanes' results at the first side lobes, and Fig. 3.8b shows this compared to Aanes' measurement. Thus, this angle has been designated as the default zero angle and will be treated as such henceforth. This particular rotation transducer coincides with an engraved number 3, indicating prototype 3, orientated in the $+y$-direction, as mentioned in Chap. 3.3. As regards to transducers CP1 and CP2, solely a minor angle region of the beam pattern at frequency 575 kHz was measured by Prøytz, displaying substantial fluctuations [23] in addition to the transducers' possible rotation during the measurements is the set screw was not employed. Consequently, the identification of the corresponding rotation angle was not pursued by this author. Instead, the rotations were selected and specified for the sake of reproducibility and comparability in the current study and future research pursuits. Markings are stated in Sec. 3.3.

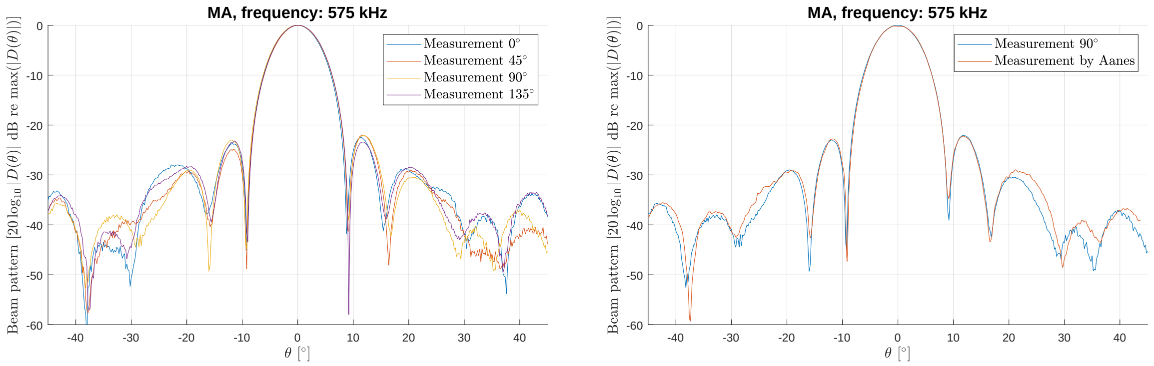

(a) *(b)*

Figure 3.8: Comparison of measurements for MA of beam pattern at frequency 575 kHz. (a) At rotations 0°, 45°, 90° and 135° in the holder. (b) Rotation 90° and measurement from [8].

A directivity measurement at the distance of 0.63 m, equal to the later directivity measurements, was conducted using the reviewed settings and setup, as stated in Sec. 3.1.2. The beam pattern and raw data from the left side of the beam pattern at angles 0°, -9.2°, -12°, -16°, and -19.6° are displayed in Figs. 3.9a and 3.9b-3.9f, respectively, where the chosen MW is indicated by a black rectangle. The raw data shows a stable signal at the main lobe with reflections that interfere around 500 μs, as seen in Fig. 3.9b and the stability of the signals amplitude decreases with the increasing order of side lobes resulting in more fluctuations at the side lobes.

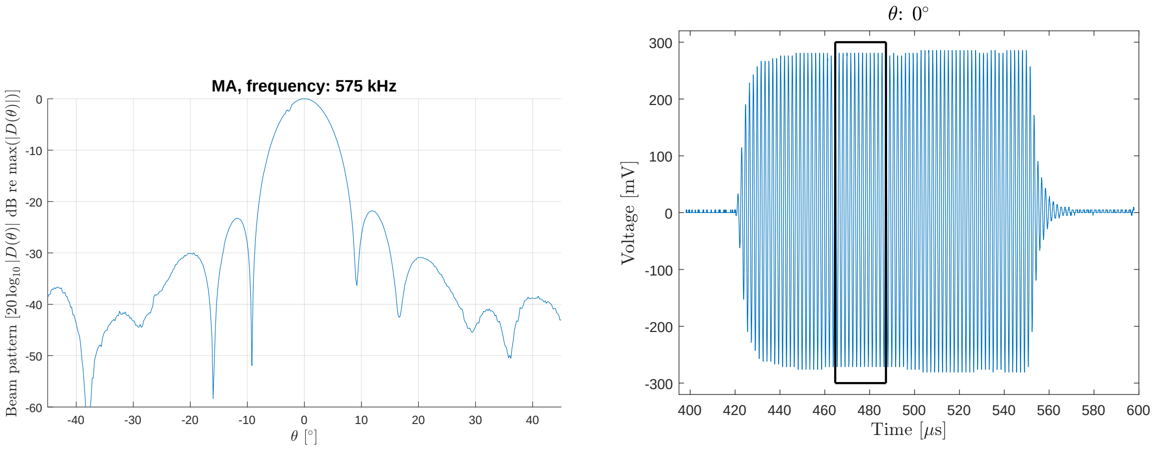

(a) *(b)*

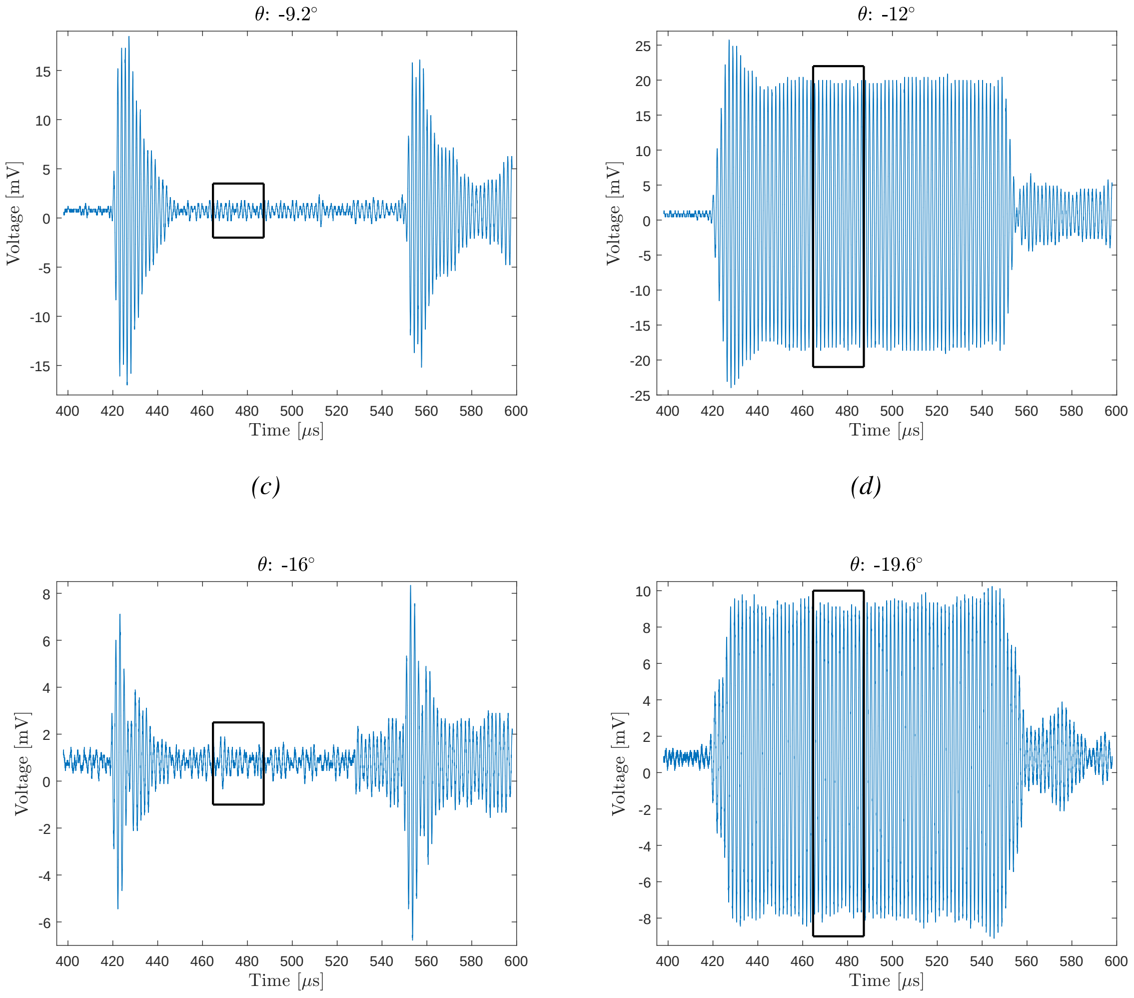

(c) *(d)*

(e) *(f)*

Figure 3.9: Measurement with MA at frequency 575 kHz with the reviewed settings. (a) Beam pattern. (b)-(f) is raw data from the measurement shown in (a) including the measurement window chosen: (b) Raw data at main lobe, $\theta = 0°$. (c) Raw data at first left dip, $\theta = -9.2°$. (d) Raw data at first left side lobe, $\theta = -12°$. (e) Raw data at second left dip, $\theta = -16°$. (f) Raw data at second left lobe, $\theta = -19.6°$.

3.5.2 Alignment and distance measurements

The acoustical distance method was attempted, which entails measuring the transit time of a pulse and determining the sound velocity in water to calculate the distance using the formula distance $=$ time$/$sound velocity. A comparison between this method and the results obtained using a simple steel measuring tape revealed a discrepancy of around $5-6$ mm, rendering the acoustical distance method unsuitable for use in this thesis. The observed inaccuracies in the acoustical distance method may be attributed to system time delay, uncertainties regarding the defined start of the signal, and uncertainties in the determined water velocity. Consequently, the steel measuring tape method was used instead.

3.5.3 Data processing

The effects of choosing the MW of a measurement is demonstrated in Figs. 3.10 and 3.11. The measurement is the beam pattern at frequency 1000 kHz for MA with settings stated in Chap. 3.1.2, where the distance is 0.63 m and the reflections occur 109.5 μs after the direct signal. Fig. 3.10 shows raw data waveforms extracted from a beam pattern measured at frequency 1000 kHz for MA, where *(a)* shows the first left dip and *(b)* shows the first left side lobe. These were chosen to clearly illustrate the differences in amplitude, as the differences in the raw data at the main lobe are not always detectable. A significant difference in the amplitude is observed between the MW, prior to the reflection, and $\mathrm{MW}_{\mathrm{reflection}}$, which is during the interference of the reflection. $\mathrm{MW}_{\mathrm{reflection}}$ is decreased in *(a)* and increased in *(b)* relative to MW. The unfolds clearly Fig 3.11

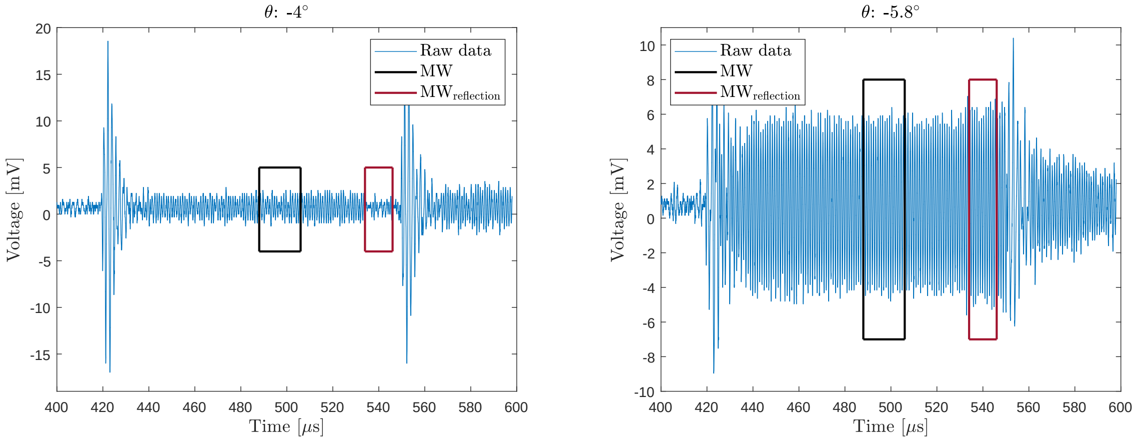

(a) *(b)*

Figure 3.10: Raw data from the beam pattern at frequency 1000 kHz for transducer MA measured at 0.63 m resulting in reflections 109.5 μs after the direct signal. MW , before the reflection occurs, and $MW_{reflection}$, while the reflection is affecting is shown. (a) First left dip, $\theta = -4°$. (b) First left side lobe, $\theta = -5.8°$.

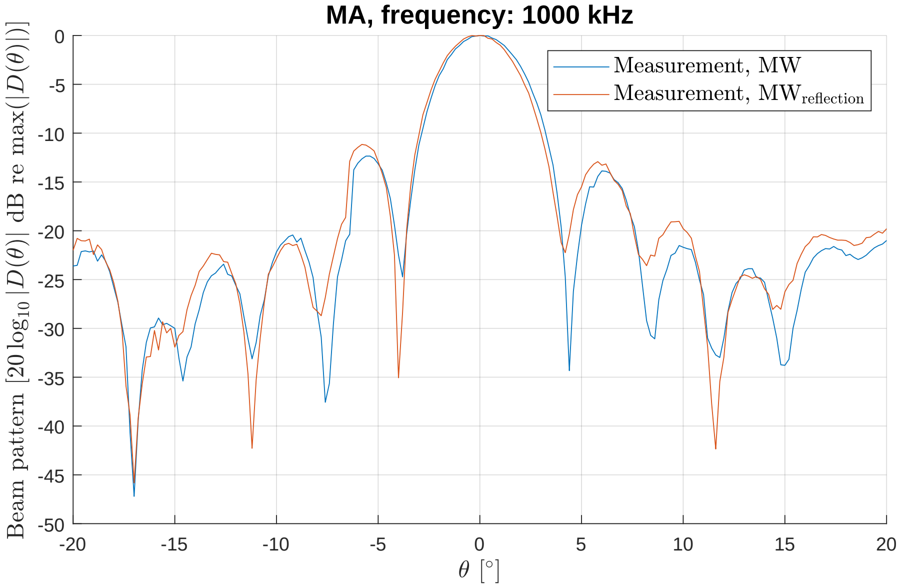

Figure 3.11: Beam pattern at frequency 1000 kHz for transducer MA measured at 0.63 m resulting in reflections 109.5 μs after the direct signal. A comparison showing the impact the two different MWs shown in Fig 3.10 has. MW is before the reflection occurs and MW$_{reflection}$ is while the reflection is affecting.

3.5.4 Sensitivity measurement

There were some challenges when measuring the sensitivity. Originally, the hydrophone of SN 1820 was intended to be used for all measurements, as it has been used by [8] and [23]. Moreover, calibration data is available for this hydrophone for all measured frequencies and it has been calibrated together with the preamplifier and DC coupler in place. However, there were challenges with the sensitivity results using this hydrophone. Looking at sensitivity measurements, results for all three transducers had a frequency-depended tilt upwards compared to the documented measurements and simulations by Aanes [8] and Prøytz [23], in addition to this author's simulations. The measurements raw data were assumed acceptable considering that the sensitivity results, excluding the tilt, had a fair agreement with the curvature of measurements and simulations by Prøytz [23] and Aanes [8], but at a lower level. The biggest difference from Aanes and Prøytz measuring setup that could alter the signal is the filter. They used a fixed bandpass filter from 20 kHz to 2 MHz covering all the measured frequencies, whereas a moving filter more concentrated around the respective frequencies [(400/575)·f - (800/575)·f] Hz is used in this thesis. A measurement with an averaging over 256 samples and the filter from 20 kHz to 2 MHz showed no significant difference regarding a tilt. Further on, the correction of each instrument's effect on the signal was explored, where the correction for the hydrophone, preamplifier and DC coupler seemed to be the only ones to give this frequency-dependent tilt upwards. Looking at the calibration data, both Aanes' calibration [8] and the NPL calibration [31] gave similar results. Reconsidering the measurements data, specifically looking at the hydrophone, the needle hydrophone of SN 1820 [31] used at first was replaced by the other needle hydrophone SN 1848 [32] to assess the instrument itself. A measurement with an averaging over 256 with this hydrophone gave the desired outcome, no clear frequency-dependent upward tilt, but with a decreased sensitivity following approximately the same curve path as Aanes [8] and Prøytz [23]. New measurements with hydrophone SN 1848 were conducted.

The instruction manual for the hydrophones [50] stated that the hydrophone should be immersed in water for approximately 1 hour before conducting measurements, although most hydrophones stabilize after about 10 minutes, and to have an immersion time of preferably 12 hours or less. For immersion times longer than 24 hours, the hydrophone should be removed as soon as possible and dried out. Even though the hydrophone SN 1820 has been used in several studies, it has not been calibrated since 2011 by NPL and Aanes [8]. During the summer of 2022, the hydrophone was unfortunately forgotten immersed in water for weeks and this author has since conducted several measurements with the hydrophone immersed in water for up to a week at a time. This is probably the reason the hydrophone is compromised, considering Prøytz achieved a high level of agreement with Aanes when measuring sensitivity for his transducer in 2022 [23]. The interchangeable probes must be handled with extreme care, not even touching the tip, but there is no reason to believe this has not been done properly by experienced personnel. The hydrophone has also not been submerged in water for a full hour before all the sensitivity measurements, but due to the time it takes to align them with the acoustic axis, at least 15 minutes have passed for those measurements concerned.

Chapter 4

Simulation

This chapter presents the simulation setup, providing details on the specific program files utilized for the simulations conducted in this thesis and associated parameters. Given that FEMP entails simulating the transducers' properties by striving to replicate the transducers as accurately as possible based on their dimensions and material parameters, the meshes employed in the simulations are presented in addition to the challenges faced. In the ASM2 simulations, a simple baffled piston represents the different transducers by varying the radius of the piston.

4.1 FEMP

4.1.1 Setup

For the usage purpose of FEMP in this thesis, four files need to be altered or constructed, ”read_inn_project.m”, ”init_const_project.m”, an ”_.inn”-file and a ”material*(integer)*.dat”, where the integer specifies the material file. In the main file, ”read_inn_project.m”, points, structure, areas and boundary conditions are defined. Together with ”init_const_project.m”, it calls upon an ”_.inn”-file, where the following is defined: dimensions of the structure, number of elements in the structure and fluid, the radius from origo to the boundary dividing the finite and infinite fluid region, R_{inf}, the material file number, the highest frequency to set the elements per wavelength, the order of finite and infinite elements, the frequency range and the type of simulation, e.g. direct harmonic analysis for sensitivity. It also calls upon a ”material_.dat”-file, specified by an integer through the ”.inn”-file, where the characteristics of the materials and fluids involved are defined. Respective examples of this are shown for transducer CP1 in App. A.1, A.2, A.3 and A.4.

In the setup, dimensions listed in Table 3.2a is used for MA, and dimensions listed in Table 3.2b is used for CP1 and CP2. Materials are listed in Table 3.3 for all transducers and specific details regarding characteristics can be found in App. A.4, [8] and [23].

The following settings, obtained from Aanes [8] and Prøytz [23], are consistent across all simulations for the three transducers, enabling direct comparison with their respective simulations. The number of nodes is 8, which corresponds to 2nd order finite element and 12th order infinite elements [27]. $R_{\text{inf}} = 80$ mm which is well above the minimum requirement stated in Eq. (2.7) in Chap. 2.4 and the highest frequency to set the elements per wavelength is 1 MHz. The number of elements per wavelength, is equal to 3 in the transducer and finite fluid region, and equal to 1 in the infinite fluid region. One exception is made for a segment in CP1 and CP2 indicated in Fig. 4.1 where the elements per wavelength were set to 29 due to failure in some calculations by FEMP. This is further elaborated in Chap. 4.1.2. The frequency range is equal to the ones stated for the respective measurements in Chaps. 3.4.2-3.4.4.

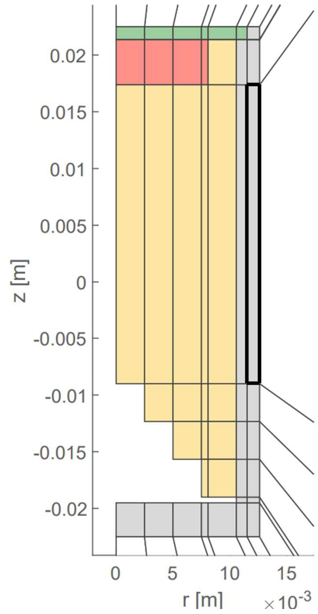

Figure 4.1: Example fluid segment CP1

FEMP simulates a cross section of the transducers along the z-axis and assumes axisymmetry as aforementioned in Chap. 2.4. Decimated meshes at frequency 50 kHz are shown for MA, CP1 and CP2 in a fluid in Figs. 4.2-4.4, respectively. (a) shows a close-up of the transducers and (b) shows the transducers surrounded by the finite fluid region, white region, which borders the infinite fluid region, blue region.

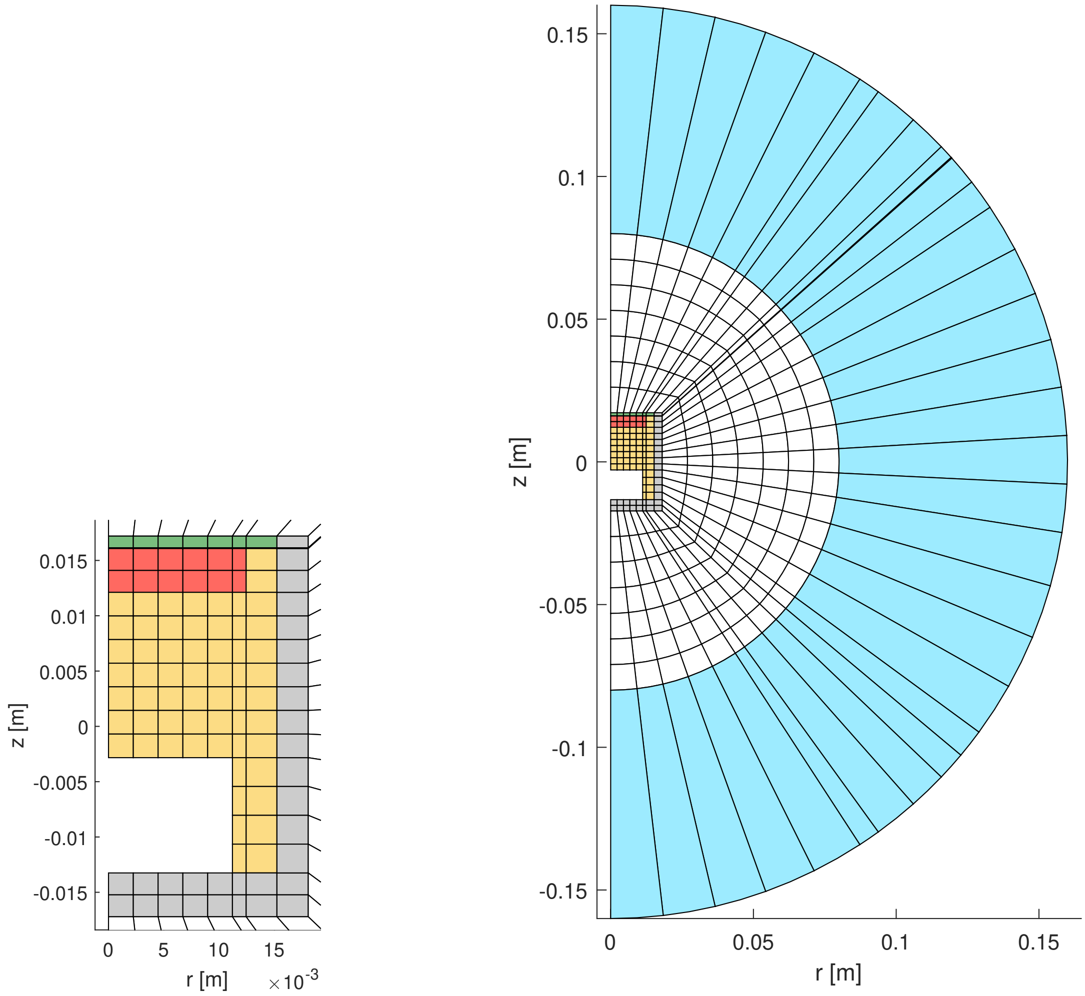

(a) *(b)*

Figure 4.2: Decimated mesh at frequency 50 kHz in FEMP for MA in a fluid divided into two regions: White finite region and blue infinite region. (a) Mesh of the transducer. (b) Mesh of the transducer and the fluid .

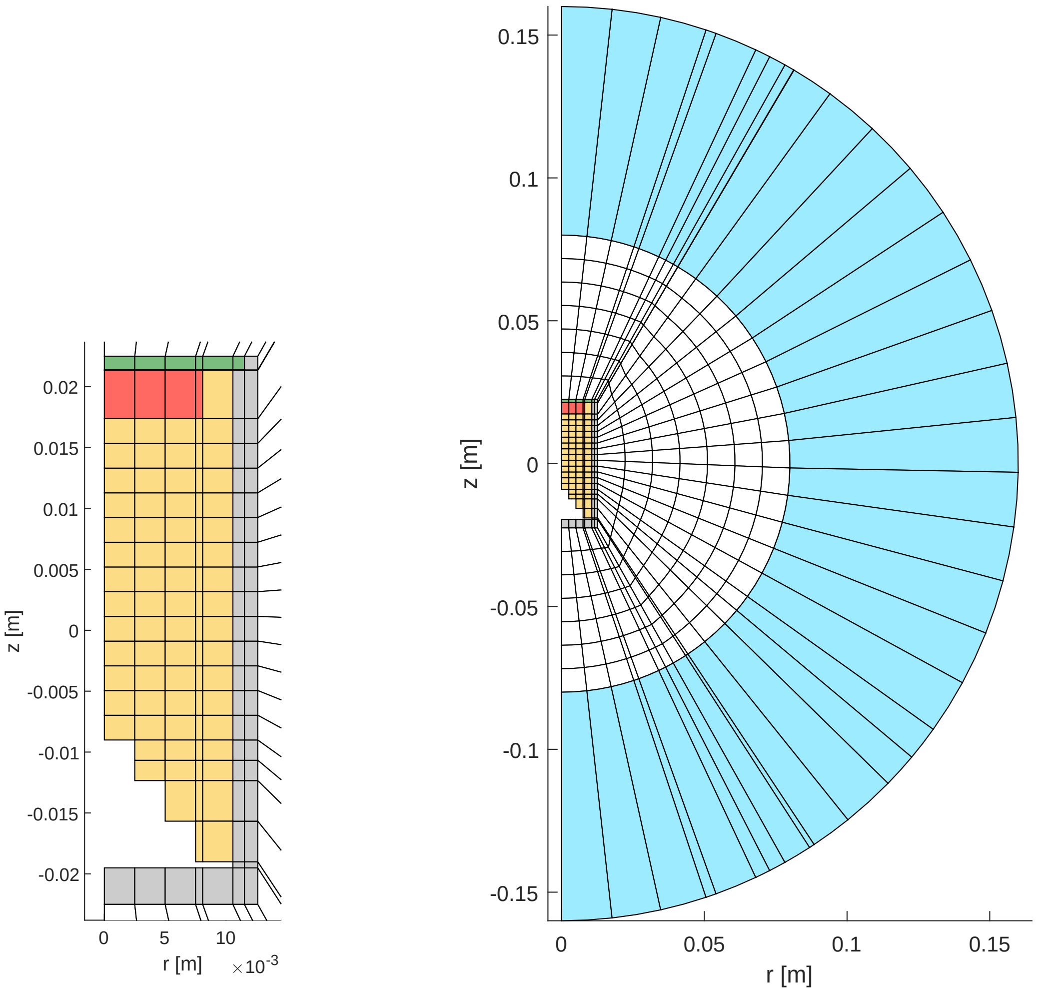

(a) *(b)*

Figure 4.3: Decimated mesh at frequency 50 kHz in FEMP for CP1 in a fluid divided into two regions: White finite region and blue infinite region. (a) Mesh of the transducer. (b) Mesh of the transducer and the fluid .

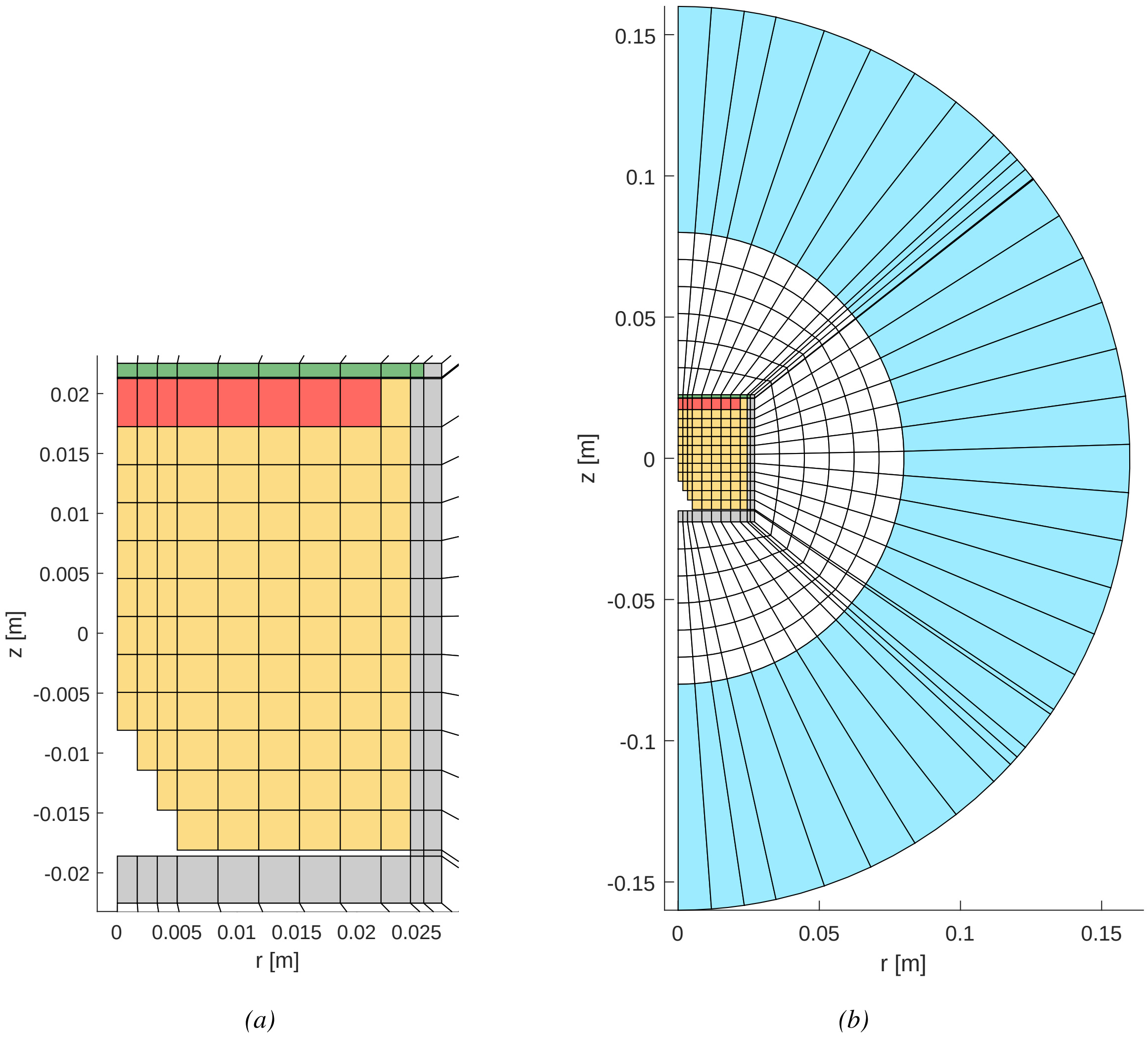

Figure 4.4: Decimated mesh at frequency 50 kHz in FEMP for CP2 in a fluid divided into two regions: White finite region and blue infinite region. (a) Mesh of the transducer. (b) Mesh of the transducer and the fluid .

4.1.2 Investigations mesh

An issue regarding the resolution was discovered. The version FEMP 6.1, used in this thesis, does not always calculate correct elements per wavelength in the fluid [51]. Investigations revealed no discrepancies in the transducer structure for any of the three transducers. However, upon closer examination of the outermost boundary of the finite fluid region, at R_{inf}, it was observed that a particular segment within the finite fluid failed to meet the stated settings of at least 3 elements per wavelength. This segment neighbors a segment of the steel casing in the transducer structure.

In order to resolve this issue, adjustments of elements per wavelength were implemented on the steel casing segment of the transducer's structure to force correct calculations out at the border R_{inf}. Each segment in the finite fluid has four boundaries with respective neighboring segments: One inner linear boundary it shares with a transducer segment of length l_t, one outer radial boundary it shares with an infinite fluid segment at R_inf of length l_Rinf, and two linear boundaries on each side they share with other finite fluid segments. Fig. 4.5 shows an illustration of a segment in the finite fluid region.

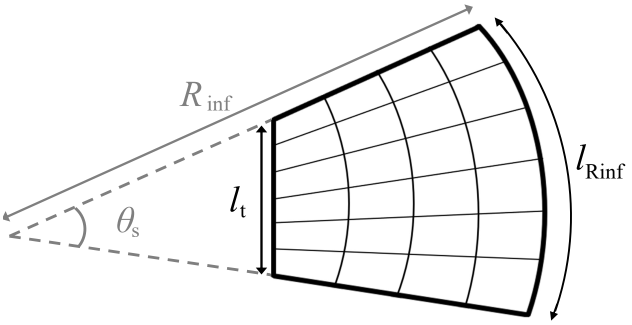

Figure 4.5: Example of a segment in the finite fluid neighboring a transducer segment, an infinite fluid segment and two other finite fluid segments.

Because the segments in the fluid expand radially outwards, the calculations are made to fit the elements along the outer boundary, i.e. the largest elements. The length of the outer boundary, l_Rinf is calculated by finding the respective angle that contains it and multiplying it with the radius, $l_\mathrm{inf} = \theta_\mathrm{s} \cdot R_\mathrm{inf}$. The total elements required for the length l_Rinf can then be found by

$$\mathrm{Tot_{El}} = \frac{l_\mathrm{Rinf}}{\lambda_\mathrm{w}} \cdot \mathrm{El}/\lambda_\mathrm{w} = \frac{l_\mathrm{Rinf} \cdot f}{c_\mathrm{w}} \cdot \mathrm{El}/\lambda_\mathrm{w}, \tag{4.1}$$

where $\mathrm{Tot_{El}}$ is the total number of elements along the boundary, $\lambda_\mathrm{w} = c_w/f$ is the wavelength of sound in the fluid in this segment where c_w is the sound velocity in the fluid and the frequency is the highest frequency simulated, and $\mathrm{El}/\lambda_\mathrm{w}$ is the set elements per wavelength controlling the accuracy. Further on, elements per wavelength for the respective transducer segment are then calculated by

$$\mathrm{El}/\lambda_\mathrm{t} = \mathrm{Tot_{El}} \cdot \frac{\lambda_\mathrm{t}}{l_\mathrm{t}} = \mathrm{Tot_{El}} \cdot \frac{c_\mathrm{t}}{f \cdot l_\mathrm{t}}, \tag{4.2}$$

where $\lambda_\mathrm{t} = c_t/f$ is the wavelength of sound in the segment of the transducers material dependent on the shear sound velocity c_t of the respective transducer segment material, and l_t is the length of the shared boundary.

The specific versions of FEMP software that have this issue are currently unknown. Upon examining the decimated meshes in Aanes' [8] and Prøytz' [23] thesis, it appears that only Prøytz' meshes have been affected. Aanes used FEMP 5.0 and Prøytz used both FEMP 5.0 and 6.1b. However, the impact of these changes on sensitivity and directivity simulations was investigated for sensitivity and directivity at the frequencies specifically focused on in this thesis, where no effect was found. Nevertheless, the changes were retained as they conform to the expected functionality of FEMP, and could be significant in an unknown capacity.

Several attempts were made to replicate Aanes' FEMP simulations [8] for MA using the dimensions listed in Table 5.9 in [8] and material data presented in Chap. 5.2 in [8], without success. A difference between the radius of the air pocket, R_{air} listed in Table 5.9 in [8] and the decimated mesh in Fig. 4.16 in [8] was found where $R_{\mathrm{air}} = 4.01$ mm for the decimated mesh. This was implemented in this author's dimensions in Table 3.2a and simulations but did not give a significant agreement with Aanes' results either. Fig. 4.6 shows a comparison of these FEMP simulations with simulations from [8] where (a) shows the sensitivity and (b) shows the beam pattern at frequency 575 kHz. Access to Aanes' private data from his work [52] contained on a hard disk was given, but no files corresponding to the results presented in his thesis were found. The search ended here due to time constraints. For these reasons, only FEMP simulations by Aanes [8] is used to compare with when available.

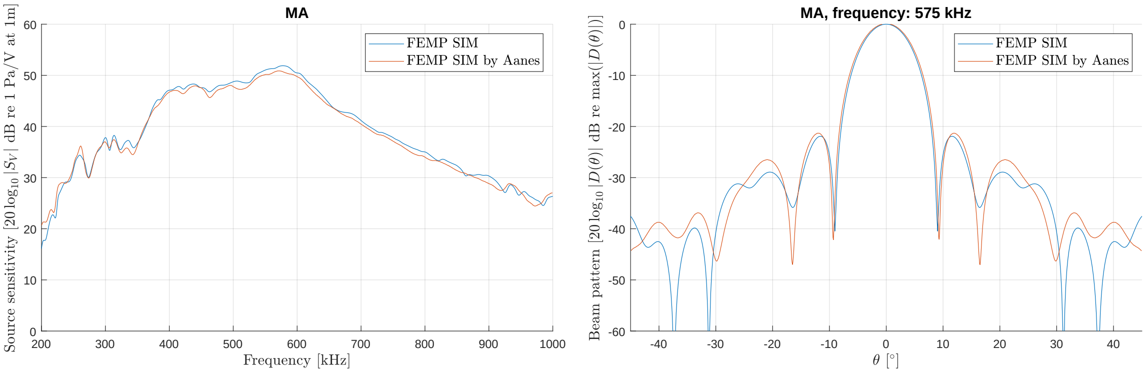

(a) *(b)*

Figure 4.6: Comparison between FEMP simulations for MA by this author and Aanes [8]. (a) Sensitivity. (b) Beam pattern at frequency 575 kHz.

Several attempts were also made to replicate Prøytz' FEMP simulations [23] for CP1 and CP2, using the dimensions listed in Tables 6.16 and 6.15 in [23], respectively, and material data presented in Chap. 3 in [23], without success. With access to Prøytz private data [53] online at google disc, several files of FEMP simulations showing a high level of agreement with sensitivity simulations in Prøytz' thesis were found. In these files, the structure of the transducers in the simulated mesh had four differences; T_{c1}, T_{c2} and R_{air} had different values than given in [23], and an air gap, T_{gap}, in the bottom was found. In Chap. 5.7 in [23], Prøytz states that vacuum gaps used in simulations were to be explicitly described when used. Considering no vacuum gap is described for any of the six transducers made in [23], it is assumed that this could be the case for CP1 and CP2. Therefore, these changes were implemented in Table 3.2b and simulations, in addition to T_{c1f}, which was not given in [23], but was also found from the same meshes in these files. This gave a fair agreement with sensitivity simulations by Prøytz [23], as shown in Figs. 5.8 and 5.9.

As for the electrical admittance simulations in air and water shown in Figs. 5.3-5.4 and 5.5-5.6 , there were some deviations compared to simulations by Prøytz [23], mostly for CP2. However, the simulations of CP2 in water showed a similar curvature to measurements conducted by this author despite them both having a big discrepancy compared to simulations and measurements by Prøytz [23]. Therefore, FEMP simulations by this author are included when comparing measurements to simulations, alongside simulations conducted by Prøytz [23].

4.2 ASM2

For the usage of ASM2 for this thesis, two files are altered, ”ASM_Adapt_FilonGauss.m” and ”FunctionsParent.m”. In the main file, ”ASM_Adapt_FilonGauss.m”, the following are defined: the frequency range, position of measuring point, (z,r), an argument as to whether it is a free field simulation or transmission through a plate simulation, the absolute local error tolerance in the first and last Gauss adaptive method and the Filon-type, and in second Gauss method around the peak, initial staring step size, the upper integration limit and the limit where the Filon method kicks in. When the argument is set for plate simulation, the file recalls values from file ”FunctionsParent.m” where the fluid’s velocity and density, the pistons radius and particle velocity, the plates density, compressional wave velocity, shear wave velocity and thickness, and the distance between the piston source and plate is defined.

Distances and frequencies are equal to the ones stated in the measurements described in Chap. 3.4.5, except a frequency step of 0.2 kHz is used instead of 1 kHz. The absolute local error tolerance is 10^{-1} Pa for every η-step in the numerical integration. The initial staring step size is 10^{-3} rad/m, the upper integration limit is 200 rad/m and the parameter determining when the Filon method kicks in is set to 0.2 rad/m. The piston’s particle velocity is 1 m/s and for the fluid, the density is 1000 kg/m^{-3} and the velocity is 1485 m/s. For the plate, the density is 8000 kg/m^{-3}, the compressional wave velocity is 5780 m/s, the shear wave velocity is 3130 m/s and the thickness is 6.05 mm [2]. The radius of the piston varies.

Simulations are conducted for transducers MA, CP1 and CP2, which has the ka-numbers 17, 26 and 46. For these, the effective radius is implemented, found from the beam pattern and calculated using Eq. (2.3), as described in Chap. 2.3.1.

A further simulation study is conducted for ka-numbers 1, 3, 5, 10, 36, 52, 60 and 100 initially. The radii are found simply from $\text{ka} = k \cdot a \ \rightarrow \ a = \text{ka}/k$, calculated for frequency 500 kHz, same as for MA, CP1 and CP2, which gives the respective radii a = 0.47, 1.42, 2.36, 4.73, 17.02, 24.58, 28.36, 47.27 mm.

Chapter 5

Results and discussion

This chapter presents the results from measurements and simulations conducted in this thesis and compares this to relevant prior work. Starting with the transducer properties, electrical admittance, sensitivity and beam patterns are presented. Beam transmission is divided into two parts where the first part presents the measurements and corresponding simulations, discussing similarities and differences and phenomena happening, especially in the frequency bands associated with the Lamb modes. Then, a further simulation study, accounting for several more ka-numbers, is presented while continuing the discussion of the phenomena. This is compared to a similar study of varying distances instead of ka-numbers.

5.1 Electrical admittance

Figs. 5.1-5.2 shows the measurements for the electrical admittance in air and water for MA, respectively, where measurement by this author and measurements and simulations by Aanes [8] is compared. For the susceptance, there are only measurements conducted by this author as there is no measurement or simulation of the susceptance in Aanes' thesis [8]. Figs. 5.3-5.6 shows the measurements for the electrical admittance in air and water for CP1 and CP2, respectively, where measurements and simulations conducted by this author and Prøytz [23] are compared. For CP1 in air and water and CP2 in water, the simulations by Prøytz lie approximately over the simulations by this author showing their proximity.

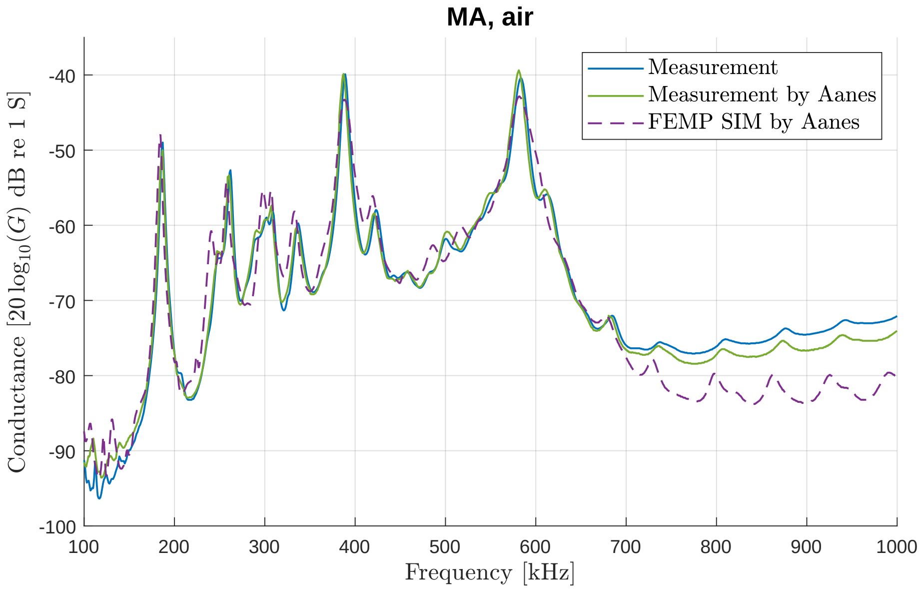

(a)

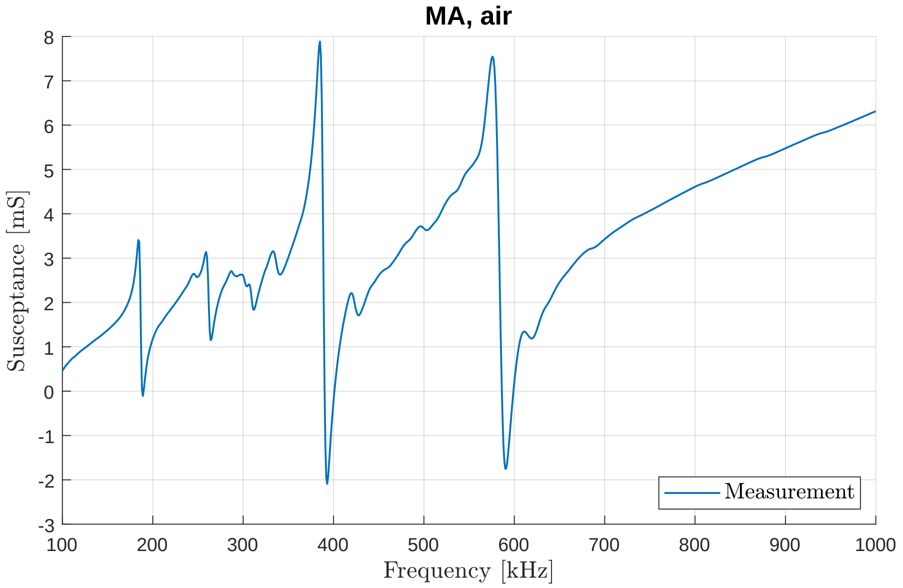

(b)

Figure 5.1: Electrical admittance for transducer MA in air. (a) Conductance: Comparison of measurements by this author and measurements and FEMP simulations by Aanes [8]. (b) Susceptance: measurement by this author.

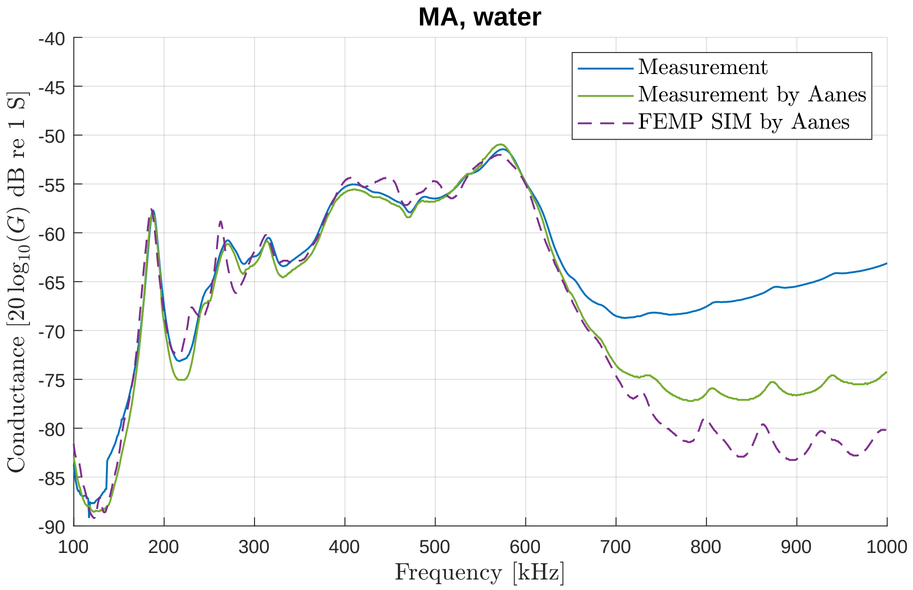

(a)

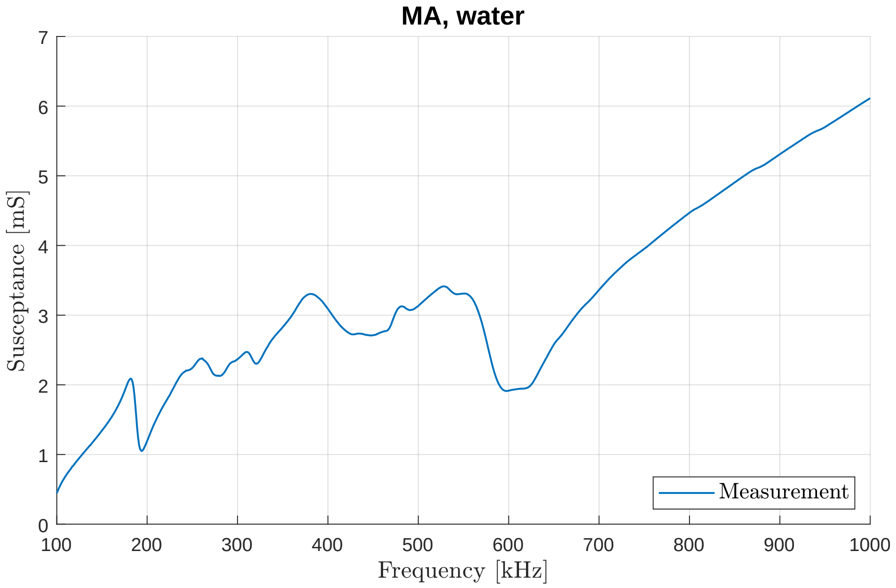

(b)

Figure 5.2: Electrical admittance for transducer MA in water. (a) Conductance: Comparison of measurements by this author and measurements and FEMP simulations by Aanes [8]. (b) Susceptance: measurement by this author.

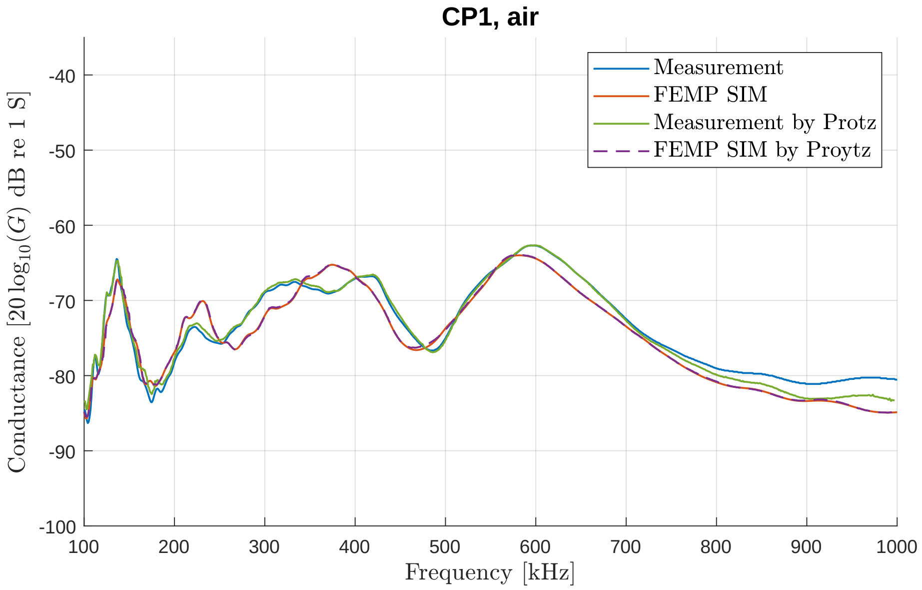

(a)

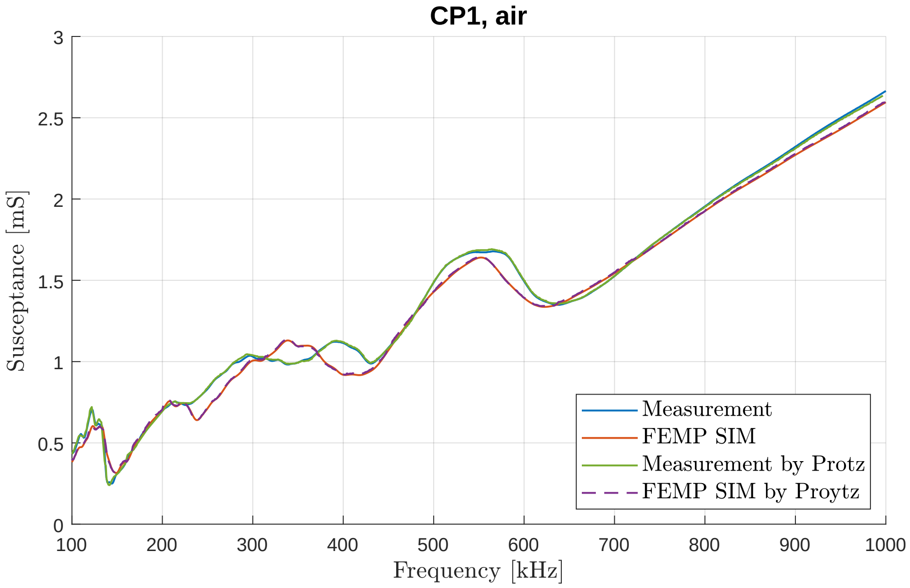

(b)

Figure 5.3: Electrical admittance for transducer CP1 in air. Comparison of measurements and FEMP simulations by this author and Prøytz [23]. (a) Conductance. (b) Susceptance.

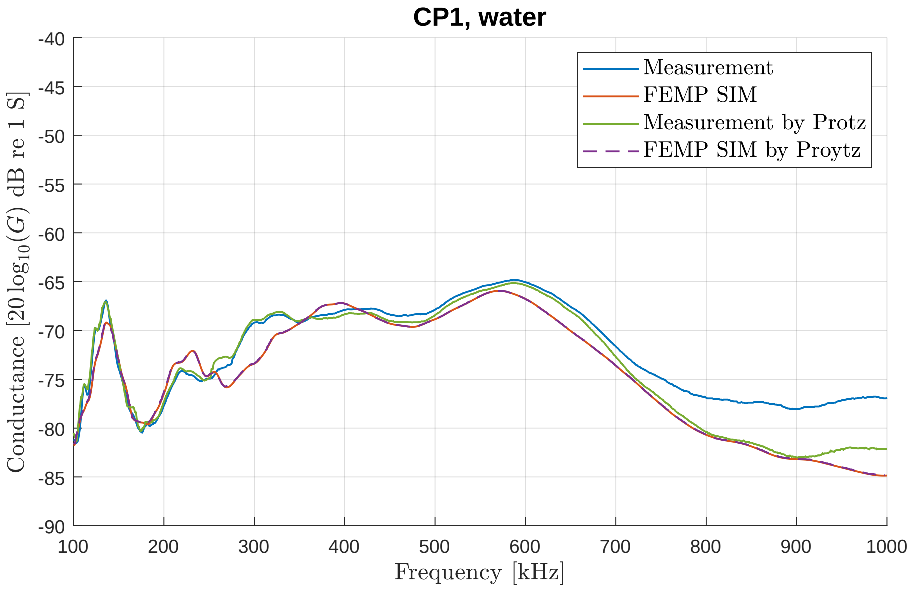

(a)

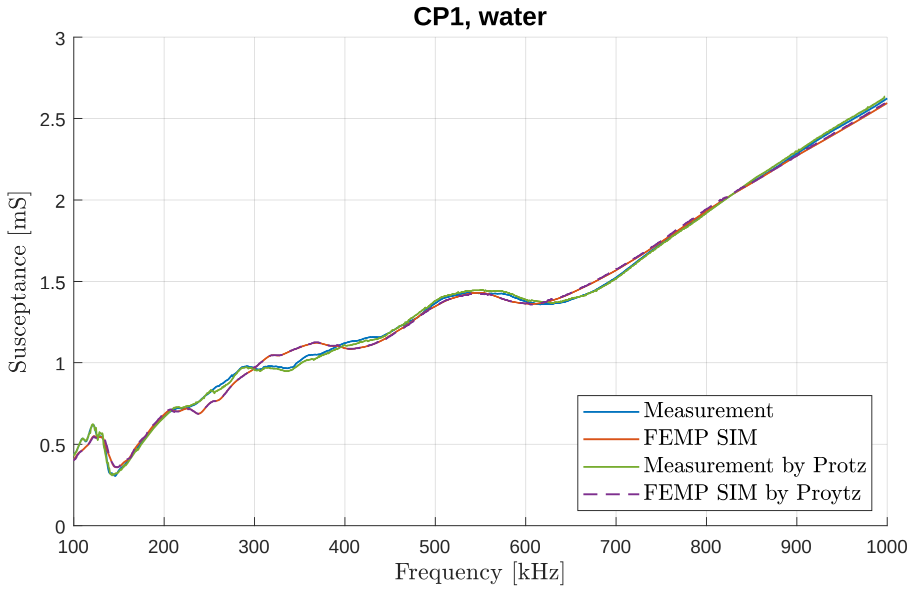

(b)

Figure 5.4: Electrical admittance for transducer CP1 in water. Comparison of measurements and FEMP simulations by this author and Prøytz [23]. (a) Conductance. (b) Susceptance.

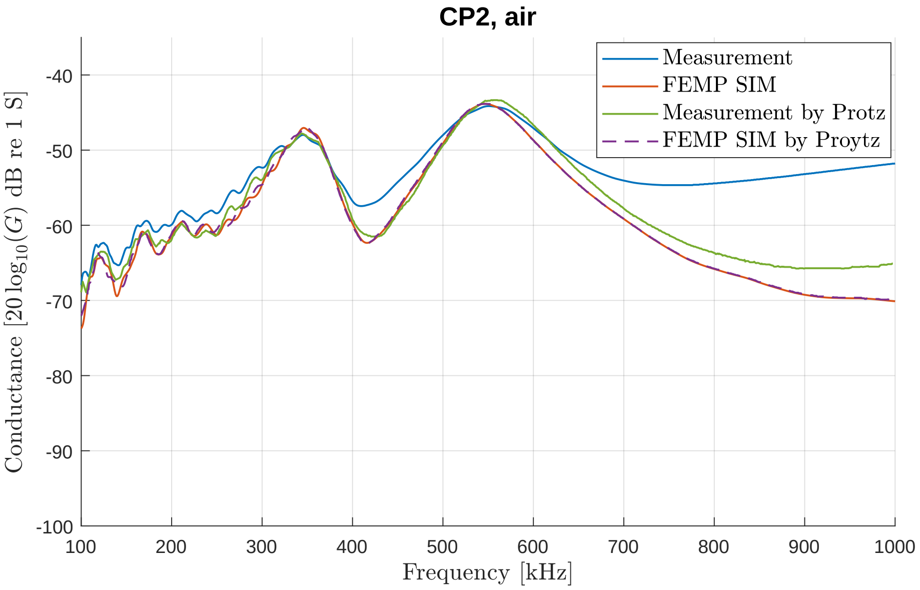

(a)

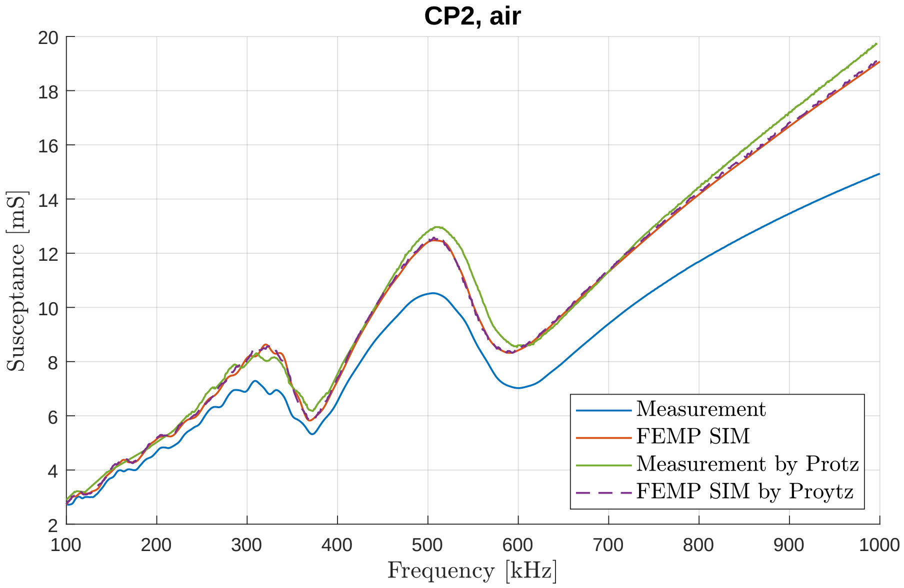

(b)

Figure 5.5: Electrical admittance for transducer CP2 in air. Comparison of measurements and FEMP simulations by this author and Prøytz [23]. (a) Conductance. (b) Susceptance.

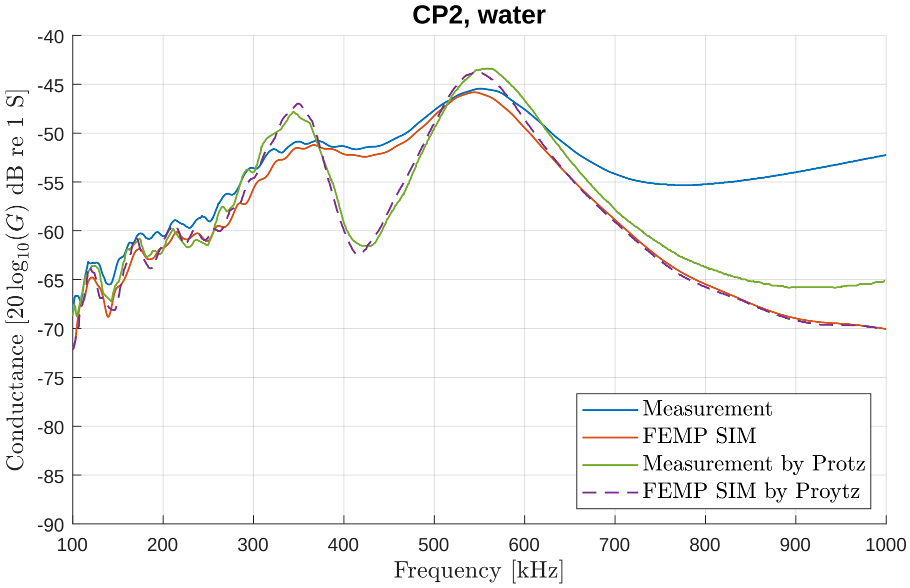

(a)

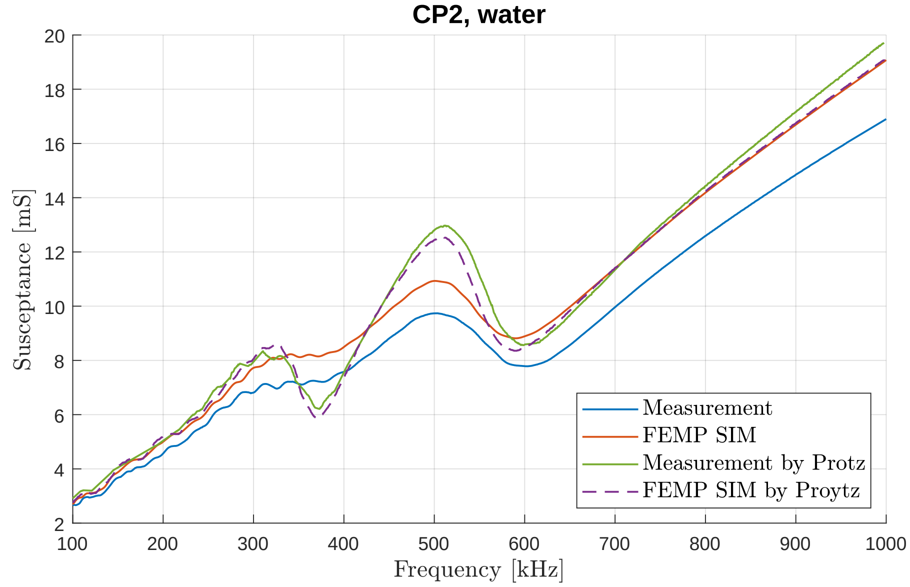

(b)

Figure 5.6: Electrical admittance for transducer CP2 in water. Comparison of measurements and FEMP simulations by this author and Prøytz [23]. (a) Conductance. (b) Susceptance.

Generally, the electrical admittance measurements in air display a better agreement compared to simulations and other measurements than the measurements in water, especially in the upper-frequency region where the deviation increases for increasing frequency.

The measurements of the conductance of MA, Figs. 5.1a and 5.2a, display a fair agreement in the frequency region below 700 kHz to the measurements and simulations conducted by Aanes [8] in 2013. Considering the substantial time between the conducted measurements, aging effects may have occurred, but due to the fair agreement, no effects are found here. In the upper region, the deviation is around 2 dB in air and 11 dB in water. Despite this, the measurements share the same curve characteristic in this region.

For CP1, the susceptance measurements in both air and water, Figs. 5.3b and 5.4b display a fair agreement with the measurements by Prøytz in the whole frequency region. The conductance measurements in Figs. 5.3a and 5.4a also have a fair agreement below the frequencies 800 kHz in air and 700 kHz in water, where a considerable deviation occurs. The deviation is around 2 dB in air and 5 dB in water. Despite the deviation in the level of conductance, the measurements share the same characteristics but at a higher level, the same as for MA.

The measurements of CP2 deviate considerably from the measurement and simulations by Prøytz[23]. Starting with the measurements in air, the conductance level in Fig. 5.5a is a bit higher below 300 kHz, more prominent between 400 and 500 kHz and highly prominent from 700 kHz and higher. At the 350 and 550 kHz peaks, there is a fair agreement between the measurements and the measurement and simulation by Prøytz [23] for a short frequency range. The susceptance measurement in Fig. 5.5b exhibits the same behavior but at a susceptance level below, where the peaks at 320 and 510 kHz have a deviation of 3 and 6 dB, respectively. Despite the deviation, the measurements follow the same curvature characteristic as the measurements by Prøytz at a different level. In water, the measurements and simulations in Figs. 5.6a-5.6b by this author have a fair agreement in the conductance up to 700 kHz and in the susceptance, they follow the same curvature at an increasing deviating level. However, compared to the measurement and simulation by Prøytz [23], a conspicuous deviation is displayed in the frequency range around 300-600 kHz where additional measurements yielded the same deviation. This author has no explanation for this.

The global maximum for the conductance measurements in water, Figs 5.2a, 5.4a and 5.6a, is at 575 kHz for MA, 587 kHz for CP1 and 550 kHz for CP2, which are noted for later discussion.

Regarding the deviation at the upper frequencies, this may be a contribution from the long wires used in the measurements, although an inspection of the measurements given by Prøytz [23] and Fig. 4.8 in [23] indicates that cables of similar lengths were used by Prøytz as well where such strong deviation did not appear at the upper frequencies. Additionally, the duct tape used for measuring the admittance in water may affect the measurements, which could contribute to the bigger deviation displayed by the measurements in water compared to air.

5.2 Source sensitivity

Results for the sensitivity measurements for MA are shown in Fig. 5.7, where it is compared to measurements and simulations by Aanes [8]. Figs. 5.8 and 5.9 show the sensitivity measurements for CP1 and CP2, respectively, where they are compared to FEMP simulations by this author, and measurements and FEMP simulations by Prøytz [23]. The simulations of CP1 and CP2 by Prøytz [23] lie approximately over the simulations by this author showing their proximity.

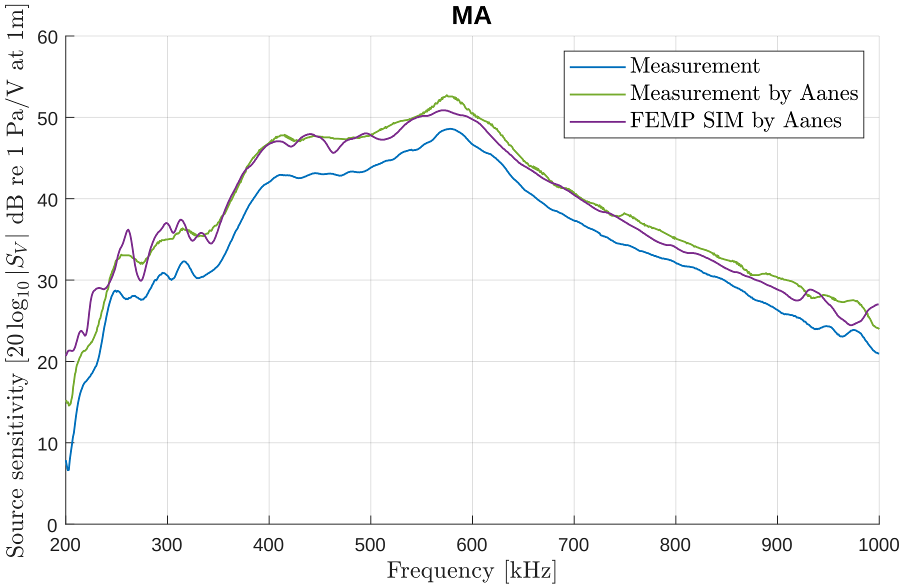

Figure 5.7: Source sensitivity for transducer MA showing comparison between FEMP simulations by this author and Aanes [8].

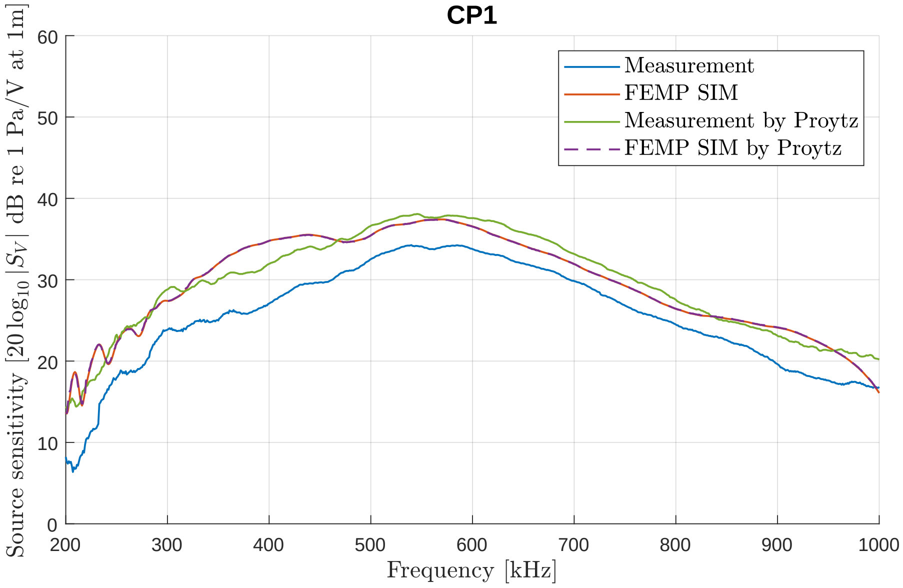

Figure 5.8: Source sensitivity for transducer CP1 showing comparison between FEMP simulations by this author and Prøytz [23]. The FEMP simulation by Prøytz lays approximately over the FEMP simulation by this author showing their close proximity.

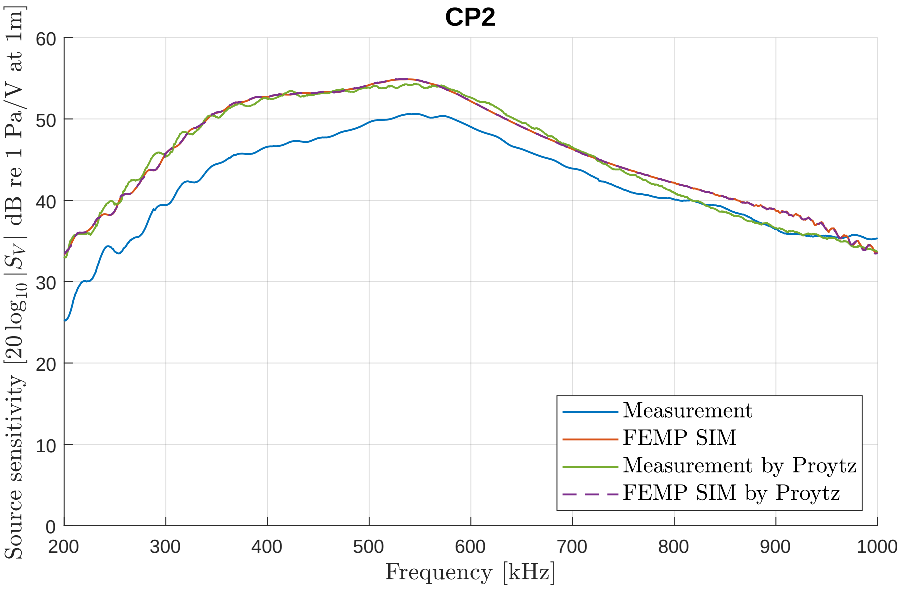

Figure 5.9: Source sensitivity for transducer CP2 showing comparison between FEMP simulations by this author and Prøytz [23]. The FEMP simulation by Prøytz lays approximately over the FEMP simulation by this author showing their close proximity.

Measurements of all the transducers in Fig. 5.7-5.9 display the same curvature characteristic as the simulations and measurements of the others at an approximately lower sensitivity level of 4 dB, except for CP2 in Fig. 5.9, where the deviation decreases around 700 kHz and a fair agreement is displayed from 800-1000 kHz. This is attributed to the use of hydrophone SN 1848. As aforementioned in Chap. 3.5, the hydrophone SN 1848, which was calibrated together with another preamplifier and DC coupler not used in this thesis while using the calibration data for hydrophone SN 1820.

The sensitivity of MA in Fig. 5.7 is highest at 400-620 kHz, with the highest level of sensitivity at 575 kHz. The sensitivity of CP1 and CP2 displays a more even sensitivity and gentler slope throughout the frequency range. CP1 in Fig. 5.8 is most sensitive at 450-700 kHz and has two close hills of approximately the same maximum at 540 and 585 kHz, while CP2 in Fig. 5.9 is most sensitive at 350-650 kHz and has the highest level of sensitivity at 546 kHz.

Compared to the conductance measurements in water for each transducer in Figs. 5.2a, 5.4a and 5.6a, the overall trends of increased and decreased conductance and sensitivity is the same. The highest level of sensitivity and conductance is the same for MA, both at 575 kHz, while for CP1, there is a deviation of 2 kHz, and for CP2, the deviation is 4 kHz relative to the second hill in the sensitivity measurements.

Looking at the similarities between the conductance in water and the sensitivity for CP2, the measurements and simulations conducted by this author of the conductance in water seem more likely to be correct.

5.3 Beam pattern

The beam pattern measurements for MA are shown in Figs. 5.10 and 5.11 where it is compared to measurements and FEMP simulations by Aanes [8], respectively. Figs. 5.12 and 5.13 shows the beam pattern measurements compared to FEMP simulations by this author. Prøytz measured the beam pattern of CP1 and CP1 transducers at 575 kHz within a smaller angular range. However, it was revealed in Chap. 3.5 that these were performed using an incorrect holder for the transducers making these measurements not directly comparable to the findings presented in this thesis.

When examining the electrical conductance in water and sensitivity, it becomes evident that the transducers perform more effectively in the middle-frequency range. There is a notable higher level in the middle-frequency region, compared to the lower and upper frequencies. As for CP1 in Fig. 5.4a, both the conductance and the sensitivity exhibit a considerably lower level, 13-19 dB less than MA and CP2, which are displayed in Figs. 5.2a and 5.6a. This is reflected in the beam patterns, where most of the beam patterns of CP1 and the lower and upper frequencies of MA and CP2 display more fluctuations beyond the main lobe, probably due to a poorer signal-to-noise ratio in these measurements.

The beam pattern measurements of MA, Fig. 5.10, compared to the measurements by Aanes [8], has a fair agreement beyond the second main lobe at most frequencies. Beyond 25° for beam patterns at 630, 760 and 850 kHz, the measurements display considerable fluctuations and deviations from the measurements by Aanes [8]. As the rotation of the transducer around its axis was compared to measurements conducted at every 45°, the chosen rotation could deviate from the rotation used in [8]. It is also unknown whether or not he had a fixed rotation using the original set screw in the system and if he used this consistently in all measurements. Comparison of the measurements to the simulations conducted by Aanes [8], Fig. 5.11, a fair agreement is found beyond the first side lobe for most frequencies, 520, 575, 630, 760 and 850 kHz, where deviations are displayed already at the first side lobe at 420 and 1000 kHz.

The beam pattern measurements of CP1, Fig. 5.12, deviate beyond the main lobe at all frequencies measured and has, in general, a higher directivity level at the main lobe relative to the side lobes compared to simulations for all frequencies but 370 kHz. This is especially prominent at 760, 850 and 1000 kHz, where at 370 kHz, the side lobes display a higher directivity level relative to the main lobe compared to simulations. For 1000 kHz, the main lobe displays a small dip at the center of the main lobe, which is not present in the measurements.

For CP2, the beam pattern measurements in Fig. 5.13 have a fair agreement with the simulations beyond several side lobes at certain frequencies. Frequencies 760, 850 and 1000 kHz have a fair agreement beyond the fourth side lobe, albeit for the measurement at 1000 kHz, the level of the side lobes is significantly lower relative to the main lobe compared to simulations. A fair agreement is found beyond the second side lobe at 520 and 630 kHz and beyond the first side lobe at 370, 420 and 575 kHz.

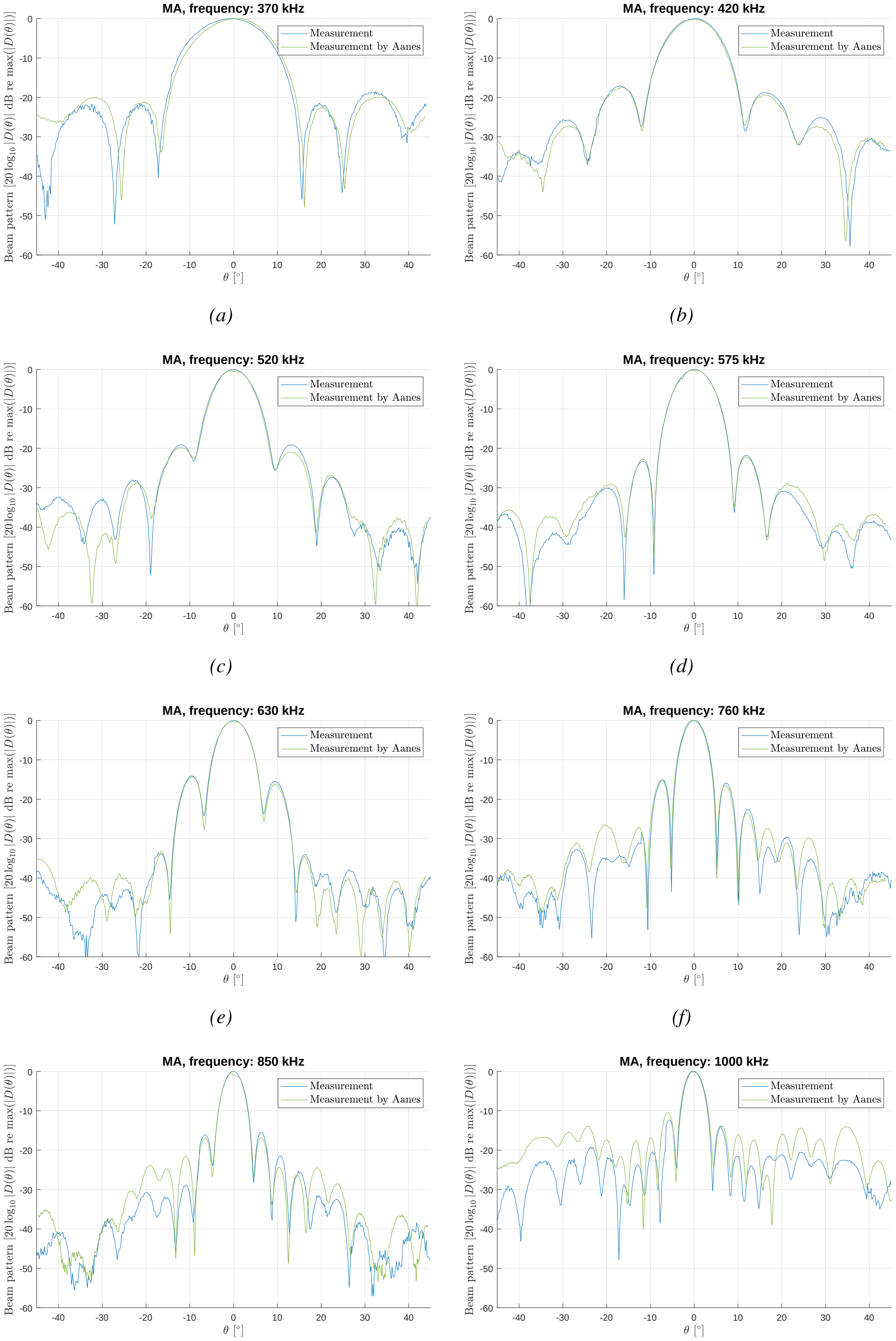

(a) *(b)* *(c)* *(d)* *(e)* *(f)* *(g)* *(h)*

Figure 5.10: Beam patterns for transducer MA at frequencies 370, 420, 520, 575, 630, 760, 850 and 1000 kHz in (a)-(h), respectively. Comparison between FEMP simulations by this author and measurements by Aanes [8].

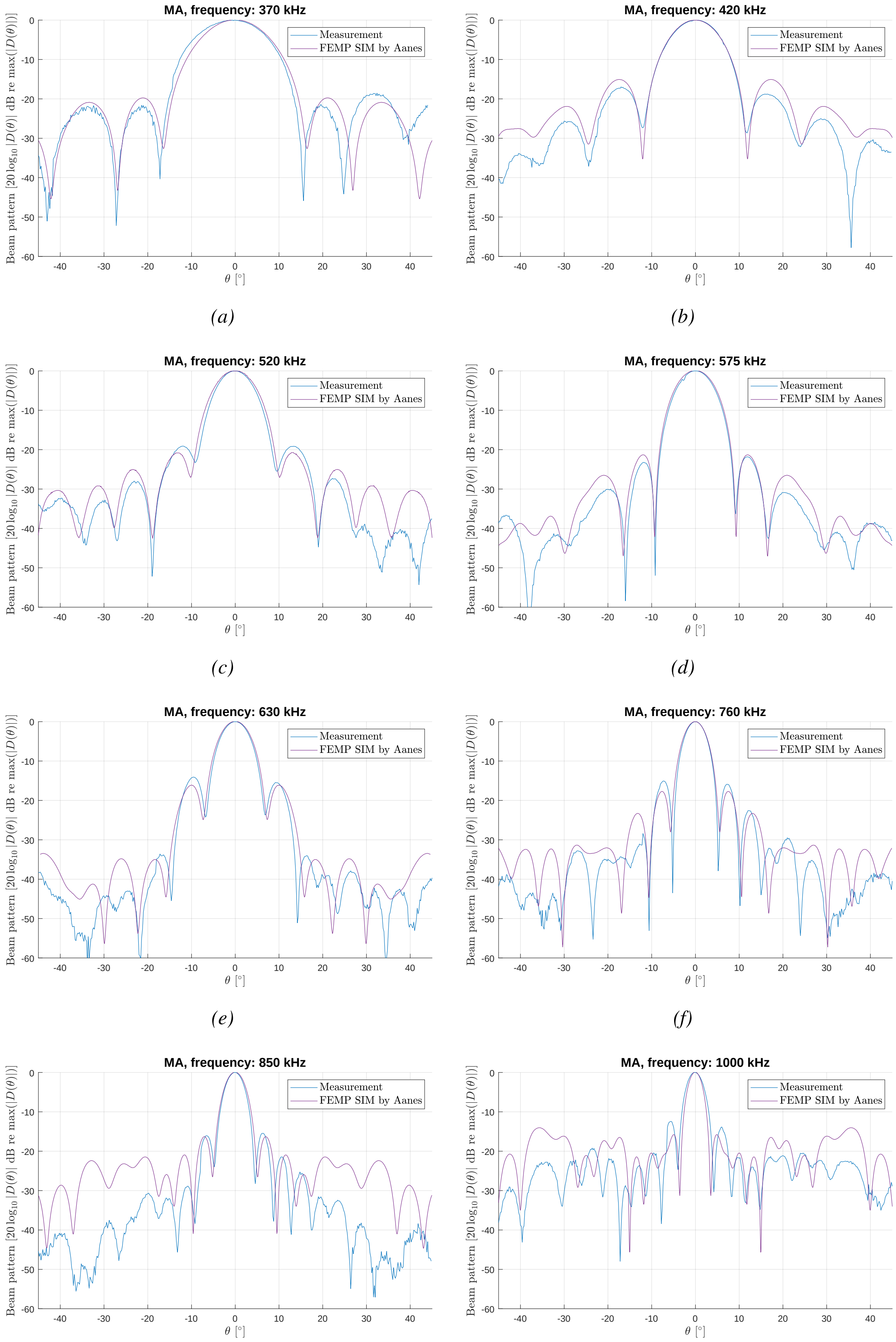

(a) *(b)* *(c)* *(d)* *(e)* *(f)* *(g)* *(h)*

Figure 5.11: Beam patterns for transducer MA at frequencies 370, 420, 520, 575, 630, 760, 850 and 1000 kHz in (a)-(h), respectively. Comparison between FEMP simulations by this author and Aanes [8].

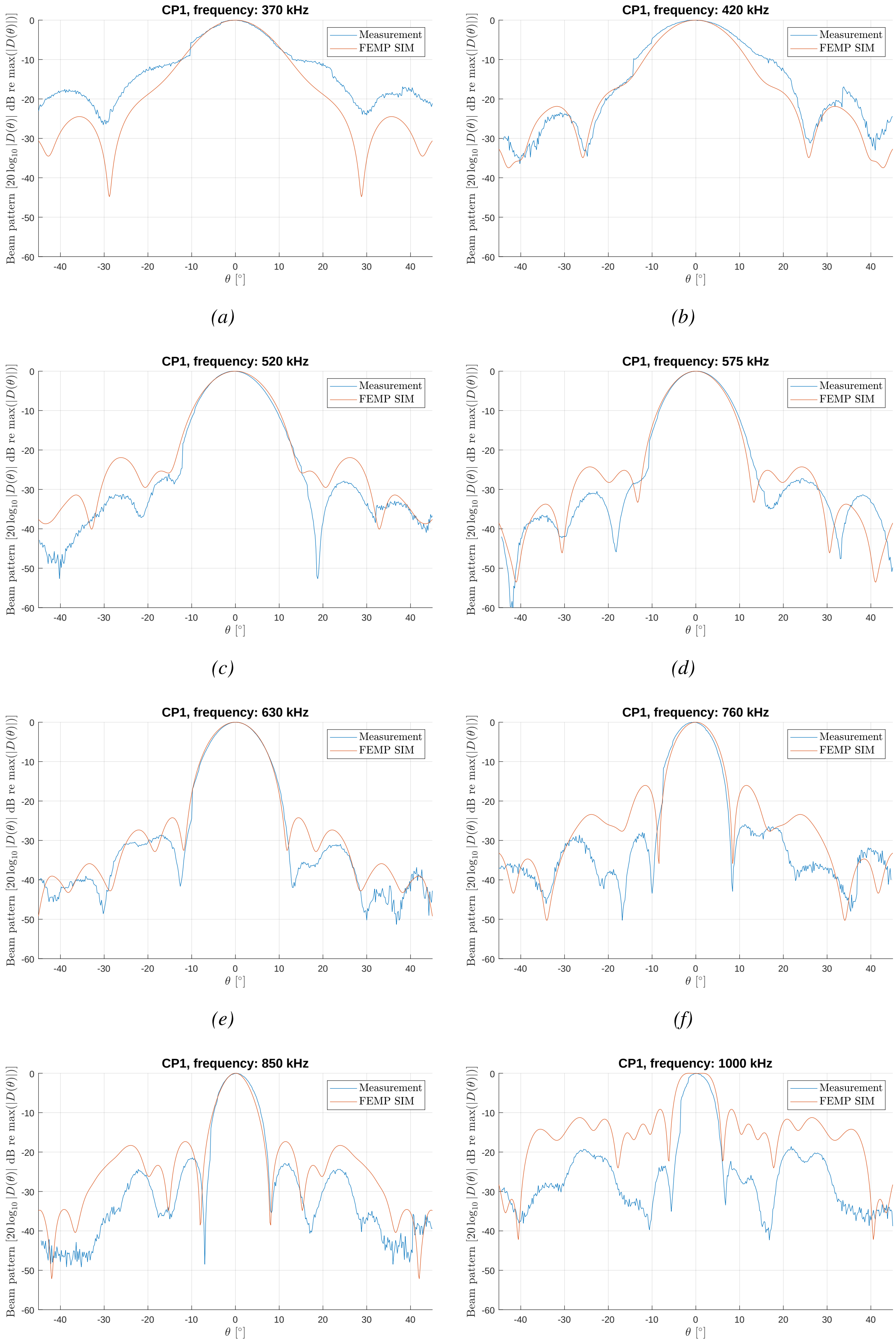

(a) (b) (c) (d) (e) (f) (g) (h)

Figure 5.12: Beam patterns for transducer CP1 at frequencies 370, 420, 520, 575, 630, 760, 850 and 1000 kHz in (a)-(h), respectively. Comparison between measurements and FEMP simulations.

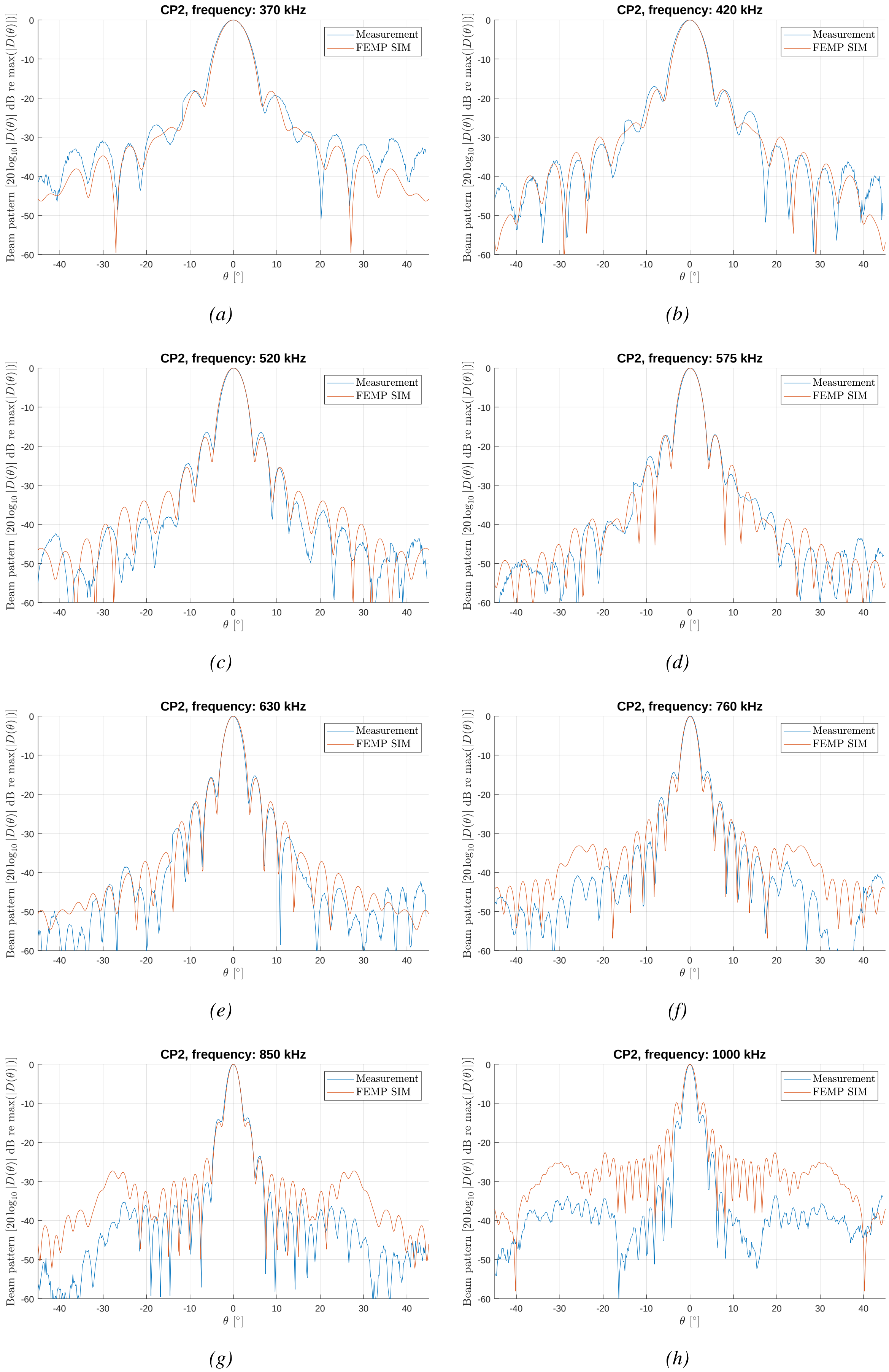

(a) *(b)* *(c)* *(d)* *(e)* *(f)* *(g)* *(h)*

Figure 5.13: Beam patterns for transducer CP2 at frequencies 370, 420, 520, 575, 630, 760, 850 and 1000 kHz in (a)-(h), respectively. Comparison between measurements and FEMP simulations.

The measurements of CP1 in Fig. 5.12 display a sudden vertical increase between two successive angles at the left side of the main lobe, where the directivity level increases most rapidly. During sensitivity measurements, it was discovered that the bandpass filter needed extra time to adjust in areas of abrupt increase in pressure. This was not implemented in directivity measurements because they were conducted before the sensitivity measurements.

The rotation of CP1 and CP2 was determined based on repeatability and no measurements were done at different rotations as it was for MA. Nevertheless, all transducer exhibits a rather symmetric behavior.

The effective radii are calculated from each beam pattern of the transducers using Eq. (2.3) as explained in Chap. 2.3.1. There are multiple reasons for choosing to calculate it from the measurements instead of simulations. This author was not able to reproduce acceptable simulations of MA, and therefore only simulations obtained from Aanes' thesis [8] are available, and the simulations of CP1 and CP2 have some aforementioned deviations and uncertainties, albeit showing a close agreement for almost all simulations. Additionally, the effective radii are used to identify the best corresponding piston model in simulations of beam transmission. The simulations are compared to beam transmission measurements using the same experimental setup as for all the previous acoustic measurements, with the exception of different hydrophones, which are thoroughly investigated. The effective radius found at the frequencies of the measured beam patterns is shown for all three transducers in Fig. 5.14 compared to the physical radius, $D_\mathrm{p}/2$, of their respective piezoelectric discs listed in Table 3.2.

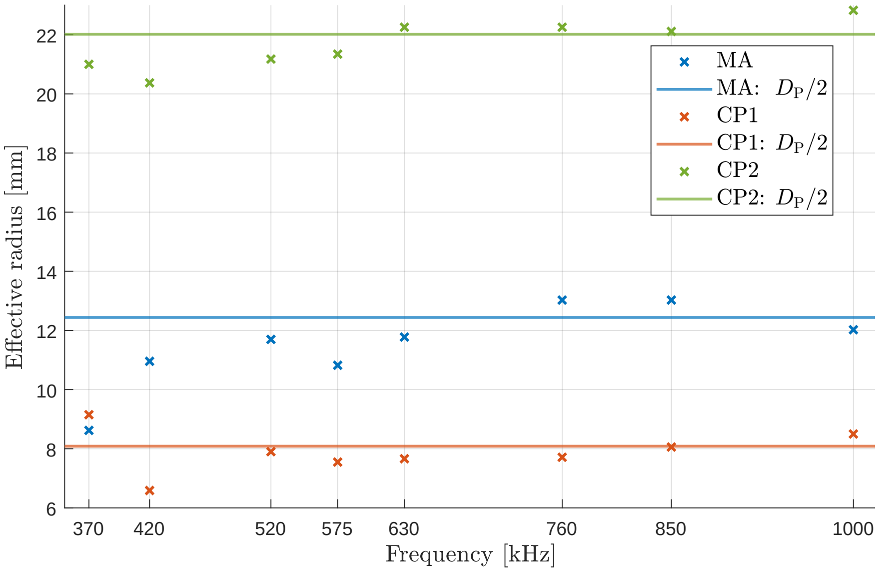

Figure 5.14: Effective radius obtained from measured beam pattern at their respective frequencies for all transducers compared to the physical radius of their piezoelectric disc, $D_p/2$, from Table 3.2.

5.4 Beam transmission

5.4.1 Measurements and simulations

The $|H_{\text{pp}}(0,z_1,f)|$ measurements compared to ASM2 simulations is presented in Fig. 5.15 together with the relevant Lamb cutoff frequencies f_{l1}^S, f_{t2}^S, f_{t3}^A and f_{l2}^A, plotted as dotted lines. *(a)* shows MA with an ASM2 simulation using the transducer's effective radius at 420 kHz, *(b)* shows CP1 with an ASM2 simulation using the transducer's effective radius at 420 kHz, *(c)* shows CP2 with an ASM2 simulation using the transducer's effective radius at 420 kHz and *(d)* shows CP2 with an ASM2 simulation using the transducer's effective radius at 575 kHz. The measurements display significant peaks around cutoff frequencies f_{l1}^S and f_{l2}^A, and the closest frequencies of obtained effective radii are at 420 kHz and 1000 kHz, respectively. ASM2 simulations were conducted using these effective radii in addition to the effective radii obtained at 575 kHz due to this being the resonance frequency of MA and in the proximity of the resonance frequency of CP1 and CP2, all displayed in Fig. 5.14. These were compared to the measurements at the mentioned cutoff frequencies to find the simulations giving the best agreement. For MA and CP1, the simulations employing the effective radii obtained at 420 kHz, $a'_{\text{eff}} = 10.96$ mm and $a'_{\text{eff}} = 6.59$ mm, respectively, exhibits the highest agreement. As for CP2, the simulations employing the effective radii obtained at 420 kHz, $a'_{\text{eff}} = 20.37$ mm, and 575 kHz, $a''_{\text{eff}} = 21.34$ mm, are both in close proximity. a'_{eff} and a''_{eff} are chosen as symbols for the effective radii obtained at 420 and 575 kHz, respectively. Notably, the simulation utilizing a'_{eff} for CP2 is closer to the measurement at the peak near f_{l2}^A and displays a more similar shape at a closer frequency to the measurement at the peak near f_{l1}^S, albeit with a bigger deviation in regards of transmission level at that peak, compared to the simulation using a''_{eff}. All these effective radii chosen are either the smallest or among the smallest effective radii calculated. Considering the idealized nature of the piston model, both results are deemed valid and therefore presented.

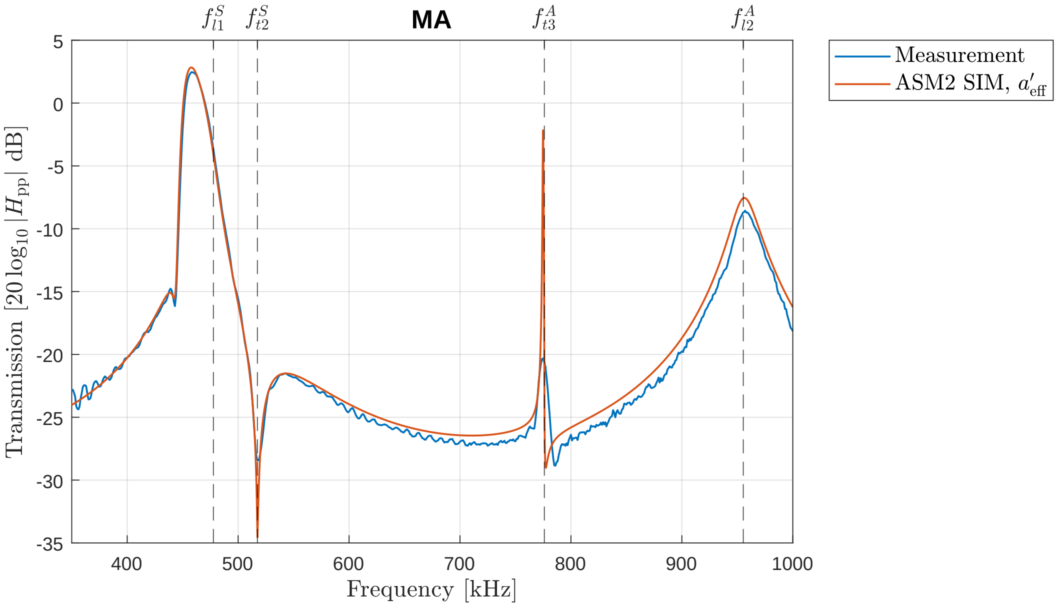
MA
f_{l1}^S
f_{t2}^S
f_{t3}^A
f_{l2}^A
Measurement
ASM2 SIM, a'_{eff}
Transmission $[20\log_{10}|H_{\text{pp}}|$ dB]
Frequency [kHz]
5
0
-5
-10
-15
-20
-25
-30
-35
400
500
600
700
800
900
1000

(a)

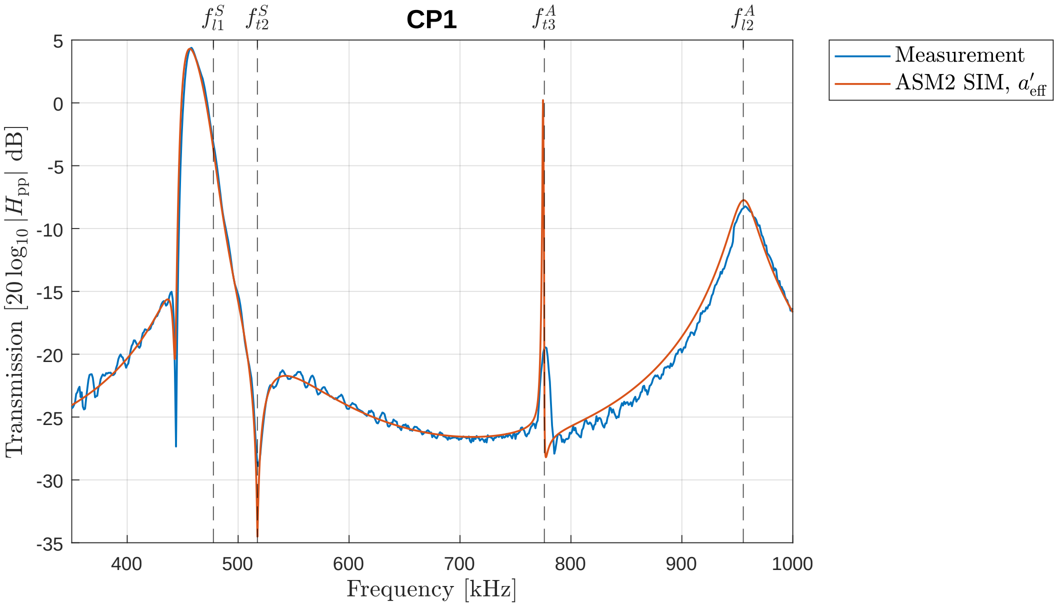
CP1
f_{l1}^S
f_{t2}^S
f_{t3}^A
f_{l2}^A
Measurement
ASM2 SIM, a'_{eff}
Transmission $[20\log_{10}|H_{\text{pp}}|$ dB]
Frequency [kHz]
5
0
-5
-10
-15
-20
-25
-30
-35
400
500
600
700
800
900
1000

(b)

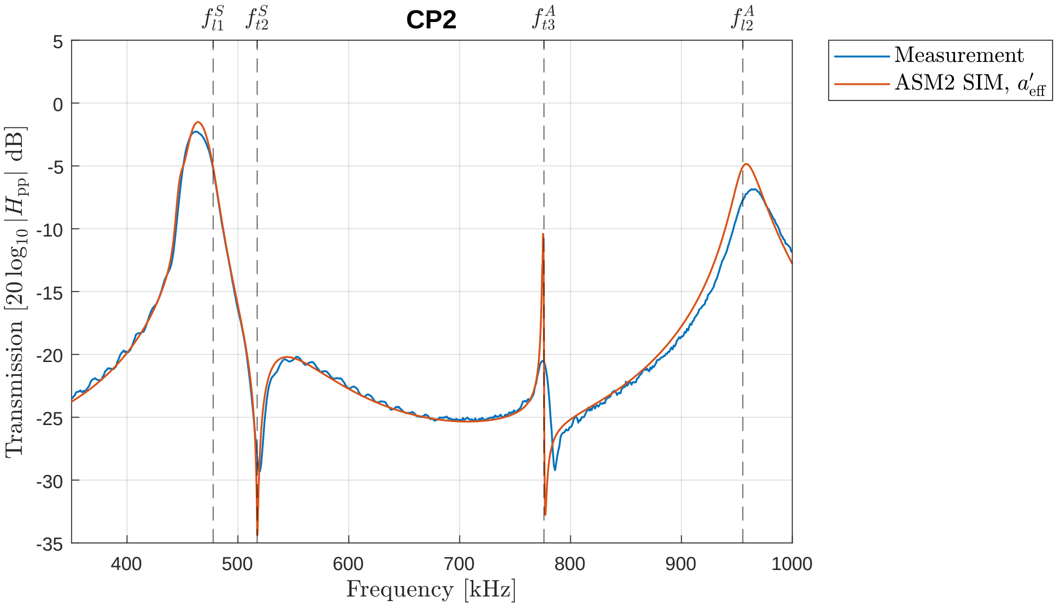

(c)

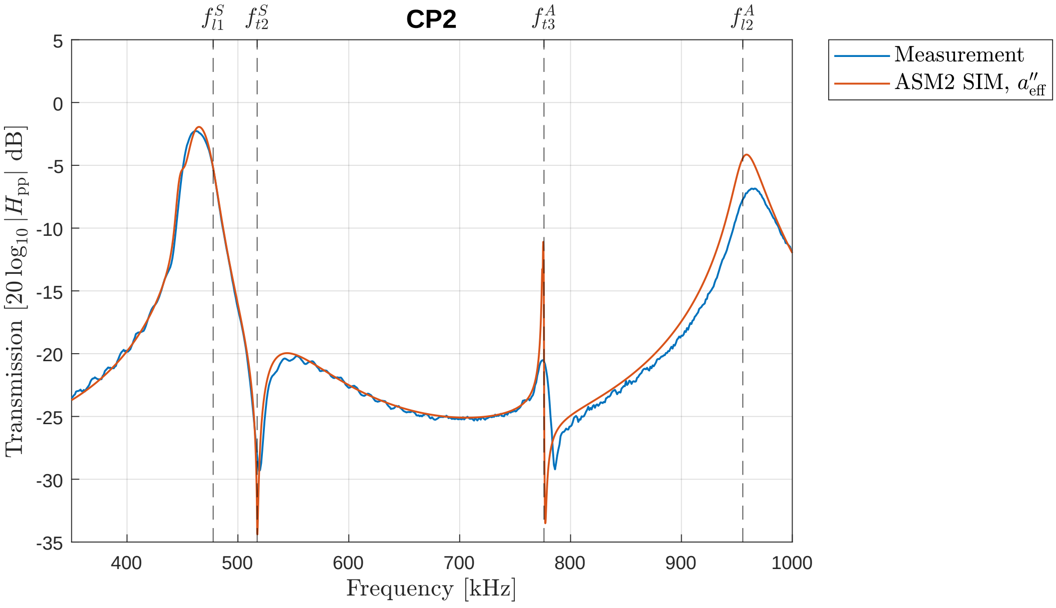

(d)

Figure 5.15: Comparison of $|H_{\text{pp}}(0,z_1,f)|$ *measurements and ASM2 simulations. The vertical dotted lines is the Lamb mode cutoff frequencies at normal beam incidence in this frequency range. (a) Transducer MA where the ASM2 simulations uses the effective radius obtained from measured beam pattern at 420 kHz,* $a'_{\mathit{eff}} = 10.96$ *mm. (b) Transducer CP1 where the ASM2 simulations uses the effective radius obtained from measured beam pattern at 420 kHz,* $a'_{\mathit{eff}} = 6.59$ *mm. (c) Transducer CP2 where ASM2 simulations uses the effective radius obtained from measured beam pattern at 420 kHz,* $a'_{\mathit{eff}} = 20.37$ *mm. (d) Transducer CP2 where ASM2 simulations uses the effective radius obtained from measured beam pattern at 520 kHz,* $a''_{\mathit{eff}} = 21.34$ *mm.*

The simulations and measurements show a fair quantitative agreement. The choice of the radius of the piston representing each transducer was limited to beam pattern measurements conducted at 8 frequencies. It is hard to say which requirements to set in order to achieve the most realist piston model, but due to the interesting phenomena happening around f_{l1}^S, this was an obvious choice of comparison in this thesis in addition to the other strong maximum associated with f_{l2}^A displayed in the measurements. Still, the closest frequencies of measured beam patterns available around f_{l1}^S were at 420 and 520 kHz.

Fig. 5.16 shows comparison of the $|H_{\text{pp}}(0, z_1, f)|$ where *(a)* compares the measurements to each other and *(b)* compares the simulations to each other. The measurements display prominent fluctuations in three regions, from the start and up to around 420 kHz, between 540-760 kHz and between 800-900 kHz, which all occur at transmission levels below -18 dB. This can possibly be caused by a lower signal-to-noise ratio, as it does no fluctuations are displayed in the simulations.

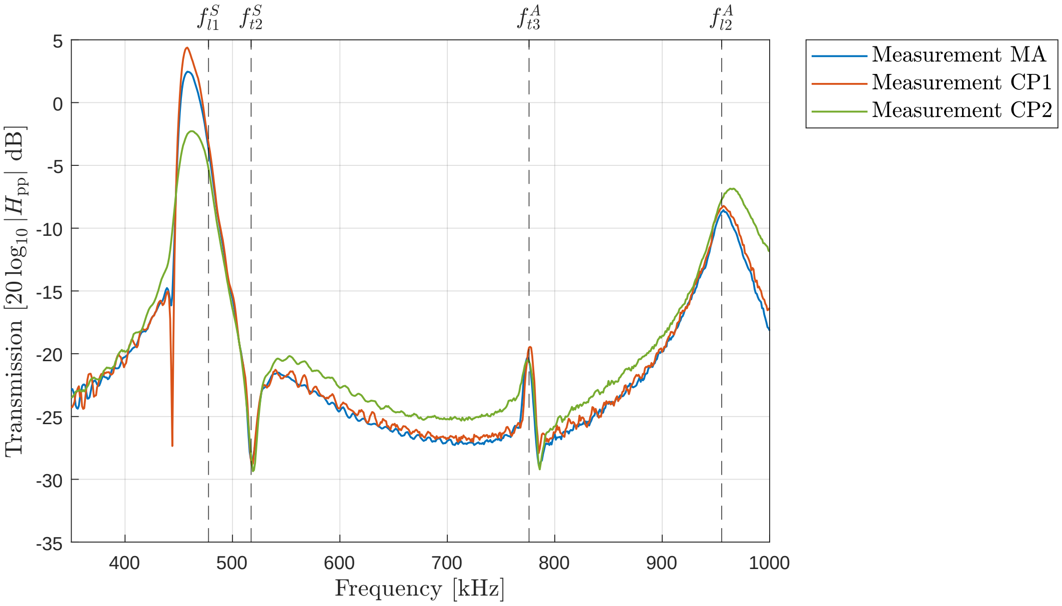

(a)

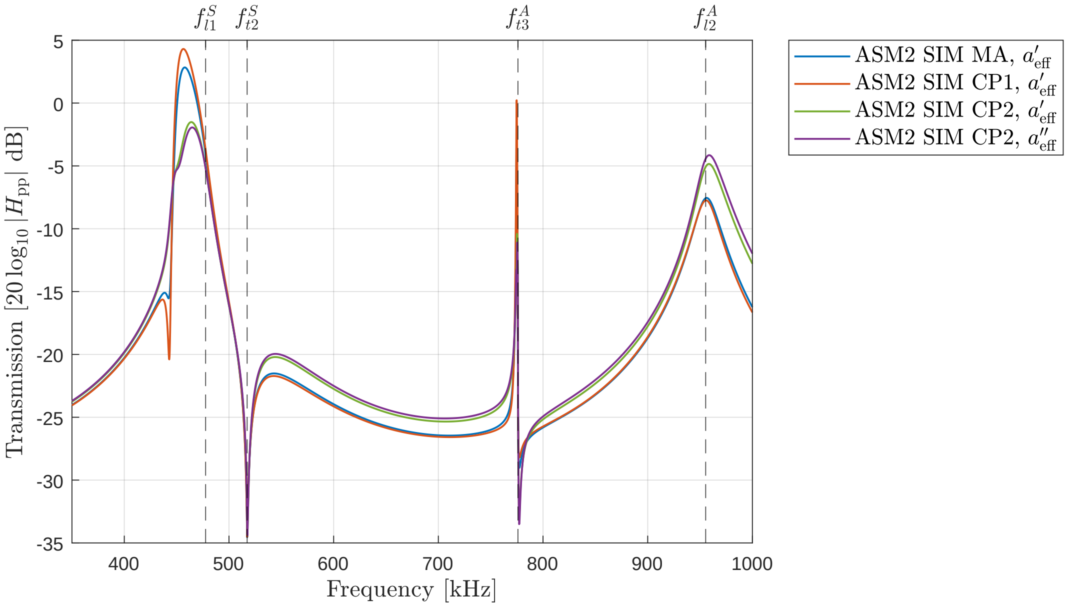

(b)

Figure 5.16: $|H_{\text{pp}}(0,z_1,f)|$ measurements and ASM2 simulations for transducers MA, CP1 and CP2, where the vertical dotted lines is the Lamb mode cutoff frequencies at normal beam incident in this frequency range. (a) Comparison between measurements. (b) Comparison between ASM2 simulations.

Aanes [8] simulated $|H_{\text{pp}}(0,z_1,f)|$ of MA at frequency 575 kHz and calculated an effective radius of 10.55 mm by Eq. (4.7) in [8] from the -3 dB angle. This radius is used to represent MA in Midtbø [17] as well, which is also presented in [1]. Simulations using this effective radius were conducted and compared to the simulations and measurements of MA by this author to see if this would yield a closer agreement. The simulation using $a'_{\text{eff}} = 10.96$ mm was 0.16 dB closer to the measurement at the maximum associated with TE1 and 0.03 dB further away from the measurement at the maximum associated with TE2 than the simulation using $a = 10.55$ mm. Given that TE1 is emphasized the most due to the interesting amplifying phenomena happening there, the simulations using a'_{eff} are still considered to yield the best agreement. Comparisons were also made between the simulations and the measurement by [17] giving the same correlations to the simulations, meaning that the simulation using a'_{eff} is considered giving the best agreement with the measurement. These comparisons are shown in Figs. C.1-C.3 in App. C.1.

The Rayleigh distance using the effective radius chosen for simulations is shown for each transducer in Fig. 5.17. The plate is at the distance of 270 mm from the source, indicated in the figure, which places it in the far-field of MA and CP1, and in the near-field of CP2. The last maximum of the near-field, defined as Ra/π [24], is indicated for both simulations of CP2 and intersects with the plate at 880 and 966 kHz for the simulations using a'_{eff} and a''_{eff}, respectively, right before and after TE2. However, no abnormalities or other effects can be identified in the small remaining frequency region in the measurements or the simulations in Fig. 5.15c. At least in the simulations, there is a small probability of the piston exhibiting an extremely dynamic sound pressure level just before the last maximum, but investigations disproved it for these simulations.

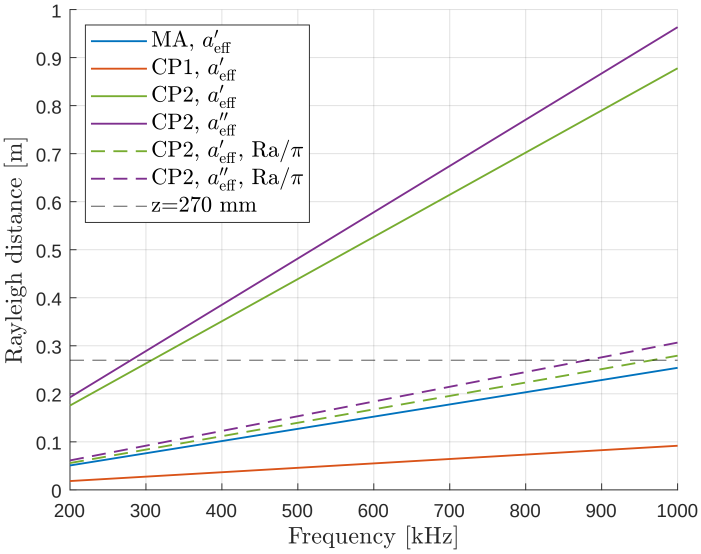

Figure 5.17: Rayleigh distance for transducers MA, CP1 and CP2, in addition to the last maximum, Ra/π, for CP2.

The biggest difference between the $|H_{\mathrm{pp}}(0,z_1,f)|$ measurements in Fig. 5.16a and $|H_{\mathrm{pp}}(0,z_1,f)|$ simulations in Fig. 5.16b is the maximum-minimum doublet associated with TS3. The simulations are really narrow and display high dynamics, while the measurements are rather damped and have wider beams relative to the simulations. In the frequency band around TS2 and TE2 the measurements also seems a bit damped relative to the simulations displaying a higher and lower transmission level, respectively. Additionally, a notch, noted as Notch 1, appears around 443 kHz and is considerably more prominent in the measurements than in simulations.

Regarding the frequency shift relative to the cutoff frequencies, all the $|H_{\mathrm{pp}}(0,z_1,f)|$ simulations and measurements for the transducers are downward frequency shifted relative to cutoff frequency f^S_{l1}, and upward frequency shifted relative to the cutoff frequencies f^S_{t2} and f^A_{l2}. As for the maximum-minimum doublet associated with cutoff frequency f^A_{t3}, the maximum and minimum are on either side of the cutoff frequency, downward and upward frequency shifted, respectively, relative to f^A_{t3}, except for the measurement of the maximum of CP1 which is upward frequency shifted relative to f^A_{t3}.

For the maximum associated with TE1, both MA and CP1 in Figs. 5.15a and 5.15b display a downward frequency shifted maximum at an apparent amplified level of transmission relative to the incidence pressure accompanied by Notch 1 below the maximum. The maximum of CP1 is at approximately 4.4 dB at 458 kHz in measurements and 4.3 dB at 464.4 kHz in simulations, and Notch 1 is at approximately -27.3 dB at 444 kHz in measurements and -20.4 dB at 443 kHz in simulations, making the notch substantially more prominent in the measurements. For MA, the maximum is at approximately 2.8 dB at 458 kHz in measurements and 2.5 dB at 457.8

kHz in simulations, and Notch 1 is at approximately -16.2 dB at 443 kHz in measurements and -15.5 dB at 442.4 kHz in simulations. The maximum for CP2 in Figs. 5.15c and 5.15d are at approximately -2.3 dB at 462 kHz in measurements and -1.5 at 464 kHz and -1.9 dB at 464.6 kHz in simulations using a'_{eff} and a''_{eff}, respectively, displaying an upward frequency shift relative to f^S_{l1} as well, without any amplifying effects relative to the incidence pressure or a notch present below. However, closer to the maximum, between Notch 1 and the maximum, the slope of both simulations displays a small dip, which is more prominent for the simulation with the biggest radius, a''_{eff} for CP2.

As for the maximum-minimum doublet in the frequency band associated with TS3, the wide beam of the measurements in Fig. 5.16a becomes wider for increasing ka-number at close transmission levels. CP1 has a maximum of approximately -19.5 dB at 777 kHz, as the only one of all measurements and simulations to be above f^A_{t3}, while both MA and CP2 have their maximum at 775 kHz, just below f^A_{t3} of transmission levels of approximately -20.3 and -20.5 dB, respectively. The minimums are approximately -27.9 dB at 785 kHz for CP1, -28.9 dB at 786 kHz for MA and -29.2 dB at 786 kHz for CP2. However, the simulations in Fig. 5.16b are narrow and exhibit high dynamics, which gets increasingly narrow with decreasing dynamics for increasing ka-number. The maximum of CP1 has a tiny amplification at the maximum relative to the incident pressure of approximately 0.2 dB at 774.8 kHz and a minimum of approximately -28.2 dB at 777.4 dB, and MA has its maximum and minimum at approximately -2.2 dB at 774.8 kHz and -29.0 dB at 777.4 kHz. The simulations of CP2 have the maxima and minima at approximately -10.4 dB at 775.2 kHz and -32.8 dB at 777.2 kHz for the one utilizing a'_{eff}, and -11.1 dB at 775.4 kHz and -33.5 dB at 777.2 kHz for the one utilizing a''_{eff}. Furthermore, the simulations for CP2 display a dip slightly below the maximum, similar to the dip reported slightly below the maximum associated with TE1, and is the most prominent for the simulation with the biggest radius, a''_{eff}. Fig. 5.18 shows the frequency band around TS3 where *(a)* shows the measurements of $|H_{\text{pp}}(0,z_1,f)|$ and *(b)* shows the simulations of $|H_{\text{pp}}(0,z_1,f)|$.

Several trends are found at the spectral maxima and minima in $|H_{\text{pp}}(0,z_1,f)|$ for increasing ka-numbers. For both measurements and simulations, the maxima associated with TE1 are upward frequency shifted and is reduced around 7 and 5 dB from CP1 to CP2, respectively, and the maxima associated with TE2 are upward frequency shifted and increases around 2 and 4 dB from CP1 to CP2, respectively. At the minima associated with TS2, the measurements are upward frequency shifted and reduced around 1 db from CP1 to CP2, while the simulations are upward frequency shifted and shows a variable transmission level of 0.1 dB. The frequency resolution appears to be a limitation here. For the maxima-minima doublet associated with TS3, the measurements are downward and upward frequency shifted, respectively, at a decreased transmission level of 1 and 11 dB, respectively and the simulations are upward and downward frequency shifted, respectively, also at a decreased transmission level of 1 and 5 dB, respectively. This entails that the lowest ka-number is closest to cutoff frequencies f^S_{t2}

and f_{l2}^{A} for measurements and simulations, and f_{t3}^{A} for measurements and that the highest ka-number is closest to the cutoff frequency f_{l1}^{S} for measurements and simulations, and f_{t3}^{A} for simulations.

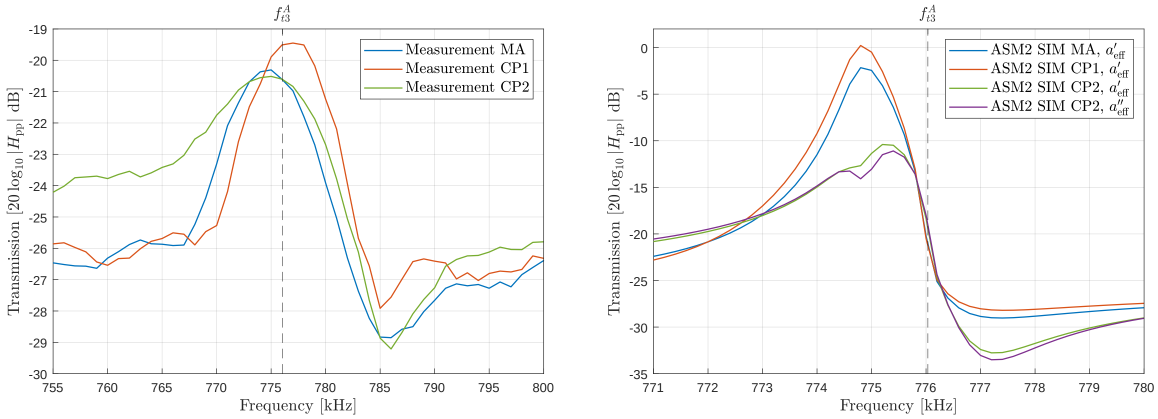

(a) *(b)*

Figure 5.18: Zoomed-in versions of Fig. 5.16 at the frequency band associated with the Lamb mode cutoff frequency f_{t3}^{A} indicated by a vertical dotted line. (a) Comparison between measurements of $|H_{\text{pp}}(0,z_1,f)|$. (b) Comparison between ASM2 simulations of $|H_{\text{pp}}(0,z_1,f)|$

Since the simulation study includes a broader range of ka-numbers both below and above those of the transducers, all trends but one will be further investigated and discussed there. The exception is the beam widening observed in the measurements in the frequency band associated with TS3.

5.4.2 Further simulation study

The ka-numbers of the transducers MA, CP1 and CP2 are calculated by the physical radius of their respective piezoelectric discs and the frequency 500 kHz, while the radii utilized in the ASM2 simulations when representing the transducers by the piston model are a'_{eff} and a''_{eff}. To distinguish between the ka-numbers representing the simulations of the transducers and the simulations in the extended simulation study, where the radius is calculated directly from the ka-number using the same frequency, 500 kHz, the ka-numbers for the transducers will attain a similar notation with primes as the effective radii. 26' is equal to $\text{ka}'_{\text{eff}} = 26$, which applies to the simulation of MA, 17' is equal to $\text{ka}'_{\text{eff}} = 17$, which applies to the simulation of CP1, and 46' is equal to $\text{ka}'_{\text{eff}} = 46$ and 46" is equal to $\text{ka}''_{\text{eff}} = 46$ which applies to the simulations of CP2.

First, additional simulations of ka-numbers 1, 3, 5, 10, 60, 100 and 120 was conducted. $|H_{\text{pp}}(0,z_1,f)|$ of ka-numbers 1, 10, 26', 46', 60, 100, 120, is presented in Fig. 5.19 and was chosen as to not overcrowd the figure but give an indication regarding tendencies for increasing ka-numbers.

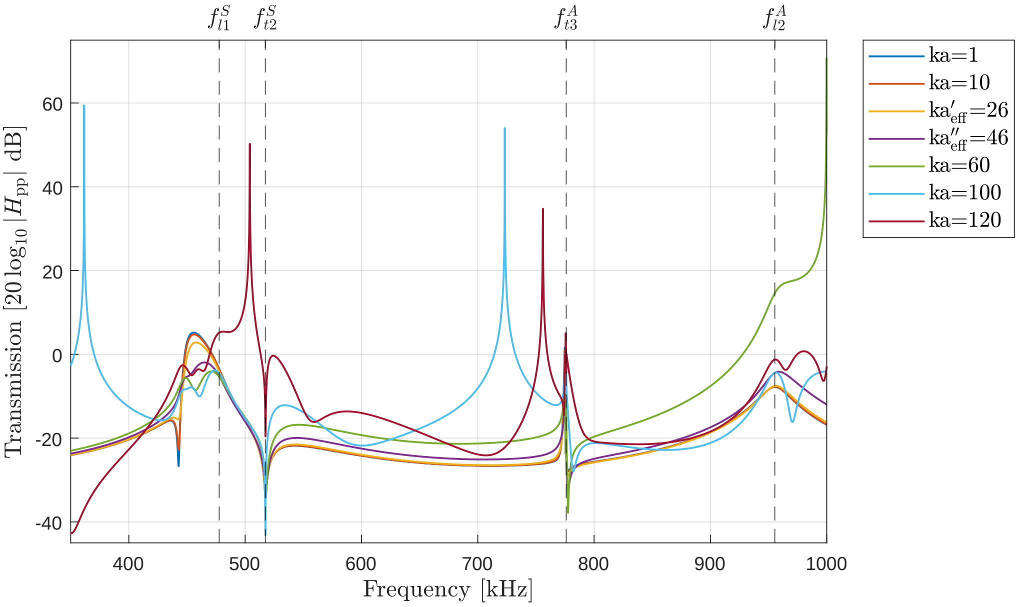

Figure 5.19: ASM2 simulations of beam transmission for a selection of ka-numbers. The vertical dotted lines is the Lamb mode cutoff frequencies at normal beam incidence in this frequency range.

Ka-numbers 60, 100 and 120 stand out with enormously high levels of transmission at some frequencies. These were further investigated while also looking at the pressure obtained at the two positions separately. This is shown in Fig. 5.20 where *(a)* is the $|H_{\text{pp}}(0, z_1, f)|$ simulation, *(b)* is the is the incident pressure at z_0 and *(c)* is the transmitted pressure at z_1. It is clear that the high transmission level is connected with a low incidence pressure which does not appear in the transmitted pressure due to this being calculated in the wavenumber domain. Nevertheless, it is worth investigating the characteristics of the curves in the frequency bands that experience minimal impact from these minima. Therefore, ka-numbers 60 and 100 will be considered for further comparisons, but ka = 120 is excluded due to the dips in the incident pressure being in close proximity to all relevant cutoff frequencies.

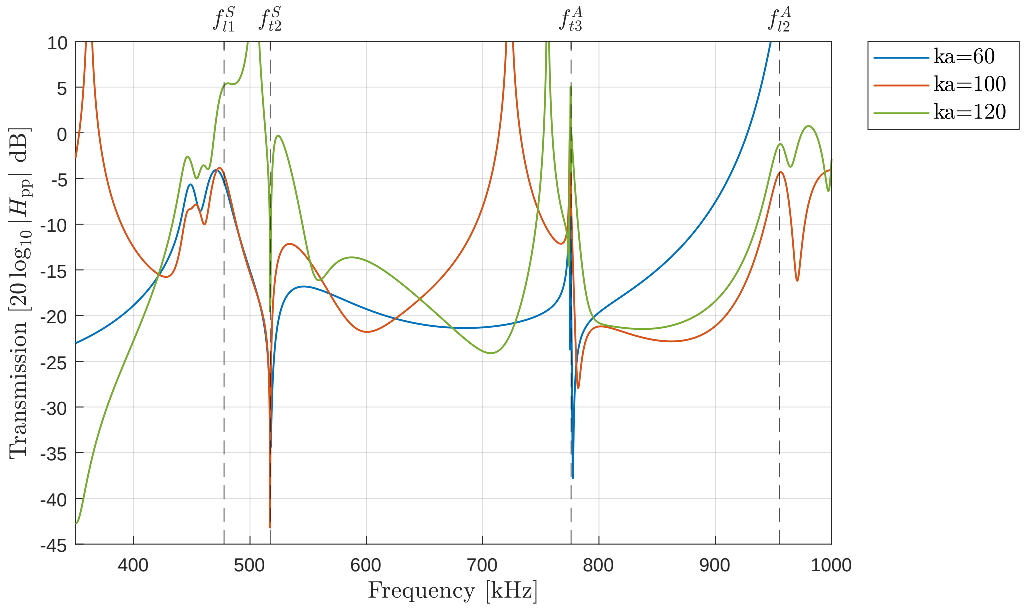
f_{l1}^S
f_{t2}^S
f_{t3}^A
f_{l2}^A
Transmission $[20\log_{10}|H_{\rm pp}|$ dB]
10
5
0
-5
-10
-15
-20
-25
-30
-35
-40
-45
400
500
600
700
800
900
1000
Frequency [kHz]
ka=60
ka=100
ka=120

(a)

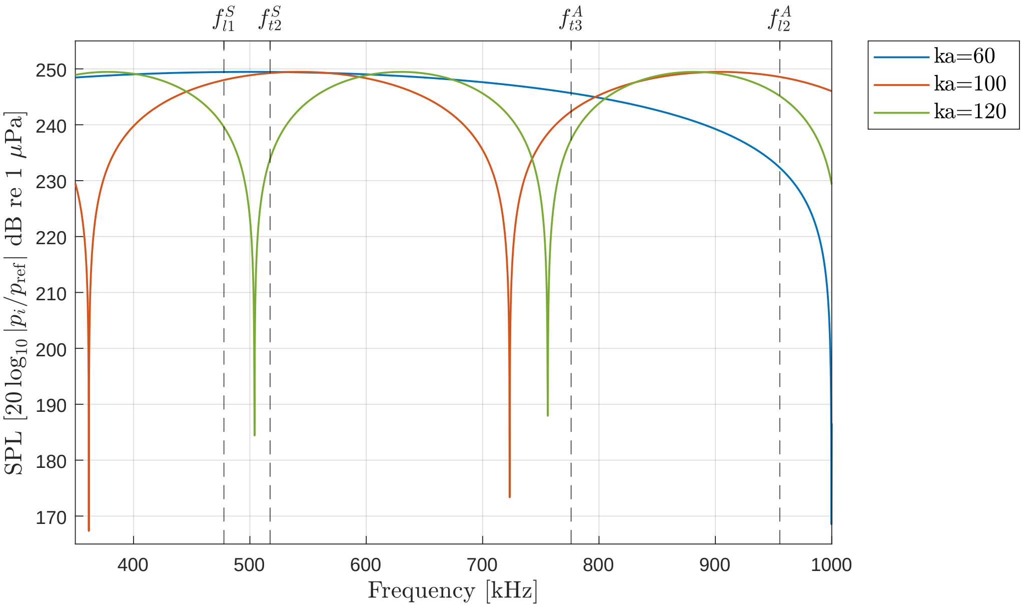
f_{l1}^S
f_{t2}^S
f_{t3}^A
f_{l2}^A
SPL $[20\log_{10}|p_i/p_{\rm ref}|$ dB re 1 μPa]
250
240
230
220
210
200
190
180
170
400
500
600
700
800
900
1000
Frequency [kHz]
ka=60
ka=100
ka=120

(b)

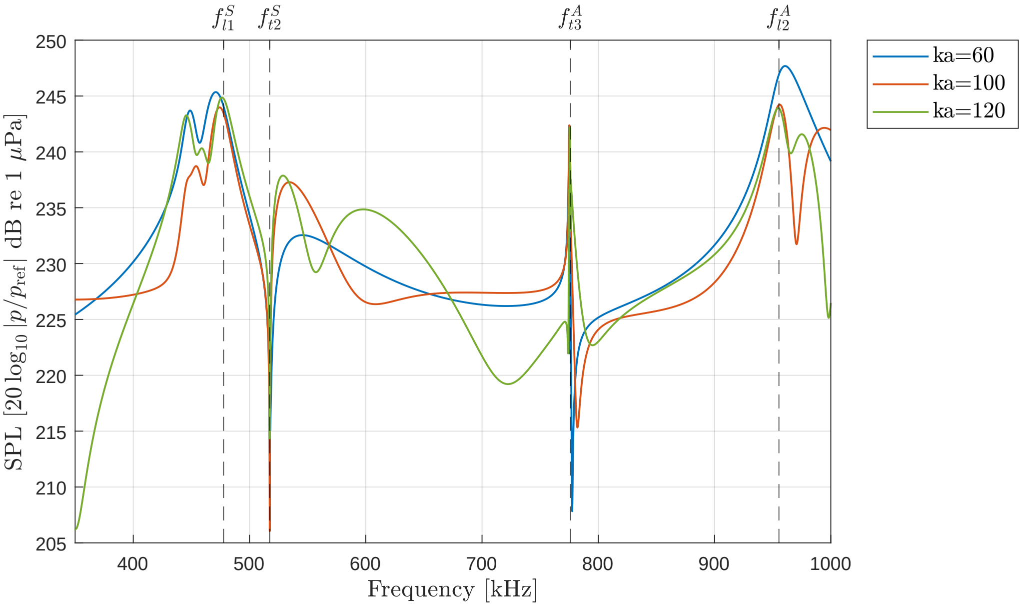

(c)

Figure 5.20: ASM2 simulations of ka-numbers 60, 100 and 120. The vertical dotted lines is the Lamb mode cutoff frequencies at normal beam incidence in this frequency range. (a) $|H_{\mathrm{pp}}(0,z_1,f)|$ *(b) Incidence pressure at* $z_0 = 270$ *mm. (c) Transmitted pressure at* $z_1 = 376.05$ *mm.*

Fig 5.21 shows the remaining ka-numbers simulated this far, ka = 1, 3, 5, 10, 17', 26', 46' and 46", where *(a)* shows $|H_{\mathrm{pp}}(0,z_1,f)|$ simulations, *(b)* shows the incidence pressure at z_0 displaying no dips and *(c)* shows the transmitted pressure at z_1. For these ka-numbers, Notch 1 and the maxima associated with TE1 and TE2 show a continuous upward frequency shift for increasing ka-numbers. All the minima associated with TS2 except ka-numbers 46' and 46" is at the same frequency, where the frequency resolution seems to be the limitation here. The maximum-minimum doublet associated with TS3 shows a continuous upward and downward frequency shift, respectively, for increasing ka-numbers, closing in on the cutoff frequency f_{t3}^A from both sides. Notch 1, which occurs around 443 kHz, before the maxima associated with TE1, displays the most dynamics for the lowest ka-numbers and increases in transmission level for increasing ka-numbers up until ka = 26. The higher ka-numbers do not display Notch 1, but as mentioned, a new dip occurs at a higher frequency around 451 kHz for ka = 46', which becomes more prominent and slightly upward frequency shifted for ka = 46".

A close look at ka = 1 shows fluctuations of around 0.04 dB between TS2 and TS3, while the other simulations are almost completely stable over the frequencies. A comparison between ka-numbers 1 and 3 is shown in Fig. C.4 in App. C. Additionally, it does not conform to all tendencies regarding increasing or decreasing transmission levels for increasing ka-numbers shown for the ka-numbers 3 to 46". ka = 1 conforms at Notch 1 below TE1, TE1 and TS3, but not at TS2 and TE2.

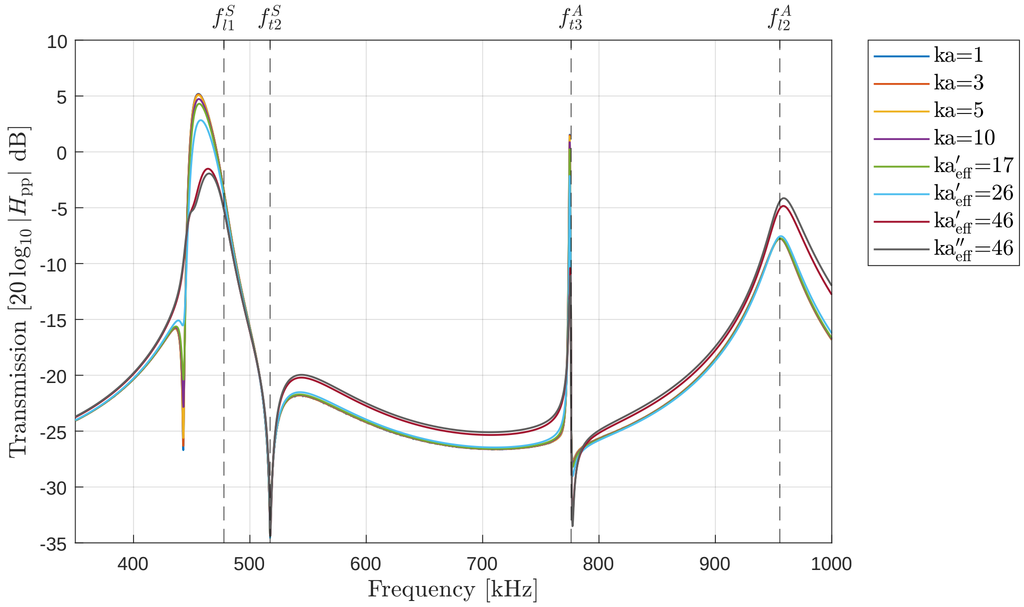
f_{l1}^S
f_{t2}^S
f_{t3}^A
f_{l2}^A
Transmission $[20\log_{10}|H_{\mathrm{pp}}|$ dB]
10
5
0
-5
-10
-15
-20
-25
-30
-35
400
500
600
700
800
900
1000
Frequency [kHz]
ka=1
ka=3
ka=5
ka=10
$\mathrm{ka}'_{\mathrm{eff}}$=17
$\mathrm{ka}'_{\mathrm{eff}}$=26
$\mathrm{ka}'_{\mathrm{eff}}$=46
$\mathrm{ka}''_{\mathrm{eff}}$=46

(a)

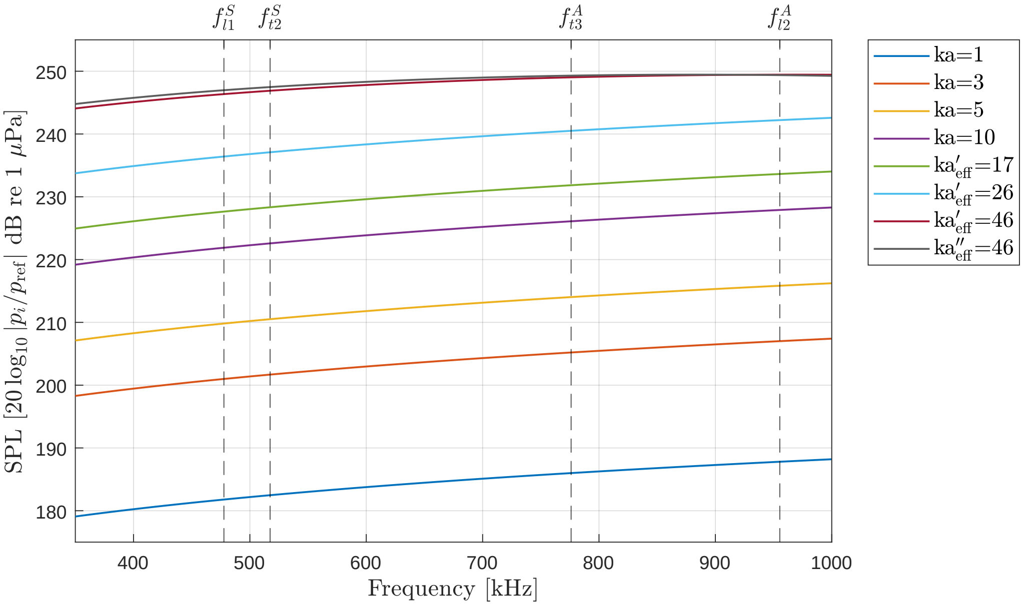
f_{l1}^S
f_{t2}^S
f_{t3}^A
f_{l2}^A
SPL $[20\log_{10}|p_i/p_{\mathrm{ref}}|$ dB re 1 μPa]
250
240
230
220
210
200
190
180
400
500
600
700
800
900
1000
Frequency [kHz]
ka=1
ka=3
ka=5
ka=10
$\mathrm{ka}'_{\mathrm{eff}}$=17
$\mathrm{ka}'_{\mathrm{eff}}$=26
$\mathrm{ka}'_{\mathrm{eff}}$=46
$\mathrm{ka}''_{\mathrm{eff}}$=46

(b)

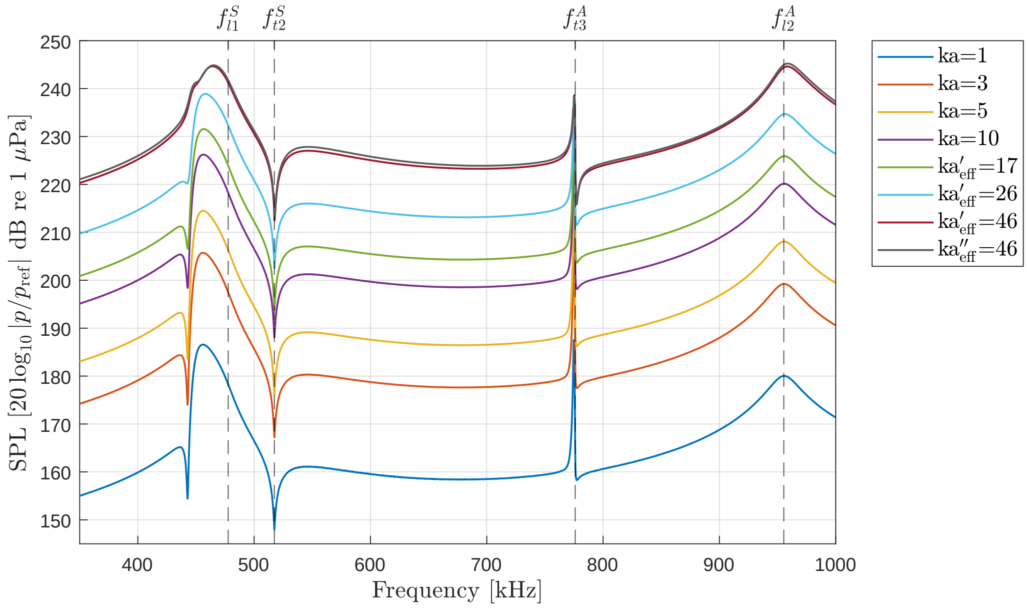

(c)

Figure 5.21: ASM2 simulations of ka-numbers 1, 3, 5, 10, 17’, 26’, 46’ and 46”. The vertical dotted lines is the Lamb mode cutoff frequencies at normal beam incidence in this frequency range. (a) $|H_{\text{pp}}(0,z_1,f)|$. (b) Incidence pressure at $z_0 = 270$ mm. (c) Transmitted pressure at $z_1 = 376.05$ mm.

The simulations were then extended to account for ka-numbers 36 and 52 to gain insight into what happens between Notch 1 disappearing and the new dip occurring between ka-numbers 26’ and 46’, and to see the evolution of the dip between ka-numbers 46” and 60.

Figure 5.22 presents simulations of the ka-numbers 3, 17’, 26’, 36, 46”, 52, 60 and 100, zoomed-in at the frequency bands associated with the cutoff frequencies. These are presented to further investigate trends over the ka-range. Simulations of ka-numbers 60 and 100 are omitted in the frequency bands where minima in the incident pressure have a strong impact, as can be seen in Fig. 5.20b. As for ka = 17, this is only included in the frequency band associated with Notch 1 and TE1, due to having highly relevant characteristics in this range but only overcrowds in the other frequency ranges. Fig. 5.22a shows the frequency band associated with the notch and the cutoff frequency f_{l1}^S, Fig. 5.22b shows the frequency band associated with cutoff frequency f_{t2}^S, Fig. 5.22c shows the frequency band associated the cutoff frequency f_{t3}^A and Fig. 5.22d shows the frequency band associated the cutoff frequency f_{l2}^A.

Starting with the frequency band associated with Notch 1 and TE1 in Fig. 5.22a, the notch is most prominent for the lowest ka-number 3, which has a level of approximately -26.3 dB at 442.8 kHz. The transmission level of the notch increases for increasing ka-numbers and is slightly downward frequency shifted before it apparently vanishes at ka = 36. Then, at ka = 46”, a dip appears around 451 kHz of approximately transmission level -5.0 dB and becomes increasingly prominent for increasing ka-numbers. For ka = 100 it ends up at an approximate level of -10.0 dB at 460.8 kHz, upward frequency shifted where an additional shelf appears around 449 kHz at an approximate level of -8.3 dB. Ka = 36 is highlighted with a thicker line to easily distinguish between the simulations displaying Notch 1 and the ones displaying the dip. The maximum is strongest for the smallest ka-numbers, starting at approximately 5.2 dB at 455.8 kHz and decreases with increasing ka-number until a level of approximately -4.1 dB at 471.0 kHz for ka = 60. For ka = 100, the maximum increases slightly to approximately -3.8 dB at 473.8 kHz, which is caused by the increase in incident pressure, displayed clearly in Fig. 5.20b.

In the frequency band associated with TS2 in Fig. 5.22b, all simulations are close to TS2 and almost all exhibits a close transmission level around -34.5 dB, except ka = 100, which has a transmission level of approximately -43.2 dB. Fig. C.5 displays a zoomed-in version of Fig. 5.22b where the limiting frequency resolution is more clearly shown. Despite the frequency resolution preventing any potential trends from being investigated, the behavior of ka = 100 having a minimum at the same frequency as ka-numbers 3, 26 and 36, can indicate that the minimum is at a constant frequency around 517.4 kHz for increasing ka-numbers at the necessary frequency resolution. Additionally, above the minimum, there is a tendency of increasing dynamics for increasing ka-numbers where ka = 100 exhibits a prominent maximum above the minimum as the only one, resulting in a minimum-maximum doublet.

For ka-numbers 3-46”, the maximum-minimum doublet associated with TS3 in Fig. 5.22c is upward and downward frequency shifted, respectively, and decreases in transmission level for increasing ka-numbers. Ka-numbers equal to and smaller than 17’ display an amplified transmission level at 774.8 kHz relative to the incidence pressure, where ka = 3 has a level of approximately 1.5 dB. A clear dip appears for ka = 46” of approximately -14.1 dB at 774.8 kHz, which evolves into a notch, noted as Notch 2, for increasing ka-numbers and is at approximately -20.8 dB at 775 kHz for ka = 100, similar to the behavior of the dip occurring for these ka-numbers nearby TE1, except Notch 2 gets a prominent depth for ka = 52 where it splits the spectral maximum into two peaks making a maximum-minimum-maximum-minimum quadruple. The lower peak becomes the strongest maximum in terms of transmission level for ka-number 52 and increases for ka = 60 in addition to being upward frequency shifted. The second peak is also upward frequency shifted and increases in transmission level from ka = 52 to ka = 60. Notably, both ka-numbers 52 and 60 exhibit a decline in the incidence pressure in this frequency band of approximately 0.05 and 0.29 dB, respectively, as opposed to the incline of 0.03-0.1 dB that the other ka-numbers exhibit, which may explain the increase of transmission level for ka = 60 relative to ka = 52.

In the frequency band associated with TE2 in Fig. 5.22d, ka = 3 has its maximum at 955.6 kHz, close to the cutoff frequency f_{l2}^{A}, and a check of ka = 1 revealed a maximum at 955.4 kHz, which is as close as possible to the cutoff frequency at the 0.2 kHz accuracy. The maximum for ka-numbers is upward frequency shifted and increases in transmission level for increasing ka-numbers up to 52. Then at ka = 100, the maximum is back at 956.4 kHz and an additional spectral minimum, noted as Notch 3, is present of approximately -16.2 dB at 970.4 kHz.

The higher ka-numbers have displayed additional characteristics than the smaller ones around the majority of the cutoff frequencies. A dip occurring around frequencies 451-460.8 kHz and Notch 2 occurring around 774.8-775 kHz, both downward frequency shifted relative to f_{l1}^S and f_{t3}^A, respectively, for ka-numbers 46'-100. For ka-number 100, an additional shelf at 449 and Notch 3 at 970 kHz, downward and upward frequency shifted relative to f_{l1}^S and f_{l2}^A, respectively, is also present.

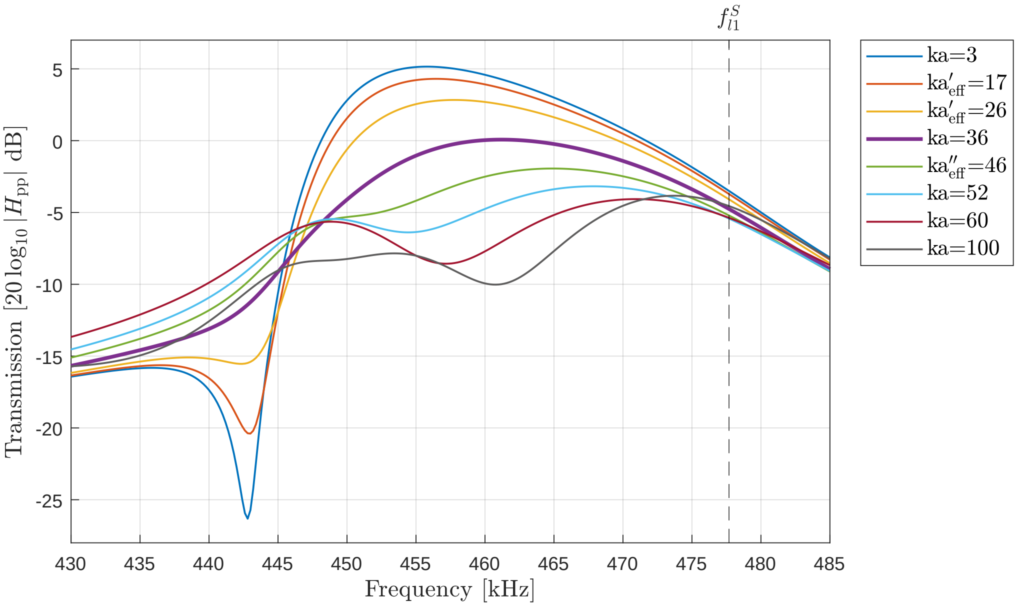

(a)

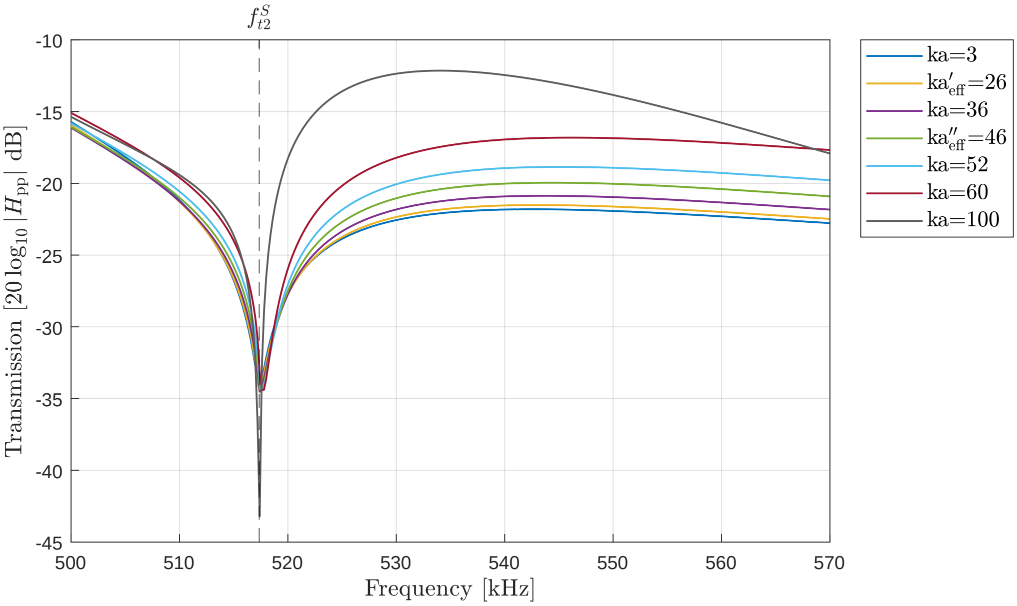

(b)

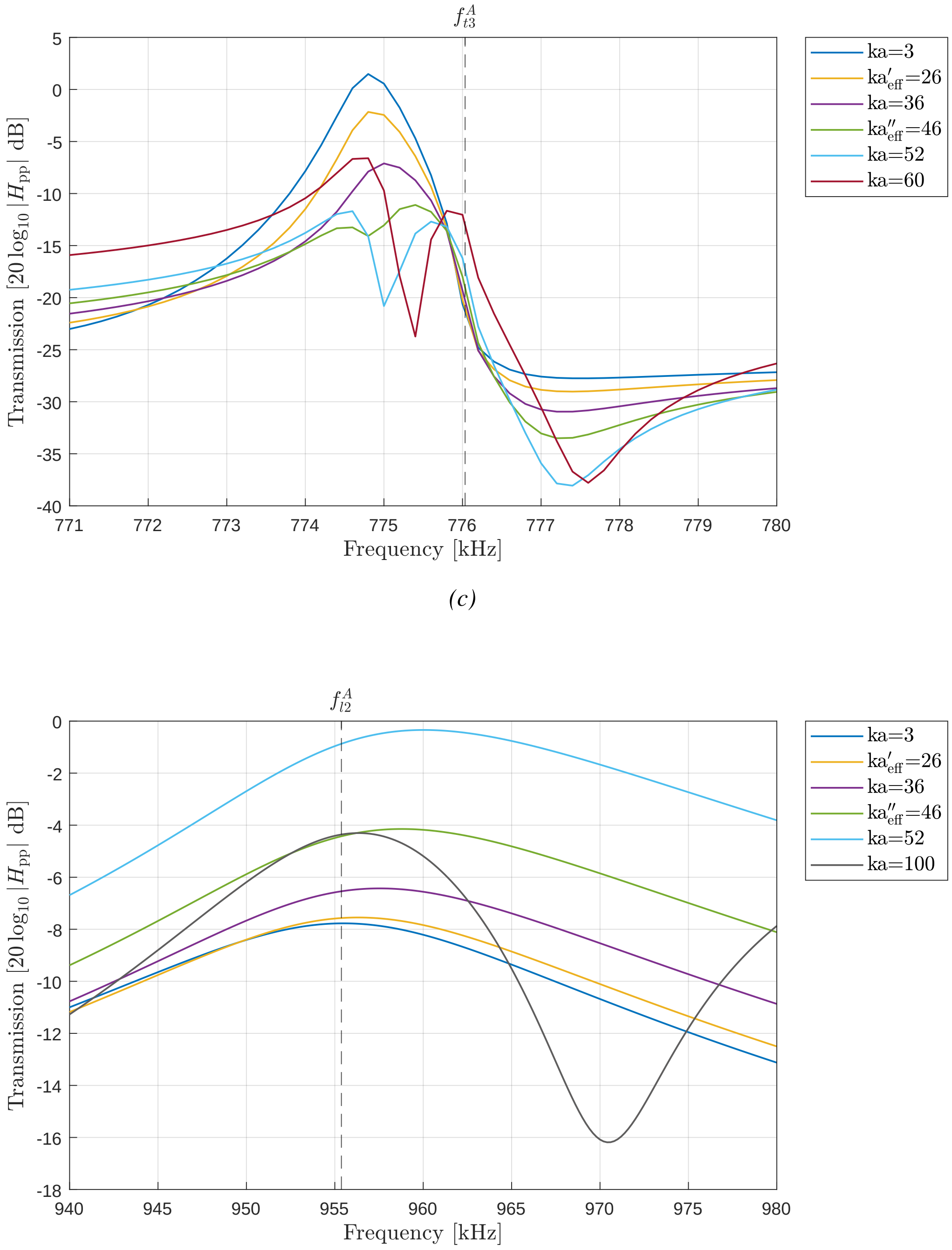

(c)

(d)

Figure 5.22: ASM2 simulations of $|H_{\text{pp}}(0,z_1,f)|$ for varies ka-numbers at frequency bands associated with the Lamb cutoff frequencies. The vertical dotted lines is the Lamb mode cutoff frequencies at normal beam incidence in this frequency range. (a) Ka-numbers 3, 17', 26', 36, 46", 52, 60 and 100 in frequency range associated with f_{l1}^{S}. (b) Ka-numbers 3, 26', 36, 46", 52, 60 and 100 in frequency range associated with f_{t2}^{S}. (c) Ka-numbers 3, 26', 36, 46", 52 and 60 in frequency range associated with f_{t3}^{A}. (d) Ka-numbers 3, 26', 36, 46", 52 and 100 in frequency range associated with f_{l2}^{A}.

5.4.3 Comparison to [1]

Sæther et al. [1] investigated $|H_{\mathrm{pp}}(0,z,f)|$ through a water-embedded steel plate as a function of distance, z, using the same setup and frequency range as in this thesis with transducer MA. They measured at distances z = 376.05, 626 and 875 mm, i.e. 100, 349.95 and 598.95 mm beneath the plate's lower surface, and conducted extensive simulations from z = 276.05 mm up to 4 m, where a direct link to this study is at the distance $z = 376.05$ mm. The maxima and minima associated with each cutoff frequency are downward and upward frequency shifted relative to the respective cutoff frequencies, equal to those remarked on in this thesis. A comparison between the results of their study and those of this thesis reveals numerous similarities in the trends of increasing ka-numbers and increasing distance from the plate, with a few exceptions. Fig. 5 in [1] shows a 3D simulation of frequency versus distance where colors indicate $|H_{\mathrm{pp}}(0,z_1,f)|$ according to transmission level. Zoomed-in version of Fig. 5 in [1], focusing on the frequency bands associated with the cutoff frequencies, is presented in Fig. 6 in [1].

Notch 1 below TE1 for ka-numbers 1-26' appears at z = 0.35-3.4 m at frequencies 440-468 kHz, particularly prominent in ranges 0.6-0.7 m and 0.9-1.5 m where it is upward frequency shifted for increasing distance in Fig. 6a in [1]. Fig. 5.22a displays that it is most prominent for ka-numbers 1 and 3 at 442.8 kHz and becomes less dynamic for increasing ka-numbers and is slightly downward frequency shifted to 442.4 kHz until it disappears for ka = 36. An additional dip, reported appearing above the notch and below f_{l1}^{S} for ka-numbers equal to and greater than 46', starts as a shelf and becomes increasingly prominent from 454.4 to 460.8 kHz, and seems to coincide with the second notch at 440-468 kHz frequency wise. In regards to transmission level, the dip is the most prominent at 460.8 kHz, which is the highest ka-number studied for this case, while in Fig. 6a in [1], the second notch is most prominent at around 457 kHz and has become less prominent at 460 kHz. Barely visible, a slight dip appears around 1.5 at 450 kHz in Fig. 6a [1], which can possibly be linked to the shelf reported for only ka = 100 at 449 kHz. As for the measurements of Notch 1, the measurements in Fig. 4 in [1] display a less dynamic minima at other distances than the simulations, while the measurements in this thesis display the opposite.

The maximum associated with TE1 in Fig. 6a in [1] shows an amplification of 5 dB relative to the incidence pressure right below the plate at 276.05 mm at 455 kHz, which is upward frequency shifted and reduced in transmission level for increasing distance [1], similar to the measurements and simulations for increasing ka-numbers, except for ka = 100, which is upward frequency shifted, but at an increased transmission relative to the prior ka-number 60, all shown in Fig. 5.22a. The highest transmission level reported in this thesis is approximately 5.2 dB for ka-numbers 1 and 3.

The minimum associated with TS2 at 517 kHz in Fig. 6b in [1] is constant at the z-range from 276.05 mm to 4 m. As previously mentioned, a limitation of frequency resolution prohibits the minimum of each ka-number from being clearly stated in Fig. 5.22b. However, considering how close they are, it is suggested that the minimum may occur at a constant minimum for all the ka-numbers. This suspicion grows stronger when compared to the constant minimum displayed for increasing distance from the plate. A maximum above the minimum is not identified in

The maximum-minimum doublet associated with TS3 in Fig. 6.c in [1] is slightly approaching f_{t3}^{A} from both sides for increasing distance. The maximum is upward frequency shifted from about 774.8 to 775.7 kHz, and the minimum is downward frequency shifted from about 777.8 to 776.2 kHz [1]. At distances around 0.75-1.25 m and 2-3 m, another spectral notch emerges at a slightly lower frequency than the maximum, at about 774-774.5 kHz. This results in a spectral triplet of minimum-maximum-minimum [1]. For increasing ka-numbers in Fig. 5.22c, Notch 2 is also appearing before the maximum but is barely present ka = 46" before it becomes increasingly prominent for increasing ka-numbers, where it splits the maximum into two peaks, resulting in a quadruple, maximum-minimum-maximum-minimum. Additionally, the first peak becomes a stronger maximum than the second peak for ka = 100. Any amplification effect, as seen for ka = 3 of approximately 1.5 dB in Fig. 5.22c, can not be identified by this author in the near-field at TS3 in [1] nor is it noted elsewhere in the article. Regarding the measurements of the maximum-minimum doublet associated with TS3, measurements in [1] and measurements in this thesis in Fig. 5.15a-5.15d exhibit significant damped behavior relative to the simulations. For increasing distance, the maximum decreases and minimum increases in transmission level, resulting in a less prominent doublet, while for increasing ka-numbers, both maximum and minimum decreases in transmission level, making the maximum less prominent and the minimum more prominent. Additionally, the measurements for ka-numbers display a slight widening of the beam for increasing ka-number, displayed in Fig. 5.18a.

As for the maximum associated with TE2, the maximum is slightly downward frequency shifted from 956.6 to 955.4 kHz for increasing distance in Fig. 6d in [1]. The opposite happens for increasing ka-numbers in Fig. 5.22d up til 52, where the maximum is slightly upward frequency shifted from approximately 955.4 to 960 kHz. The maximum of ka = 100 is downward frequency shifted relative to the prior ka-number 52, down to 956.4 kHz, and an additional notch, Notch 3, is occurring above at 970.4 kHz. This author is not able to identify any similar minima near f_{l2}^{A} in Fig. 6d in [1].

5.4.4 Overall discussion

All events identifiable in Fig. 2.5 is the plate's response to the beam. This is assumed to account for the maxima associated with TE1 and TE2, the minimum-maximum doublet associated with TS2 and the maximum-minimum doublet associated with TS3 (referring to the second peak and dip for ka-numbers 52 and higher), for measurements and simulations in this thesis and in [1]. Fig. 2.5 shows that for TS2 and TS3, only plane waves of oblique angles can excite the maximum and minimum doublets appearing, meaning that the doublets at TS2 and TS3 is caused by wave interaction inside the plate caused by the finite angular spectrum of the beam.

The observed apparent amplification phenomena found for the maximum related to TE1 have been ascribed to the finite angular spectrum interacting with the backward-wave branches of the Lamb modes S_{-2} and S_2 in the plate [1]. These are characterized by opposite signs for their phase and group velocities and demonstrate negative and positive in-plane wavenumbers, respectively [1]. Consequently, the beam is confined within the plate by carrying energy back towards the beam center resulting in a narrower transmitted beam, as opposed to interaction with forward-wave branches, where the energy is carried away from the beam center resulting in a wider transmitted beam [1].

The simulations narrow and highly dynamic behavior around TS3 is not found in the measurements at this frequency TS3, where a rather damped and widened beam is exhibited instead. The model does not account for viscoelastic loss in the plate or the water which could be significant in explaining this deviation [1]. The dynamic narrow beam is not sensitive to leaky Lamb wave loss but to viscoelastic loss, which may mean that the apparent amplification relative to the incidence pressure found for ka-numbers equal to and smaller than 17' at the maximum associated with TS3 is artificial.

As for the additional notches, dip, shelf and the extra maximum peak remarked, not identified in Fig. 2.5, these are assumed to be caused by destructive or constructive interference of the wave propagation in water [1]. The greater the distance from the plate for these additional characteristics, the stronger the suspicion that it is due to wave interaction in the water and not in the plate [1] is. The extra characteristics appearing at frequencies closely to identified events in [1] can indicate that this also applies for these in addition to the rest. However, this requires further investigations for any clarification [1].

The spectral minima in the near-field of sources of big ka-numbers at this distance restricts the investigation of whether a big ka-number such as 100 would tend towards a plane-wave transmission response of normal incidence due to the spectral minima in the sources near-field. The ka-numbers 14, 20 and 42 simulated in [19] shows an indication of the maximum associated with TE1 tending toward the cutoff frequency f_{l1}^{S} in Fig. 1 [19] for increasing ka-number and the extensive simulation displayed in Fig. 2 in [19] underlies this trend. A simpler model was used in these simulations, not accounting for near-field effects of the sources, while this is taken into account in this thesis. As mentioned in Chap. 5.4.3, the same tendency is exhibited in the frequency band associated with TE1 by the ka-numbers investigated in this thesis in Fig. 5.22a, but an additional dip evolved at higher ka-numbers and the shelf, both below the maximum, is displayed for ka = 100. The tendency nearby the other TE and TS modes investigated in this thesis is variable. The minimum above f_{t3}^{A} is suggested constant for all ka-numbers due to aforementioned reasons, and the increasing dynamics from the minimum evolving into a prominent maximum for ka = 100 also indicates a tendency of downward frequency shift for this maximum. The maximum of ka = 100 is nearest the cutoff frequency f_{t3}^{A} but with an additional maximum-minimum doublet below the maximum, while the minimum of the middle ka-numbers 36, 46’ and 46” is closest to f_{t3}^{A} where ka = 100 is tending away from f_{t3}^{A} relative to these. The maximum of the smallest ka-numbers is closest to f_{l2}^{A}, but the pattern of upward frequency shift for increasing numbers up to 52 is broken by ka = 100, which has the maximum at equal frequency as ka = 26’, with an additional notch below the maximum. This suggest that ka = 100 is not a sufficiently high ka-number at this distance to give clear tendencies whether big ka-numbers tend towards plane-wave transmission response relative to how close the plate is. Taking into account the increasing frequency of spectral minima in the near-field of increasing ka-numbers, greater distances is required to investigate this further.

Chapter 6

Conclusion and Future Work

6.1 Conclusion

In this thesis, the properties of three in-house built transducers, MA [8], CP1[23] and CP2 [23], have been measured and simulated using a finite element method. The electrical admittance in air and the electrical admittance, the source sensitivity and multiple beam pattern in water where investigated. Then, beam transmission measurements in water using these transducers were conducted, focusing on the Lamb modes S_2, A_2 and A_3. Characterizing the transducers is important to this study to understand the incident beam on the plate, which induces leaky Lamb waves in the plate. Finally, simulation by ASM2 utilizing the effective radii calculated from the measured beam patterns of the transducers was used for beam transmission simulation, compared to measurements. Simulations were then extended to account for a broader range of ka-numbers allowing for further investigations of the Lamb modes.

This author's attempt of simulating MA in the finite element method had deviations compared with [8] caused by minor differences in the material constant and/or the transducer geometry used in simulations. Whether this is due to misinterpretation by this author or some typo in [8], is unknown. The finite element simulations of CP1 and CP2 had varied results compared with prior simulations by [23], but a fair agreement was displayed for most comparisons. As for the measurements, there were some challenges with the measurement setup, but this only influenced the source sensitivity. Else, a fair agreement was exhibited for most measurements compared to simulations and prior measurements.

In beam transmission, the transfer function for a normally incident sound field is investigated. The simulated ka-numbers were 1, 3, 5, 10, 17', 26', 36, 46', 46", 52, 60, 100 and 120, where the numbers marked with primes are simulations representing the three transducers used for measurements. These ka-numbers are calculated a bit differently, resulting in a bit lower value than their respective noted integer. Ka-numbers 60, 100 and 120 exhibited some spectral minima in the incidence pressure field, making them unsuitable for comparison in the frequency bands highly affected by this, where simulations of ka = 120 were omitted entirely due to this.

There are several characteristics displayed in the transfer simulations, varying in dynamics and frequency for increasing ka-numbers. The spectral maxima and minima characteristics found for all ka-numbers investigated are the maximum associated with the lower cutoff frequency of S_2, the minimum associated with the upper cutoff frequency of S_2, the maximum-minimum doublet associated with A_2 and the maximum associated with A_3. These have been attributed to the plate's response and the minima associated with A_2 and the doublet associated with A_3 is attributed to the wave interactions in the plate caused by the finite angular spectrum of the beam.

Other characteristics are found for certain ka-numbers in this frequency range. There is a notch below the maximum associated with the lower cutoff frequency of S_2 with an additional dip above this and a shelf between the notch and the dip. Above the minimum associated with the upper cutoff frequency of S_2, there is a maximum linked to the minimum and this is therefore also attributed to wave interactions in the plate caused by the finite angular spectrum of the beam. An additional doublet below the doublet associated with A_2 results in a quadruple, and there is a notch above the maximum associated with A_3. Except for the maximum associated with the upper frequency of S_2, all the extra characteristics displayed are suggested to be caused by destructive and constructive wave interaction in the water.

Monotonic frequency shifts are found for increasing ka-numbers at most characteristics. The notch, dip and maximum associated with the lower cutoff frequency of S_2, the maximum associated with the upper cutoff frequency of S_2, in addition to the spectral maxima and lowest minimum associated with A_2 are displaying this. As for the last minimum associated with A_2, the pattern break after ka = 46', and the maximum associated with A_3, deviate for only ka = 100.

The measurements of the beam transmission compared to their respective simulations deviates in some characteristics. The notch displays greater dynamics in the measurements than in the simulations. The biggest difference between the measurements and simulations is damped and widened behavior of the doublet associated with A_2 compared to the narrow and highly dynamic behavior of the simulations. The model is not taking intrinsic losses of the plate and the water into account, which is pointed to as a possible significant factor in explaining the difference between measurements and simulations. An apparent amplified transferred pressure found for low ka-numbers in simulations is therefore classified as artificial caused by the model's calculations.

Comparison to [1] revealed several similarities and some opposite behavior for increasing ka-numbers compared to increasing distance to the plate. The measurement of MA at distance z_1 has been conducted in this thesis and by [1], giving a direct link between the studies. The notch identified below the maximum associated with the upper frequency of S_2 is therefore stated to be the same in both studies. Links between possible candidates have been suggested for some of the additional characteristics found in this thesis, but further investigations remain to gain insight into this.

Characteristics not found by this author in prior literature are the maximum below the doublet associated with A_2 for ka-numbers 52 and 60, and the notch above the maximum associated with A_3 for ka = 100.

The investigation of whether a big ka-number would tend toward plane-wave theory were inconclusive. Some tendencies indicated this slightly for ka = 100, but due to the short distance to the plate, it was suggested that it may not have been sufficiently high relative to how close the plate is. Moreover, taking into account the increasing spectral minima in the near-field of the source, it becomes clear that a greater distance is required to investigate this further.

6.2 Further work

The main things that could be improved for the benefit of later work are new sensitivity measurements using a newly certified calibrated hydrophone, investigating the deviation in the electrical admittance measurements and finding another way to conduct the electrical admittance measurement in water rather than hanging it by duct tape. Moreover, new attempts can be made to locate the files corresponding to simulations of the transducers in [8, 23]. Then the susceptance can be simulated for MA as there is no previous simulation of this, the simulation of the electrical admittance for CP1 can be clarified and the beam pattern simulations for both CP1 and CP2 in this thesis can be tested.

Furthermore, several interesting things can be further pursued regarding beam transmission. In the simulation study, simulations in the frequency band associated with the lower cutoff frequency can clarify whether the minimum is at a constant frequency. Furthermore, an extensive simulation of ka-numbers versus frequency where colors represent the level of transmission could help visualize the tendencies of increasing ka-numbers more clearly. The increasing effects of spectral minima in the incident pressure field constrain the possible range of ka-numbers to be simulated at this distance. Therefore, the proposed extensive simulations can be conducted at multiple distances as well, which would indirectly increase the range of ka-numbers investigated and give further insight into where the notches appear and why, and if any more is present not identified in this study. For this, measurements of transducers MA, CP1 and CP2 can help bring insight into this.

As for the characteristics shown most prominent for the higher ka-numbers investigated in this study, it would be interesting to measure with a bigger ka-number to see whether these effects are present in measurements as well.

A further investigation can be made by linking the beam pattern of the source together with the different phenomena happening, giving insight into the weighting of the angles of plane waves. This could perhaps give indications as to why the maximum associated with TS2 is only prominent for ka = 100 in simulations in this thesis and give insight into the other phenomena. Extending with FEMP simulations could also give more realistic simulations of real transducers and the losses in the water and plate could be included. However, this requires a thorough review of the simulations, as mentioned above.

Bibliography

[1] M. M. Sæther, P. Lunde, and S. H. Midtbø, "Interaction of three-dimensional acoustic beam with fluid-loaded solid plate: Axial near- to far-field transmission at normal beam incidence," *Ultrasonics*, vol. 125, no. 106795, September, 2022.

[2] K. D. Lohne, P. Lunde, and M. Vestrheim, "Ultrasonic signal transmission in plates - study of a steel plate immersed in water," *Proceedings of the 31th Scandinavian Symposium on Physical Acoustics, Geilo, Norway, 27-30 Jan.*, p. 23, 2008.

[3] ——, "Measurements and 3D simulations of ultrasonic directive beam transmission through a water-immersed steel plate," *Proceedings of the 34th Scandinavian Symposium on Physical Acoustics, Geilo, Norway, 29. Jan. - 2. Feb., 2011.*

[4] L. Rayleigh, "On the free vibrations of an infinite plate of homogeneous isotropic elastic matter," *London Mathematical Society*, pp. 225–234, 1889.

[5] H. Lamb, "On the flexure of an elastic plate," *London Mathematical Society*, pp. 70–91, 1889.

[6] ——, "On waves in an elastic plate," *Royal Society of London*, pp. 114–128, 1917.

[7] H. Reissner, "Der senkrechte und schräge durchtritt einer in einem flüssigen medium erzeugten ebenen dilatations welle durch eie in diesem medium befindliche planparallelle feste platte," *Helv. Phys. Acta*, vol. 11, pp. 140–155, 1938.

[8] M. Aanes, "Interaction of piezoelectric transducer excited ultrasonic pulsed beams with a fuid-embedded viscoelastic plate," Ph.D. dissertation, Dept. of Physics and Technology, University of Bergen, Norway, 2013.

[9] M. F. M. Osborne and S. D. Hart, "Transmission, reflection, and guiding of an exponential pulse by a steel plate in water. II. experiment," *The Journal of the Acoustical Society of America*, vol. 18, no. 1, pp. 170–184, 1946.

[10] R. D. Fay and O. V. Fortier, "Transmission of sound through steel plates immersed in water," *The Journal of the Acoustical Society of America*, vol. 23, no. 3, pp. 339–346, 1951.

[11] M. J. Anderson, P. R. Martin, and C. M. Fortunko, “Resonant transmission of a three-dimensional acoustic sound beam through a solid plate in air: Theory and measurement,” *The Journal of the Acoustical Society of America*, vol. 98, no. 5, pp. 2628–2638, 1995.

[12] P. Cawley and B. Hosten, “The use of large ultrasonic transducers to improve transmission coefficient measurements on viscoelastic anisotropic plates,” *The Journal of the Acoustical Society of America*, vol. 101, no. 3, pp. 1373–1379, 1997.

[13] S. D. Holland and D. E. Chimenti, “Air-coupled acoustic imaging with zero-group velocity lamb modes,” *Applied Physics Letters*, vol. 83, no. 13, pp. 2704–2706, 2003.

[14] M. Anes, K. D. Lohne, P. Lunde, and M. Vestrheim, “Finite element analysis of acoustic beam interactions with a plate at normal incidence. comparison with a 3d angular spectrum method and measurements.” *Proceedings of the 34th Scandinavian Symposium on Physocical Acoustics, Geilo, Norway, 30. Jan. - 2. Feb., 2011.*

[15] ——, “Normal incidence ultrasonic beam transmission through a water-immersed plate using a piezoelectric transducer. finite element modeling, angular spectrum method and measurements,” *Proceedings of the International Congress on Sound Vibration, Vilnius, Lithuania, 8-12 Jul., 2012*, pp. 12–20.

[16] ——, “Ultrasonic beam transmission through a water-immersed plate at oblique incidence using a piezoelectric source transducer. finite element - angular spectrum modeling and measurements,” *Proceedings IEEE International Ultrasonics Symposium, Dresden, Germany, 7-10 Oct., 2012*, pp. 1972–1977.

[17] S. H. Midtbø, “Beam diffraction effects in guided-wave transmission of fluid embedded elastic plate. influence of receiver distance and finite aperture,” Master’s thesis, Dept. of Physics and Technology, University of Bergen, Norway, 2018.

[18] M. Anes, K. D. Lohne, P. Lunde, and M. Vestrheim, “Transducer beam diffraction effects in sound transmission near leaky lamb modes in elastic plates at normal incidence,” *Proceedings IEEE International Ultrasonics Symposium, Taipei, Taiwan, 21-24 Oct., 2015*, p. 4.

[19] ——, “Finite aperture influence on energy concentration, frequency shift, and signal enhancement, for acoustic transmission in the negative group velocity region of the s1 leaky lamb mode,” *Proceedings IEEE International Ultrasonics Symposium, Tours, France, 11-16 Sep., 2016, 4p.*

[20] ——, “Beam diffraction effects in sound transmission of a fluid-embedded viscoelastic plate at normal incidence,” *Acoustical Society of America, 140 (1) (2016) EL67EL72.*

[21] I. Ravndal, “Normal incidence ultrasonic beam transmission through steel plates. measuring and modelling the transmission coefficient,” Master’s thesis, Dept. of Physics and Technology, University of Bergen, Norway, 2020.

[22] M. M. Sæther, “Customization of the angular spectrum method for calculating the acoustic piston field transmitted through a solid plate using MATLAB,” *MethodsX 10 (2023) 102037*.

[23] C. Prøytz, “Underwater ultrasonic transducer technology. construction, characterization and finite-element modeling.” Master’s thesis, Dept. of Physics and Technology, University of Bergen, Norway, 2022.

[24] L. E. Kinsler and A. R. Frey, *Fundamentals of Acoustics*, 4th ed. USA: John Wiley Sons Inc, 2000.

[25] P. Lunde, *Lecture notes in PHYS271: Acoustics, Chap. 7: Radiation and reception of acoustic waves*, Dept. of Physics and Technology, University of Bergen, Norway, 2022.

[26] M. Solberg, *Lecture notes in PHYS272: Acoustic transducers, Chap. 2: Circuit description of a transducer, Chap. 7: Calibration*, Dept. of Physics and Technology, University of Bergen, Norway, 2021.

[27] J. Kocbach, “Finite element modeling of ultrasonic piezoelectric transducers,” Ph.D. dissertation, Dept. of Physics, University of Bergen, Norway, 2000.

[28] P. Lunde, *Lecture notes in PHYS374: Selected topics in theoretical acoustics, Chapter 5: Elastic waves in solids*, Bergen, Norway, 2022.

[29] *CurveSnap.exe*, https://curvesnap.en.softonic.com/, Accessed: November 2022.

[30] *HP 33120A Function Generator/Arbitrary Waveform Generator Service Guide*, Hewlett Packard, USA, 1996.

[31] *Certificate of Calibration. PRECISION ACOUSTICS PVDF NEEDLE HYDROPHONE SERIAL NUMBER 1820 (Preamplifier SN PA110078, DC coupler SN DCPS223)*, Precision Acoustic Ltd., Dorset, U.K., 2011.

[32] *CALIBRATION CERTIFICATE. (Hydrophone SN 1848 needle of diameter 1 mm, Preamplifier SN PA10028, DC coupler SN 606)*, Precision Acoustic Ltd., Dorset, U.K., 2011.

[33] *10 MHz High Input Impedance Voltage Amplifier*, Femto, Germany, 2023.

[34] *Model 3940*, Krohn-Hite, Brockton, USA, 2022.

[35] *MSO3000 and DPO3000 Series Digital Phosphor Oscilloscopes - User Manual*, Tektronix, USA, 2022.

[36] *404XE Series Linear Positioning Manual*, Parker Hannifin Corporation, Pennsylvania, USA, 2021.

[37] *PRS-110 Precision Rotation Stage User Manual*, PiMicos GmbH, Eschbach, Germany, 2022.

[38] *Linear Motor Stage LMS-100*, PiMicos GmbH, Eschbach, Germany, 2022.

[39] *Quick guide to Precision Measuring Instruments*, ITM Instruments Inc., USA, 2011.

[40] *Operation and service manual Model 4192A LF Impedance Analyzer*, Yokogawa-Hewlett-Packard Ltd, Tokyo, Japan, 1981.

[41] *High quality components and materials for the electronics industry*, Meggit Ferroperm Piezoceramics, Kvistgaard, Denmark, 2013.

[42] *Eccosorb MF114*, Lard Technologies - Emerson Cuming Microwave Products, Massachusetts, USA, 2013.

[43] MG Chemicals, 9347 - 193rd Street, B.C., Canada V4N 4E7, 2013, 2013.

[44] *HCP70*, Divinycell International AB, DIAB Group, Laholm, Sweden, 2013.

[45] *Type Pz27 datasheet*, CTS Ferroperm, Kvistgaard, Denmark, 2020.

[46] *Eccosorb MF114*, Lard Technologies - Emerson Cuming Microwave Products, Massachusetts, USA, 2022.

[47] *8330D - Silver Conductive Epoxy Adhesive*, MG Chemicals, Ontario, Canada, 2021.

[48] *Cold mounting systems for all materialgraphic applications*, Struers ApS, Ballerup, Denmark, 2000.

[49] J. 1, *Evaluation of measurement data - Guide to the expression of uncertainty in measurement*, fist edition. jcgm 100: 2008 (gum 1995 with minor corrections) ed. Bergen, Norway: JCGM, 2008.

[50] *PRESSURE/INTENSITY MEASUREMENTS*, Precision Acoustic Ltd., Dorset, U.K., 2011.

[51] H. Økland, *Private communication, mesh structure in FEMP 6.1*, Dept. of Physics and Technology, University of Bergen, Norway, 2023.

[52] M. Aanes, *Data files from PhD work of Aanes [8], now NDT Global, at acoustic laboratory at UiB*, Dept. of Physics and Technology, University of Bergen, Norway, 2023.

[53] C. Prøytz, *Data files from Master work of Prøytz [23], now WSP, at acoustic laboratory at UiB*, Dept. of Physics and Technology, University of Bergen, Norway, 2023.

Appendix A

FEMP

A.1 ”read_inn_project.m” file

```
function [read]=read_inn_project(read,commands);
%%%%%%%%%%%%%%%%%%%%%%%%%%%%%%%%%%%%%%%%%%%%%%%%%%%%%%%%%%%%%%%%%%%%%
% Read .inn-file. Note that this function calls a project specific
% read_inn_project.m which should be in the working directory
%
% Part of FEMP (Finite Element Modeling of Piezoelectric structures)
% Programmed by Jan Kocbach (jan@kocbach.net)
% (C) 2000 Jan Kocbach. This file is free software;  you can redistribute
% it and/or modify it only under the the terms of the GNU GENERAL PUBLIC
% LICENSE which should be included along with this file.
% (C) 2000-2010 Christian Michelsen Research AS
%%%%%%%%%%%%%%%%%%%%%%%%%%%%%%%%%%%%%%%%%%%%%%%%%%%%%%%%%%%%%%%%%%%%%

% Put a file read_inn_project.m in your project directory to define local
% FEMP input commands. Also include init_const_project.m in this directory
% and define the comtransducercpnds there.
global glob;
read=read;

%% transducercp_egen
    if ~isempty(read.transducercp)
        read.points=[]; read.areas=[]; read.materials=[]; read.dof=[]; read.restraints=[];

        fy=read.transducercp(1,1,:);
        fx2=read.transducercp(1,2,:);
        fx=read.transducercp(1,30,:);
        ay=read.transducercp(1,3,:);
        py=read.transducercp(1,4,:);
        px=read.transducercp(1,5,:);
        by=read.transducercp(1,6,:);
        airy1=read.transducercp(1,7,:);
        airy2=read.transducercp(1,26,:);
        airy3=read.transducercp(1,27,:);
        airx1=read.transducercp(1,8,:);
        airx2=read.transducercp(1,28,:);
        airx3=read.transducercp(1,29,:);
        gap=read.transducercp(1,31,:);
        cy=read.transducercp(1,9,:);
        cx=read.transducercp(1,10,:);
        front=read.transducercp(1,11,:);
        eladhesive=read.transducercp(1,12,:);
        piezo=read.transducercp(1,13,:);
        back=read.transducercp(1,14,:);
        casing=read.transducercp(1,15,:);
%         elr=read.transducercp(1,16,:);    %not working, writing directly
%         elz=read.transducercp(1,17,:);    %not working, writing directly
        rfluid=read.transducercp(1,18,:);
%         theta=read.transducercp(1,19,:);    %not used
        matnumfluid=read.transducercp(1,20,:);
        flr=read.transducercp(1,21,:);
        flz=read.transducercp(1,22,:);
        inflr=read.transducercp(1,23,:);
        inflz=read.transducercp(1,24,:);
        luft=read.transducercp(1,25,:);
        elr=3;
        elz = 3;
        elz_fluid = 29;
        yy=-cy/2;

        for s=1:size(px,3)
            rfluidtemp=0+rfluid;
            rinffluid=rfluidtemp*2;
            read.points(:,:,s)=...
                [1 0 yy;
                2 0 fy+yy;
                3 airx1 fy+yy;
```

```
4 airx1 yy;
5 airx2 fy+yy;
6 airx2 yy;
7 airx3 fy+yy;
8 airx3 yy;
9 px fy+yy;
10 px yy;
11 fx2 fy+yy;
12 fx2 yy;
13 0 ay+yy;
14 airx1 ay+yy;
15 airx2 ay+yy;
16 airx3 ay+yy;
17 px ay+yy;
18 fx2 ay+yy;
19 0 py+yy;
20 airx1 py+yy;
21 airx2 py+yy;
22 airx3 py+yy;
23 px py+yy;
24 fx2 py+yy;
25 0 by+yy;
26 airx1 by+yy;
27 airx2 by+yy;
28 airx3 by+yy;
29 px by+yy;
30 fx2 by+yy;
31 airx1 airy1+yy;
32 airx2 airy1+yy;
33 airx3 airy1+yy;
34 px airy1+yy;
35 fx2 airy1+yy;
36 airx2 airy2+yy;
37 airx3 airy2+yy;
38 px airy2+yy;
39 fx2 airy2+yy;
40 airx3 airy3+yy;
41 px airy3+yy;
42 fx2 airy3+yy;
43 0 airy1+yy;
44 0 airy2+yy;
45 airx1 airy2+yy;
46 0 airy3+yy;
47 airx1 airy3+yy;
48 airx2 airy3+yy;
49 0 cy+yy;
50 airx1 cy+yy;
51 airx2 cy+yy;
52 airx3 cy+yy;
53 px cy+yy;
54 fx2 cy+yy;
55 cx cy+yy;
56 cx airy3+yy;
57 cx airy2+yy;
58 cx airy1+yy;
59 cx by+yy;
60 cx py+yy;
61 cx ay+yy;
62 cx fy+yy;
63 cx yy;
64 fx cy+yy;
65 fx airy3+yy;
66 fx airy2+yy;
67 fx airy1+yy;
68 fx by+yy;
69 fx py+yy;
70 fx ay+yy;
71 fx fy+yy;
72 fx yy;
73 0 0;
120 0 gap+yy;
121 airx1 gap+yy;
122 airx2 gap+yy;
123 airx3 gap+yy;
124 px gap+yy;
125 fx2 gap+yy;
126 fx gap+yy;
127 cx gap+yy;
%   fluid
74 0 -rfluid;
75 rfluid*cos(atan(yy/airx1))        -rfluid*sin(atan(yy/airx1));
76 rfluid*cos(atan(yy/airx2))        -rfluid*sin(atan(yy/airx2));
77 rfluid*cos(atan(yy/airx3))        -rfluid*sin(atan(yy/airx3));
78 rfluid*cos(atan(yy/px))           -rfluid*sin(atan(yy/px));
79 rfluid*cos(atan(yy/fx2))          -rfluid*sin(atan(yy/fx2));
80 rfluid*cos(atan(yy/fx))           -rfluid*sin(atan(yy/fx));
81 rfluid*cos(atan(yy/cx))           -rfluid*sin(atan(yy/cx));
82 rfluid*cos(atan((yy+airy3)/cx))   rfluid*sin(atan((yy+airy3)/cx));
83 rfluid*cos(atan((yy+airy2)/cx))   rfluid*sin(atan((yy+airy2)/cx));
84 rfluid*cos(atan((yy+airy1)/cx))   rfluid*sin(atan((yy+airy1)/cx));
85 rfluid*cos(atan((yy+by)/cx))      rfluid*sin(atan((yy+by)/cx));
86 rfluid*cos(atan((yy+py)/cx))      rfluid*sin(atan((yy+py)/cx));
87 rfluid*cos(atan((yy+ay)/cx))      rfluid*sin(atan((yy+ay)/cx));
88 rfluid*cos(atan((yy+fy)/cx))      rfluid*sin(atan((yy+fy)/cx));
89 rfluid*cos(atan(yy/cx))           rfluid*sin(atan(yy/cx));
90 rfluid*cos(atan(yy/fx))           rfluid*sin(atan(yy/fx));
91 rfluid*cos(atan(yy/fx2))          rfluid*sin(atan(yy/fx2));
92 rfluid*cos(atan(yy/px))           rfluid*sin(atan(yy/px));
93 rfluid*cos(atan(yy/airx3))        rfluid*sin(atan(yy/airx3));
94 rfluid*cos(atan(yy/airx2))        rfluid*sin(atan(yy/airx2));
95 rfluid*cos(atan(yy/airx1))        rfluid*sin(atan(yy/airx1));
96 0 rfluid;
128 rfluid*cos(atan((yy+gap)/cx))   rfluid*sin(atan((yy+gap)/cx));
```

```
                %   inf fluid
                97 0 -rinffluid;
                98 rinffluid*cos(atan(yy/airx1))        -rinffluid*sin(atan(yy/airx1));
                99 rinffluid*cos(atan(yy/airx2))        -rinffluid*sin(atan(yy/airx2));
                100 rinffluid*cos(atan(yy/airx3))        -rinffluid*sin(atan(yy/airx3));
                101 rinffluid*cos(atan(yy/px))           -rinffluid*sin(atan(yy/px));
                102 rinffluid*cos(atan(yy/fx2))          -rinffluid*sin(atan(yy/fx2));
                103 rinffluid*cos(atan(yy/fx))           -rinffluid*sin(atan(yy/fx));
                104 rinffluid*cos(atan(yy/cx))           -rinffluid*sin(atan(yy/cx));
                105 rinffluid*cos(atan((yy+airy3)/cx))   ...
                    rinffluid*sin(atan((yy+airy3)/cx));
                106 rinffluid*cos(atan((yy+airy2)/cx))   ...
                    rinffluid*sin(atan((yy+airy2)/cx));
                107 rinffluid*cos(atan((yy+airy1)/cx))   ...
                    rinffluid*sin(atan((yy+airy1)/cx));
                108 rinffluid*cos(atan((yy+by)/cx))      rinffluid*sin(atan((yy+by)/cx));
                109 rinffluid*cos(atan((yy+py)/cx))      rinffluid*sin(atan((yy+py)/cx));
                110 rinffluid*cos(atan((yy+ay)/cx))      rinffluid*sin(atan((yy+ay)/cx));
                111 rinffluid*cos(atan((yy+fy)/cx))      rinffluid*sin(atan((yy+fy)/cx));
                112 rinffluid*cos(atan(yy/cx))           rinffluid*sin(atan(yy/cx));
                113 rinffluid*cos(atan(yy/fx))           rinffluid*sin(atan(yy/fx));
                114 rinffluid*cos(atan(yy/fx2))          rinffluid*sin(atan(yy/fx2));
                115 rinffluid*cos(atan(yy/px))           rinffluid*sin(atan(yy/px));
                116 rinffluid*cos(atan(yy/airx3))        rinffluid*sin(atan(yy/airx3));
                117 rinffluid*cos(atan(yy/airx2))        rinffluid*sin(atan(yy/airx2));
                118 rinffluid*cos(atan(yy/airx1))        rinffluid*sin(atan(yy/airx1));
                119 0 rinffluid;
                129 rinffluid*cos(atan((yy+gap)/cx))     rinffluid*sin(atan((yy+gap)/cx));
                ];

            read.areas(:,:,s)=...
                [1, 2,3,4,1,    elr,elz,0,0;    %front layer
                1, 3,5,6,4,     elr,elz,0,0;
                1, 5,7,8,6,     elr,elz,0,0;
                1, 7,9,10,8,    elr,elz,0,0;
                1, 9,11,12,10,  elr,elz,0,0;
                1, 11,71,72,12, elr,elz,0,0;
                %
                2, 13,14,3,2,   elr,elz,0,0;    %cond.adhesive
                2, 14,15,5,3,   elr,elz,0,0;
                2, 15,16,7,5,   elr,elz,0,0;
                2, 16,17,9,7,   elr,elz,0,0;
                2, 17,18,11,9,  elr,elz,0,0;
                2, 18,70,71,11, elr,elz,0,0;
                %
                3, 19,20,14,13, elr,elz,0,0;    %piezodisc
                3, 20,21,15,14, elr,elz,0,0;
                3, 21,22,16,15, elr,elz,0,0;
                3, 22,23,17,16, elr,elz,0,0;
                %
                4, 23,24,18,17, elr,elz,0,0;    %back layer
                4, 25,26,20,19, elr,elz,0,0;
                4, 26,27,21,20, elr,elz,0,0;
                4, 27,28,22,21, elr,elz,0,0;
                4, 28,29,23,22, elr,elz,0,0;
                4, 29,30,24,23, elr,elz,0,0;
                4, 31,32,27,26, elr,elz,0,0;
                4, 32,33,28,27, elr,elz,0,0;
                4, 33,34,29,28, elr,elz,0,0;
                4, 34,35,30,29, elr,elz,0,0;
                4, 36,37,33,32, elr,elz,0,0;
                4, 37,38,34,33, elr,elz,0,0;
                4, 38,39,35,34, elr,elz,0,0;
                4, 40,41,38,37, elr,elz,0,0;
                4, 41,42,39,38, elr,elz,0,0;
                %
                5, 49,50,121,120, elr,elz,0,0;  %casing
                5, 50,51,122,121, elr,elz,0,0;
                5, 51,52,123,122, elr,elz,0,0;
                5, 52,53,124,123, elr,elz,0,0;
                5, 53,54,125,124, elr,elz,0,0;
                5, 54,64,126,125, elr,elz,0,0;
                5, 125,126,65,42, elr,elz,0,0;
                5, 64,55,127,126, elr,elz,0,0;
                5, 126,127,56,65, elr,elz,0,0;
                5, 42,65,66,39, elr,elz,0,0;
                5, 65,56,57,66, elr,elz,0,0;
                5, 39,66,67,35, elr,elz,0,0;
                5, 66,57,58,67, elr,elz,0,0;
                5, 35,67,68,30, elr,elz,0,0;
                5, 67,58,59,68, elr,elz,0,0;
                5, 30,68,69,24, elr,elz,0,0;
                5, 68,59,60,69, elr,elz_fluid,0,0;
                5, 24,69,70,18, elr,elz,0,0;
                5, 69,60,61,70, elr,elz,0,0;
                5, 70,61,62,71, elr,elz,0,0;
                5, 71,62,63,72, elr,elz,0,0;
                %
%                 6, 43,31,26,25, elr,elz,0,0;    %air  - not to be used
%                 6, 44,45,31,43, elr,elz,0,0;
%                 6, 45,36,32,31, elr,elz,0,0;
%                 6, 46,47,45,44, elr,elz,0,0;
%                 6, 47,48,36,45, elr,elz,0,0;
%                 6, 48,40,37,36, elr,elz,0,0;
                %
%                 6,                              %air gap  - not to be used
                %
                7, 50,49,74,75, flr,flz,0,73;   %Finite fluid
                7, 51,50,75,76, flr,flz,0,73;
                7, 52,51,76,77, flr,flz,0,73;
                7, 53,52,77,78, flr,flz,0,73;
                7, 54,53,78,79, flr,flz,0,73;
                7, 64,54,79,80, flr,flz,0,73;
```

```
                7, 55,64,80,81, flr,flz,0,73;
                7, 127,55,81,128, flr,flz,0,73;
                7, 56,127,128,82, flr,flz,0,73;
                7, 57,56,82,83, flr,flz,0,73;
                7, 58,57,83,84, flr,flz,0,73;
                7, 59,58,84,85, flr,flz,0,73;
                7, 60,59,85,86, flr,flz,0,73;
                7, 61,60,86,87, flr,flz,0,73;
                7, 62,61,87,88, flr,flz,0,73;
                7, 63,62,88,89, flr,flz,0,73;
                7, 72,63,89,90, flr,flz,0,73;
                7, 12,72,90,91, flr,flz,0,73;
                7, 10,12,91,92, flr,flz,0,73;
                7, 8,10,92,93,  flr,flz,0,73;
                7, 6,8,93,94,   flr,flz,0,73;
                7, 4,6,94,95,   flr,flz,0,73;
                7, 1,4,95,96,   flr,flz,0,73;
                %
                8, 75,74,97,98,   inflr,inflz,73,73;  %Infinite fluid
                8, 76,75,98,99,   inflr,inflz,73,73;
                8, 77,76,99,100,  inflr,inflz,73,73;
                8, 78,77,100,101, inflr,inflz,73,73;
                8, 79,78,101,102, inflr,inflz,73,73;
                8, 80,79,102,103, inflr,inflz,73,73;
                8, 81,80,103,104, inflr,inflz,73,73;
                8, 128,81,104,129, inflr,inflz,73,73;
                8, 82,128,129,105, inflr,inflz,73,73;
                8, 83,82,105,106, inflr,inflz,73,73;
                8, 84,83,106,107, inflr,inflz,73,73;
                8, 85,84,107,108, inflr,inflz,73,73;
                8, 86,85,108,109, inflr,inflz,73,73;
                8, 87,86,109,110, inflr,inflz,73,73;
                8, 88,87,110,111, inflr,inflz,73,73;
                8, 89,88,111,112, inflr,inflz,73,73;
                8, 90,89,112,113, inflr,inflz,73,73;
                8, 91,90,113,114, inflr,inflz,73,73;
                8, 92,91,114,115, inflr,inflz,73,73;
                8, 93,92,115,116, inflr,inflz,73,73;
                8, 94,93,116,117, inflr,inflz,73,73;
                8, 95,94,117,118, inflr,inflz,73,73;
                8, 96,95,118,119, inflr,inflz,73,73;
                ];

            read.materials(:,:,s)=...
            [1 glob.globvariables.mechanic front;
             2 glob.globvariables.mechanic eladhesive;
             3 glob.globvariables.piezo piezo;
             4 glob.globvariables.mechanic back;
             5 glob.globvariables.mechanic casing;
             6 glob.globvariables.fluid luft;
             7 glob.globvariables.fluid matnumfluid;
             8 glob.globvariables.infinitefluid matnumfluid];

        read.dof(:,:,s)=[-1 1 ay+yy-1e-9 ay+yy+1e-9 glob.free.ep];
        read.restraints(:,:,s)=[-1 1 py+yy-1e-9 py+yy+1e-9 glob.free.ep 1];

        end
    end
```

A.2 ”init_const.m” file

```
%%%%%%%%%%%%%%%%%%%%%%%%%%%%%%%%%%%%%%%%%%%%%%%%%%%%%%%%%%%%%%%%%%%%%
% Initialization of constants for FEMP
% Part of FEMP (Finite Element Modeling of Piezoelectric structures)
% Programmed by Jan Kocbach (jan@kocbach.net)
% (C) 2000 Jan Kocbach. This file is free software;  you can redistribute
% it and/or modify it only under the the terms of the GNU GENERAL PUBLIC
% LICENSE which should be included along with this file.
% (C) 2000-2010 Christian Michelsen Research AS
%%%%%%%%%%%%%%%%%%%%%%%%%%%%%%%%%%%%%%%%%%%%%%%%%%%%%%%%%%%%%%%%%%%%%


%%%%%%%%%%%%%%%%%%%%%%%%%%%%%%%%%%%%%%%%%%%%%%%%%%%%%%%%%%%%%%%%%%%%%
% INIT_CONST_PROJECT: Initialize constants - project specifix
%%%%%%%%%%%%%%%%%%%%%%%%%%%%%%%%%%%%%%%%%%%%%%%%%%%%%%%%%%%%%%%%%%%%%

% Make a copy of this file in your project folder to
% make project specific definitions

commands = [commands,'transducercp'];
```

A.3 ”CP1.inn” file

```
set
fy, -1.12315e-3;
fx2, 10.5687e-3;
fx, 11.5157e-3;
ay, -1.15876e-3;
py, -5.13175e-3;
px, 8.08537e-3;
by,  -31.51265e-3;
airy1, -34.845983333333e-3;
airy2, -38.179316666667e-3;
airy3, -41.51265e-3;
airx1, 2.5e-3;
airx2, 5e-3;
airx3, 7.5e-3;
gap, -42.01265e-3;
cy, -45.01e-3;
cx, 12.6147e-3;
front, 70;
eladhesive, 30;
piezo, 1;
back, 95;
casing, 80;
luft, 10101;
matnumfluid, 100;
elr, 0;
elz, 0;
rfluid, 80e-3;
flr, 3;
flz, 3;
inflr, 1;
inflz, 1;
theta, 0;
end


transducercp
fy,fx2,ay,py,px,by,airy1,airx1,cy,cx,front,eladhesive,piezo,back,casing,elr,elt,rfluid, ...
    theta,matnumfluid,flr,flz,inflr,inflz,luft,airy2,airy3,airx2,airx3,fx,gap
end

materialfile
43
end

# for hoyeste frekvensen
meshingtype
elementsperwavelength,1e6
end

viewmesh
0
end

# The order of the finite elements is 2 - i.e. 8 node isoparametric elements are applied
order
2
end

# The order of the infinite elements is set to 10. -> s=0.32
infiniteorder
12
end

# husk delta f --> delta Rinf ( z=s*lambda/a^2=s*c/(f*a*2) )
directharmonicanalysis
200e3,1e3,1000e3,complex_loss
end

#tar inn frekvensene fra under "directharmonicanalysis"
#admittance
#0,0,0
#end

#nearfieldpressure
#0,0,0,-1,1,-1,1
#end

# Calculate far-field pressure for the frequencies used in the time-harmonic
# analysis. Calculate out to 3 times the distance at which the infinite
# elements are applied (10*7.0 mm= 70.0 mm), with 20 divisions per 7.0 mm.

# farfieldpressure
# 0,0,0,40.4e-3,20
# end

sensitivity
0,0,0,1
end

#directivity
#0,0,0,1
#end

#onaxispressure
#0,0,0,10,20
#end

save
sensitivity,sensitivity_f
end
```

A.4 ”material4.dat” file

```
##############################
#    MA material data
##############################
_________________________________________________________________________________ 10
        10     front
# mechanical terms
 1.44281e+10 8.72812e+09 8.72812e+09 0.00000e+00 0.00000e+00 0.00000e+00
 8.72812e+09 1.44281e+10 8.72812e+09 0.00000e+00 0.00000e+00 0.00000e+00
 8.72812e+09 8.72812e+09 1.44281e+10 0.00000e+00 0.00000e+00 0.00000e+00
 0.00000e+00 0.00000e+00 0.00000e+00 2.85000e+09 0.00000e+00 0.00000e+00
 0.00000e+00 0.00000e+00 0.00000e+00 0.00000e+00 2.85000e+09 0.00000e+00
 0.00000e+00 0.00000e+00 0.00000e+00 0.00000e+00 0.00000e+00 2.85000e+09
# coupling terms
 0.00000e+00 0.00000e+00 0.00000e+00 0.00000e+00 0.00000e+00 0.00000e+00
 0.00000e+00 0.00000e+00 0.00000e+00 0.00000e+00 0.00000e+00 0.00000e+00
 0.00000e+00 0.00000e+00 0.00000e+00 0.00000e+00 0.00000e+00 0.00000e+00
# dielectric terms
 0.00000e+00 0.00000e+00 0.00000e+00
 0.00000e+00 0.00000e+00 0.00000e+00
 0.00000e+00 0.00000e+00 0.00000e+00
# density and damping coefficients
 2.85000e+03 2.00000e+01 0.00000e+00
# end of material data


_________________________________________________________________________________ 20
        20     conductive adhesive
# mechanical terms
 6.76260e+09 2.08260e+09 2.08260e+09 0.00000e+00 0.00000e+00 0.00000e+00
 2.08260e+09 6.76260e+09 2.08260e+09 0.00000e+00 0.00000e+00 0.00000e+00
 2.08260e+09 2.08260e+09 6.76260e+09 0.00000e+00 0.00000e+00 0.00000e+00
 0.00000e+00 0.00000e+00 0.00000e+00 2.34000e+09 0.00000e+00 0.00000e+00
 0.00000e+00 0.00000e+00 0.00000e+00 0.00000e+00 2.34000e+09 0.00000e+00
 0.00000e+00 0.00000e+00 0.00000e+00 0.00000e+00 0.00000e+00 2.34000e+09
# coupling terms
 0.00000e+00 0.00000e+00 0.00000e+00 0.00000e+00 0.00000e+00 0.00000e+00
 0.00000e+00 0.00000e+00 0.00000e+00 0.00000e+00 0.00000e+00 0.00000e+00
 0.00000e+00 0.00000e+00 0.00000e+00 0.00000e+00 0.00000e+00 0.00000e+00
# dielectric terms
 0.00000e+00 0.00000e+00 0.00000e+00
 0.00000e+00 0.00000e+00 0.00000e+00
 0.00000e+00 0.00000e+00 0.00000e+00
# density and damping coefficients
 2.34000e+03 5.00000e+01 0.00000e+00
# end of material data

_________________________________________________________________________________ 30
        30     piezo      piezodisc
# mechanical terms
 1.20250e+011 7.62000e+010 7.42000e+010 0.00000e+000 0.00000e+000 0.00000e+000
 7.62000e+010 1.20250e+011 7.42000e+010 0.00000e+000 0.00000e+000 0.00000e+000
 7.42000e+010 7.42000e+010 1.10050e+011 0.00000e+000 0.00000e+000 0.00000e+000
 0.00000e+000 0.00000e+000 0.00000e+000 2.11000e+010 0.00000e+000 0.00000e+000
 0.00000e+000 0.00000e+000 0.00000e+000 0.00000e+000 2.11000e+010 0.00000e+000
 0.00000e+000 0.00000e+000 0.00000e+000 0.00000e+000 0.00000e+000 2.20250e+010
# coupling terms
 0.00000e+000 0.00000e+000 0.00000e+000 0.00000e+000 1.12000e+001 0.00000e+000
 0.00000e+000 0.00000e+000 0.00000e+000 1.12000e+001 0.00000e+000 0.00000e+000
 -5.40000e+000 -5.40000e+000 1.70000e+001 0.00000e+000 0.00000e+000 0.00000e+000
# dielectric terms
 8.11044e-009 0.00000e+000 0.00000e+000
 0.00000e+000 8.11044e-009 0.00000e+000
 0.00000e+000 0.00000e+000 8.14585e-009
# density and damping coefficients
 7.70000e+003 0.00000e+000 0.00000e+000
# mechanical Q-factors
 9.60000e+001 7.00000e+001 1.20000e+002 0.00000e+000 0.00000e+000 0.00000e+000
 7.00000e+001 9.60000e+001 1.20000e+002 0.00000e+000 0.00000e+000 0.00000e+000
 1.20000e+002 1.20000e+002 1.90000e+002 0.00000e+000 0.00000e+000 0.00000e+000
 0.00000e+000 0.00000e+000 0.00000e+000 7.50000e+001 0.00000e+000 0.00000e+000
 0.00000e+000 0.00000e+000 0.00000e+000 0.00000e+000 7.50000e+001 0.00000e+000
 0.00000e+000 0.00000e+000 0.00000e+000 0.00000e+000 0.00000e+000 1.30000e+001
# piezoelectric Q-factors
 0.00000e+000 0.00000e+000 0.00000e+000 0.00000e+000 -2.00000e+002 0.00000e+000
 0.00000e+000 0.00000e+000 0.00000e+000 -2.00000e+002 0.00000e+000 0.00000e+000
 -1.66000e+002 -1.66000e+002 -3.2400e+002 0.00000e+000 0.00000e+000 0.00000e+000
# dielectric Q-factors
 -5.00000e+001 0.00000e+000 0.00000e+000
 0.00000e+000 -5.00000e+001 0.00000e+000
 0.00000e+000 0.00000e+000 -1.30000e+002
# end of material data

_________________________________________________________________________________ 40
        40     backing
# mechanical terms
 7.73289e+08 3.63901e+08 3.63901e+08 0.00000e+00 0.00000e+00 0.00000e+00
 3.63901e+08 7.73289e+08 3.63901e+08 0.00000e+00 0.00000e+00 0.00000e+00
 3.63901e+08 3.63901e+08 7.73289e+08 0.00000e+00 0.00000e+00 0.00000e+00
 0.00000e+00 0.00000e+00 0.00000e+00 2.04694e+08 0.00000e+00 0.00000e+00
 0.00000e+00 0.00000e+00 0.00000e+00 0.00000e+00 2.04694e+08 0.00000e+00
 0.00000e+00 0.00000e+00 0.00000e+00 0.00000e+00 0.00000e+00 2.04694e+08
# coupling terms
 0.00000e+00 0.00000e+00 0.00000e+00 0.00000e+00 0.00000e+00 0.00000e+00
 0.00000e+00 0.00000e+00 0.00000e+00 0.00000e+00 0.00000e+00 0.00000e+00
 0.00000e+00 0.00000e+00 0.00000e+00 0.00000e+00 0.00000e+00 0.00000e+00
# dielectric terms
 0.00000e+00 0.00000e+00 0.00000e+00
 0.00000e+00 0.00000e+00 0.00000e+00
```

```
 0.00000e+00 0.00000e+00 0.00000e+00
# density and damping coefficients
 3.00000e+02 2.50000e+01 0.00000e+00
# end of material data

                                                                            51
        51      casing
# mechanical terms
 2.67267e+11 1.10517e+11 1.10517e+11 0.00000e+00 0.00000e+00 0.00000e+00
 1.10517e+11 2.67267e+11 1.10517e+11 0.00000e+00 0.00000e+00 0.00000e+00
 1.10517e+11 1.10517e+11 2.67267e+11 0.00000e+00 0.00000e+00 0.00000e+00
 0.00000e+00 0.00000e+00 0.00000e+00 7.83752e+10 0.00000e+00 0.00000e+00
 0.00000e+00 0.00000e+00 0.00000e+00 0.00000e+00 7.83752e+10 0.00000e+00
 0.00000e+00 0.00000e+00 0.00000e+00 0.00000e+00 0.00000e+00 7.83752e+10
# coupling terms
 0.00000e+00 0.00000e+00 0.00000e+00 0.00000e+00 0.00000e+00 0.00000e+00
 0.00000e+00 0.00000e+00 0.00000e+00 0.00000e+00 0.00000e+00 0.00000e+00
 0.00000e+00 0.00000e+00 0.00000e+00 0.00000e+00 0.00000e+00 0.00000e+00
# dielectric terms
 0.00000e+00 0.00000e+00 0.00000e+00
 0.00000e+00 0.00000e+00 0.00000e+00
 0.00000e+00 0.00000e+00 0.00000e+00
# density and damping coefficients
 8.00000e+03 1.00000e+03 0.00000e+00
# end of material data

                                                                            10 000
     10000      fluid             water
 1.00000e+03 2.25000e+09 0.00000e+00 0.00000e+00

                                                                            10 101
     10101      fluid                 air    Magne Aanes FEM approach
 1.21000e+00 1.34983e+05 0.00000e+00 0.00000e+00





##############################
#   CP1 and CP2 material data
##############################
                                                                            70
       70      front
# mechanical terms
 1.44281e+10 8.72813e+09 8.72813e+09 0.00000e+00 0.00000e+00 0.00000e+00
 8.72813e+09 1.44281e+10 8.72813e+09 0.00000e+00 0.00000e+00 0.00000e+00
 8.72813e+09 8.72813e+09 1.44281e+10 0.00000e+00 0.00000e+00 0.00000e+00
 0.00000e+00 0.00000e+00 0.00000e+00 2.85000e+09 0.00000e+00 0.00000e+00
 0.00000e+00 0.00000e+00 0.00000e+00 0.00000e+00 2.85000e+09 0.00000e+00
 0.00000e+00 0.00000e+00 0.00000e+00 0.00000e+00 0.00000e+00 2.85000e+09
# coupling terms
 0.00000e+00 0.00000e+00 0.00000e+00 0.00000e+00 0.00000e+00 0.00000e+00
 0.00000e+00 0.00000e+00 0.00000e+00 0.00000e+00 0.00000e+00 0.00000e+00
 0.00000e+00 0.00000e+00 0.00000e+00 0.00000e+00 0.00000e+00 0.00000e+00
# dielectric terms
 0.00000e+00 0.00000e+00 0.00000e+00
 0.00000e+00 0.00000e+00 0.00000e+00
 0.00000e+00 0.00000e+00 0.00000e+00
# density and damping coefficients
 2.85000e+03 2.00000e+01 0.00000e+00
# end of material data

                                                                            30
        30      conductive adhesive
# mechanical terms
 6.76260e+09 2.08290e+09 2.08290e+09 0.00000e+00 0.00000e+00 0.00000e+00
 2.08290e+09 6.76260e+09 2.08290e+09 0.00000e+00 0.00000e+00 0.00000e+00
 2.08290e+09 2.08290e+09 6.76260e+09 0.00000e+00 0.00000e+00 0.00000e+00
 0.00000e+00 0.00000e+00 0.00000e+00 2.34000e+09 0.00000e+00 0.00000e+00
 0.00000e+00 0.00000e+00 0.00000e+00 0.00000e+00 2.34000e+09 0.00000e+00
 0.00000e+00 0.00000e+00 0.00000e+00 0.00000e+00 0.00000e+00 2.34000e+09
# coupling terms
 0.00000e+00 0.00000e+00 0.00000e+00 0.00000e+00 0.00000e+00 0.00000e+00
 0.00000e+00 0.00000e+00 0.00000e+00 0.00000e+00 0.00000e+00 0.00000e+00
 0.00000e+00 0.00000e+00 0.00000e+00 0.00000e+00 0.00000e+00 0.00000e+00
# dielectric terms
 0.00000e+00 0.00000e+00 0.00000e+00
 0.00000e+00 0.00000e+00 0.00000e+00
 0.00000e+00 0.00000e+00 0.00000e+00
# density and damping coefficients
 2.34000e+03 5.00000e+01 0.00000e+00
# end of material data

                                                                            1
       1      piezo     piezodisc
# mechanical terms
 1.18750e+11 7.43000e+10 7.42500e+10 0.00000e+00 0.00000e+00 0.00000e+00
 7.43000e+10 1.18750e+11 7.42500e+10 0.00000e+00 0.00000e+00 0.00000e+00
 7.42500e+10 7.42500e+10 1.12050e+11 0.00000e+00 0.00000e+00 0.00000e+00
 0.00000e+00 0.00000e+00 0.00000e+00 2.11000e+10 0.00000e+00 0.00000e+00
 0.00000e+00 0.00000e+00 0.00000e+00 0.00000e+00 2.11000e+10 0.00000e+00
 0.00000e+00 0.00000e+00 0.00000e+00 0.00000e+00 0.00000e+00 2.16000e+10
# coupling terms
 0.00000e+00 0.00000e+00 0.00000e+00 0.00000e+00 1.12000e+01 0.00000e+00
 0.00000e+00 0.00000e+00 0.00000e+00 1.12000e+01 0.00000e+00 0.00000e+00
 -5.40000e+00 -5.40000e+00 1.60389e+01 0.00000e+00 0.00000e+00 0.00000e+00
# dielectric terms
 8.11044e-09 0.00000e+00 0.00000e+00
 0.00000e+00 8.11044e-09 0.00000e+00
 0.00000e+00 0.00000e+00 8.14585e-09
# density and damping coefficients
 7.70000e+03 9.99000e+02 9.99000e+02
# mechanical Q-factors
 9.57500e+01 7.12400e+01 1.20190e+02 0.00000e+00 0.00000e+00 0.00000e+00
```

```
 7.12400e+01 9.57500e+01 1.20190e+02 0.00000e+00 0.00000e+00 0.00000e+00
 1.20190e+02 1.20190e+02 1.77990e+02 0.00000e+00 0.00000e+00 0.00000e+00
 0.00000e+00 0.00000e+00 0.00000e+00 7.50000e+01 0.00000e+00 0.00000e+00
 0.00000e+00 0.00000e+00 0.00000e+00 0.00000e+00 7.50000e+01 0.00000e+00
 0.00000e+00 0.00000e+00 0.00000e+00 0.00000e+00 0.00000e+00 3.15010e+02
# piezoelectric Q-factors
 0.00000e+00 0.00000e+00 0.00000e+00 0.00000e+00 -2.00000e+02 0.00000e+00
 0.00000e+00 0.00000e+00 0.00000e+00 -2.00000e+02 0.00000e+00 0.00000e+00
 -1.66000e+02 -1.66000e+02 -3.23770e+02 0.00000e+00 0.00000e+00 0.00000e+00
# dielectric Q-factors
 5.00000e+01 0.00000e+00 0.00000e+00
 0.00000e+00 5.00000e+01 0.00000e+00
 0.00000e+00 0.00000e+00 8.62800e+01
# end of material data

________________________________________________________________________________ 95
        95      backing
# mechanical terms
 1.91232e+10 9.56140e+09 9.56140e+09 0.00000e+00 0.00000e+00 0.00000e+00
 9.56140e+09 1.91232e+10 9.56140e+09 0.00000e+00 0.00000e+00 0.00000e+00
 9.56140e+09 9.56140e+09 1.91232e+10 0.00000e+00 0.00000e+00 0.00000e+00
 0.00000e+00 0.00000e+00 0.00000e+00 4.78090e+09 0.00000e+00 0.00000e+00
 0.00000e+00 0.00000e+00 0.00000e+00 0.00000e+00 4.78090e+09 0.00000e+00
 0.00000e+00 0.00000e+00 0.00000e+00 0.00000e+00 0.00000e+00 4.78090e+09
# coupling terms
 0.00000e+00 0.00000e+00 0.00000e+00 0.00000e+00 0.00000e+00 0.00000e+00
 0.00000e+00 0.00000e+00 0.00000e+00 0.00000e+00 0.00000e+00 0.00000e+00
 0.00000e+00 0.00000e+00 0.00000e+00 0.00000e+00 0.00000e+00 0.00000e+00
# dielectric terms
 0.00000e+00 0.00000e+00 0.00000e+00
 0.00000e+00 0.00000e+00 0.00000e+00
 0.00000e+00 0.00000e+00 0.00000e+00
# density and damping coefficients
 7.47000e+03 1.35000e+01 0.00000e+00
# end of material data

________________________________________________________________________________ 80
        80      casing
# mechanical terms
 2.67267e+11 1.18427e+11 1.18427e+11 0.00000e+00 0.00000e+00 0.00000e+00
 1.18427e+11 2.67267e+11 1.18427e+11 0.00000e+00 0.00000e+00 0.00000e+00
 1.18427e+11 1.18427e+11 2.67267e+11 0.00000e+00 0.00000e+00 0.00000e+00
 0.00000e+00 0.00000e+00 0.00000e+00 7.44200e+10 0.00000e+00 0.00000e+00
 0.00000e+00 0.00000e+00 0.00000e+00 0.00000e+00 7.44200e+10 0.00000e+00
 0.00000e+00 0.00000e+00 0.00000e+00 0.00000e+00 0.00000e+00 7.44200e+10
# coupling terms
 0.00000e+00 0.00000e+00 0.00000e+00 0.00000e+00 0.00000e+00 0.00000e+00
 0.00000e+00 0.00000e+00 0.00000e+00 0.00000e+00 0.00000e+00 0.00000e+00
 0.00000e+00 0.00000e+00 0.00000e+00 0.00000e+00 0.00000e+00 0.00000e+00
# dielectric terms
 0.00000e+00 0.00000e+00 0.00000e+00
 0.00000e+00 0.00000e+00 0.00000e+00
 0.00000e+00 0.00000e+00 0.00000e+00
# density and damping coefficients
 8.00000e+03 1.00000e+03 0.00000e+00
# end of material data

________________________________________________________________________________ 100
       100      fluid              water
 1.00000e+03 2.20523e+09 0.00000e+00 0.00000e+00
# end of material data

________________________________________________________________________________ 10 101
     10101      fluid               air
 1.21000e+00 1.34983e+05 0.00000e+00 0.00000e+00
```

Appendix B

ASM2

B.1 ”ASM_Adapt_FilonGauss.m” file

```
Om clear
warning('') % Clear lastwarn. A MATLAB lastwarn warning on badly scaled polynomial ...
    fitting is expected when using Filon method.
% The warning is OK because it triggers MATLAB to execute Gauss method instead of Filon.

%% Input parameters
f_vec = 350e3:1e3:1000e3; ,
% z_vec = 270e-3;   % distance piston to measuring point: 'freefield'
z_vec = 376.05e-3;  % distance piston to measuring point: 'plate'
r_vec = 0;
plate_or_freefield = 'plate';   % input argument: 'plate' , or 'freefield'

%% Input parameters numerical integration scheme
Err_tresh = 1e-1;      % Absolute local error tolerance in the first and last Gauss ...
    adaptive method and the Filon-type adaptive method
Err_tresh_peak = 1e-1;   % Absolute local error tolerance in second Gauss method ...
    around the peak. Usually set higher than Err_tresh
eta_step_init = 1e-3;    % Initial staring step size
IntegrationBoundary_DeltaAbove_h_f = 200;   % Set upper integration limit. Sets eta ...
    limit above h_f.
FilonMethodStarts_OscPeriodCutOff_or_EtaCutoff = 0.2; % Typical value: 0.2. Defines ...
    when Filon method kicks in.
% For a value set in the range <0,10>, a eta period in the integrand is defined when ...
    Filon method kicks in. For a value set
% outside <0,10>, Filon method kicks in at the set value (for inf, the Gauss is always ...
    used, for 0, Filon is always used)

%% Loop over field
tic
c_wa = FunctionsParent.c_f;
for ii = 1:length(r_vec)
    r = r_vec(ii);
    for jj = 1:length(z_vec)
        z = z_vec(jj);
        for kk = 1:length(f_vec)

            f = f_vec(kk);
            h_f = 2*pi*f/c_wa;
            eta_end = h_f+IntegrationBoundary_DeltaAbove_h_f;

            Integral_sum = 0;
            eta_step  = eta_step_init;
            eta = 0;

            if strcmp(plate_or_freefield,'plate')
                functions_r_z_f = FunctionsPlate(r,z,f);
            else
                functions_r_z_f = FunctionsFluid(r,z,f);
            end
            gaussObj = Integral_Segment_Gauss(functions_r_z_f);
            filonObj = Integral_Segment_Filon(functions_r_z_f);

            eta_cutOf_Shampine = sqrt(  h_f^2  -  ( 2*pi/z + sqrt(h_f^2-[0:1:h_f].^2)  ...
                ).^2 ) - [0:1:h_f]; % find appearant period
            indx_tmp = find(imag(eta_cutOf_Shampine) == 0,1);  % find when imaginary ...
                part is zero
            eta_cutoff = find(abs(eta_cutOf_Shampine(indx_tmp:end)) ...
                <FilonMethodStarts_OscPeriodCutOff_or_EtaCutoff,1)+indx_tmp-1;
            if isempty(eta_cutoff)
                eta_cutoff = eta_end;
            end

            if FilonMethodStarts_OscPeriodCutOff_or_EtaCutoff >= 10 || ...
                FilonMethodStarts_OscPeriodCutOff_or_EtaCutoff == 0
                eta_cutoff = FilonMethodStarts_OscPeriodCutOff_or_EtaCutoff;
            end
```

```
            if eta_cutoff > eta_end
                eta_cutoff = eta_end;
            end
%             tic
            %% Adaptive Gauss integration from eta in range (0,eta_cutoff)
            while eta<eta_cutoff  && eta<eta_end
%                 eta
                if eta+eta_step>eta_cutoff
                    eta_step =  eta_cutoff - eta;
                end
                gaussOrder4 = gaussObj.Gauss4(eta,eta_step);
                gaussOrder5 = gaussObj.Gauss5(eta,eta_step);
                if abs(gaussOrder4 - gaussOrder5)  <=  Err_tresh
                    Integral_sum = Integral_sum + gaussOrder5;
                    eta = eta+eta_step;
                    eta_step = eta_step*2;
                else
                    eta_step=eta_step/2;
                end
            end %eta
%             eta
            %% Adaptive Filon-type integration from eta in range (eta_cutoff,lastwarn)
            warning('')
            while eta<eta_end
%                 eta
                if eta+eta_step>eta_end
                    eta_step =  eta_end - eta;
                end

                Filon_segment_course = 1/2/pi*filonObj.DoIntegrationCoarse(eta, eta_step);
                Filon_segment_fine = 1/2/pi*filonObj.DoIntegrationFine(eta, eta_step);

                if ~isempty(lastwarn)
                    break
                end
                if abs(Filon_segment_course - Filon_segment_fine)  <=  Err_tresh
                    Integral_sum = Integral_sum + Filon_segment_fine;
                    eta = eta+eta_step;
                    eta_step = eta_step*2;
                else
                    eta_step=eta_step/2;
                end
            end %eta
%             eta
            %% Adaptive Gauss integration around peak in integrand, i.e, eta in range ...
                 (lastwarn,h_f+0.1)
            while eta<h_f+0.1
%                 eta
                if eta+eta_step>h_f+0.1
                    eta_step =  h_f+0.1 - eta;
                end
                gaussOrder4 = gaussObj.Gauss4(eta,eta_step);
                gaussOrder5 = gaussObj.Gauss5(eta,eta_step);
                if abs(gaussOrder4 - gaussOrder5)  <=  Err_tresh_peak
                    Integral_sum = Integral_sum + gaussOrder5;
                    eta = eta+eta_step;
                    eta_step = eta_step*2;
                else
                    eta_step=eta_step/2;
                end
            end % eta
%             eta
            %% Adaptive Gauss integration in the evanescent region i.e, eta in range ...
                 (h_f+0.1,eta_end)
            while eta<eta_end
%                 eta
                if eta+eta_step>eta_end
                    eta_step =  eta_end - eta;
                end
                gaussOrder4 = gaussObj.Gauss4(eta,eta_step);
                gaussOrder5 = gaussObj.Gauss5(eta,eta_step);
                if abs(gaussOrder4 - gaussOrder5)  <=  Err_tresh
                    Integral_sum = Integral_sum + gaussOrder5;
                    eta = eta+eta_step;
                    eta_step = eta_step*2;
                else
                    eta_step=eta_step/2;
                end
            end % eta
%             eta
            Pressure_freq_spectrum{ii,jj,kk} = Integral_sum;
%             toc
        end % f
    end % z
end % r
compute_time = toc
%% Extract pressure magnitude and phase
r_index = 1;
z_index = 1;
f_index = 1;
P_level = 20*log10(abs(Pressure_freq_spectrum{r_index,z_index,f_index}));
P_phase = angle(Pressure_freq_spectrum{r_index,z_index,f_index});


ff = cell2mat(Pressure_freq_spectrum(:));
Y_k_Mplate = ff;
a = FunctionsParent.a;

save 'GaussFilon_save.mat' f_vec z_vec r_vec Err_tresh compute_time ...
    Pressure_freq_spectrum ff Y_k_Mplate a
% save 'C:\Users\iis007\OneDrive - University of ...
    Bergen\Dokumenter\Master\AkustikkLAB\MatLab LAB programmer\Mappen jeg bruker på ...
    labben\Transmisjon\AdaptiveMethod_Object_FilonGauss\GaussFilon_save.mat' f_vec ...
    z_vec r_vec Err_tresh compute_time Pressure_freq_spectrum ff Y_k_Mplate a
```

```
% save GaussFilon.mat f_vec z_vec r_vec Err_tresh compute_time Pressure_freq_spectrum ...
    ff Y_k_Mplate
```

B.2 "FunctionsParent.m" file

```
classdef FunctionsParent


    properties (Constant)
        c_f = 1485;       % Fluid velocity
        rho_f = 1000;     % Fluid density
        a = 6.59e-3;      % Piston radius
        v0 = 1;           % piston particle velocity
        rho_p = 8000;     % Plate density
        c_pl = 5780;      % Compressional wave velocity plate
        c_ps = 3130;      % Shear wave velocity plate
        d = 6.05e-3;      % Plate thickness
        z0 = 270e-3;      % Plate distance from piston source
    end


    properties (Access=public)
%          Filon_Integrate;
% Hardcded Filon_Integrate:
Filon_Integrate = @(A,B,C,K,L,M,eta_sym)exp(M.*-1i-L.*eta_sym.*1i-K.*eta_sym.^2.*1i).* ...
    ((B.*5.0e-1i)./K-A.*1.0./K.^2.*L.*2.5e-1i)+ ...
(A.*eta_sym.*exp(M.*-1i-L.*eta_sym.*1i-K.*eta_sym.^2.*1i).*5.0e-1i)./K+1.0./K.^2.* ...
    sqrt(pi).*exp(M.*-1i+(L.^2.*2.5e-1i)./K).* ...
erfi((L.*5.0e-1i+K.*eta_sym.*1i).*1.0./sqrt(K.*-1i)).*1.0./sqrt(K.*-1i).*(A.*L.^2.*1i+ ...
    C.*K.^2.*4.0i+A.*K.*2.0-B.*K.*L.*2.0i).*1.25e-1i;

    end

%     methods
%         function obj = FunctionsParent()    % contructor
%             syms A B C K L M eta_sym
%             integrand = (A*eta_sym^2+B*eta_sym+C) * exp(-i*(K*eta_sym^2+L*eta_sym+M));
%             int_expression_sym = int(integrand,eta_sym);
%             obj.Filon_Integrate = matlabFunction(int_expression_sym,'Vars',{A B C K ...
    L M eta_sym});
%         end
%
%     end
end
```

Appendix C

Supplementary figures

C.1 $|H_{\text{pp}}(0, z_1, f)|$

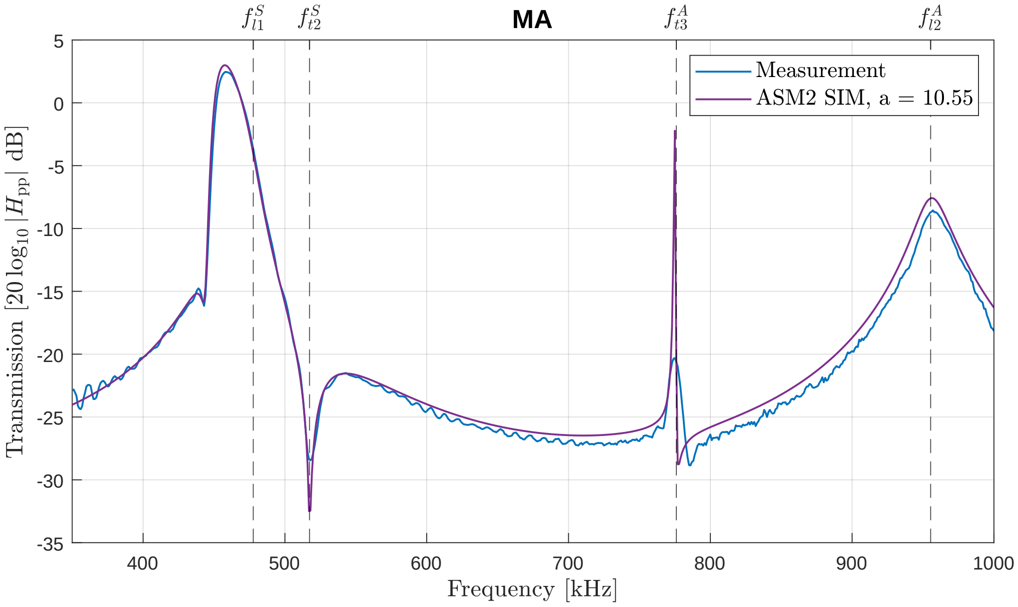

Figure C.1: Comparison of $|H_{\text{pp}}(0, z_1, f)|$ measurement of MA and ASM2 simulation using radius a = 10.55 *mm. The vertical dotted lines is the Lamb mode cutoff frequencies at normal beam incidence in this frequency range.*

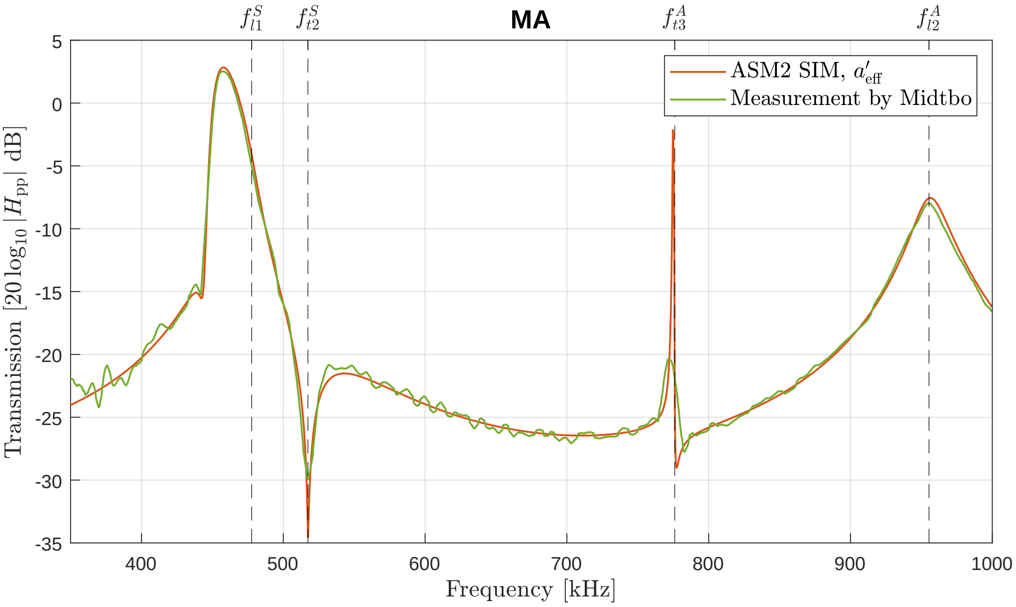

Figure C.2: Comparison of $|H_{\text{pp}}(0,z_1,f)|$ *ASM2 simulation using the effective radius* $a'_{eff} = 10.96$ *mm and measurement of MA by [17]. The vertical dotted lines is the Lamb mode cutoff frequencies at normal beam incidence in this frequency range.*

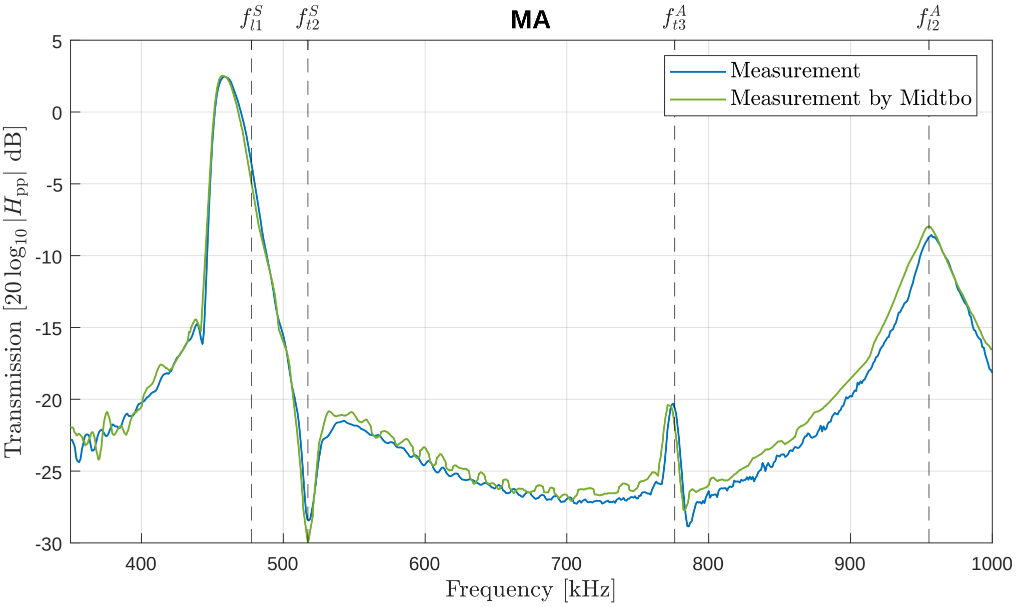

Figure C.3: Comparison of $|H_{\text{pp}}(0,z_1,f)|$ *measurement of MA by this author and measurement of MA by [17]. The vertical dotted lines is the Lamb mode cutoff frequencies at normal beam incidence in this frequency range.*

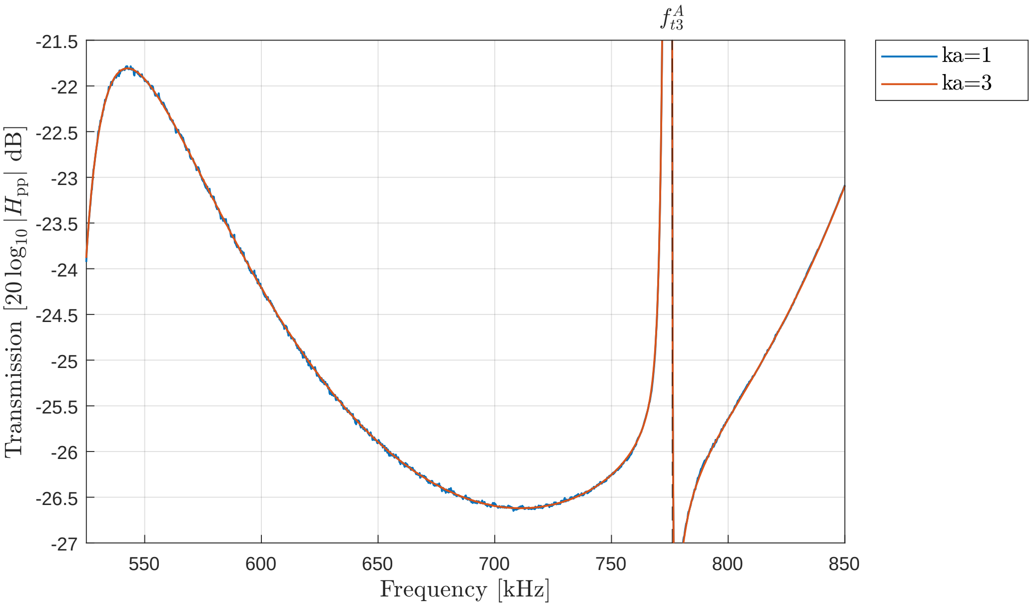

Figure C.4: Comparison of $|H_{\mathrm{pp}}(0,z_1,f)|$ ASM2 simulations of ka-numbers 1 and 3 in a frequency range of fluctuations for ka = 1.

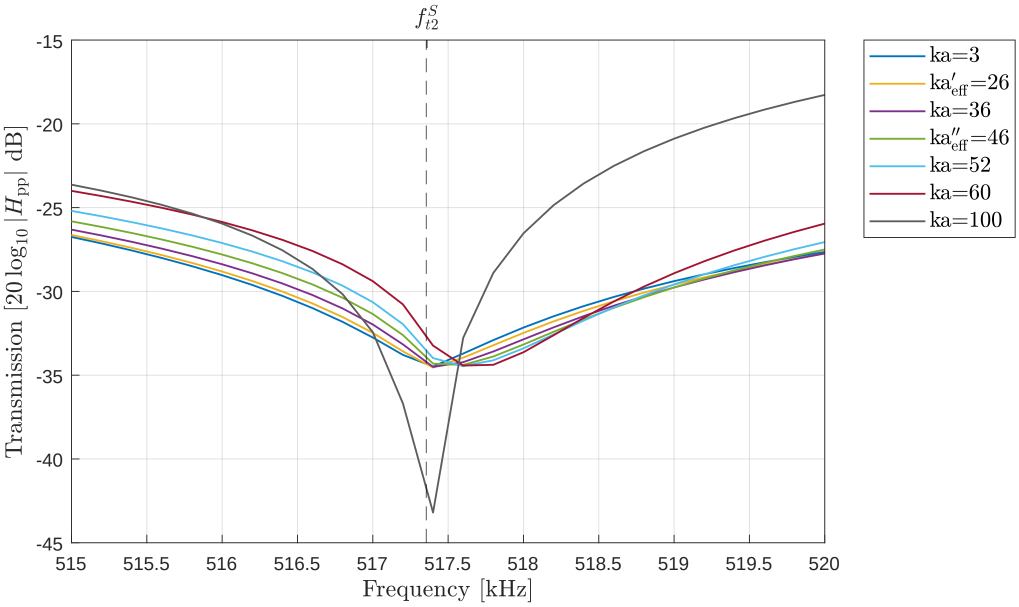

Figure C.5: Zoomed-in version of Fig. 5.22b showing the frequency band associated with TS2. ASM2 simulations of $|H_{\mathrm{pp}}(0,z_1,f)|$ for ka-numbers 3, 26’, 36, 46”, 52, 60 and 100.